CORA Cork Open Research Archive
Cartlann Taighde Oscailte Chorcaí

Title	High-efficiency photovoltaics through mechanically stacked integration of solar cells based on the InP lattice constant
Authors	Mathews, Ian P.
Publication date	2014
Original Citation	Mathews, I. P. 2014. High-efficiency photovoltaics through mechanically stacked integration of solar cells based on the InP lattice constant. PhD Thesis, University College Cork.
Type of publication	Doctoral thesis
Rights	© 2014, Ian P. Mathews - http://creativecommons.org/licenses/by-nc-nd/3.0/
Download date	2026-11-07 12:52:55
Item downloaded from	https://hdl.handle.net/10468/1705



UCC
University College Cork, Ireland
Coláiste na hOllscoile Corcaigh

High-Efficiency Photovoltaics through Mechanically Stacked Integration of Solar Cells based on the InP Lattice Constant

Thesis by

Ian Mathews, BEng (Hons), MSc



May 2014

Thesis submitted to the National University of Ireland, Cork, for a PhD in Electrical and Electronic Engineering

Head of Department

Prof. Nabeel A. Riza

Chair Professor of Electrical and Electronic Engineering, University College Cork

Supervisors

Dr. Alan P. Morrison

Senior Lecturer in Electrical and Electronic Engineering, University College Cork

Mr. Brian Corbett

Head of Group, III-V Materials and Devices, Tyndall National Institute

I hereby certify that this thesis submission is an original piece of research work conducted in the Electrical and Electronic Engineering Department, University College Cork, Ireland, and the Tyndall National Institute, University College Cork, Ireland.

_____

Ian Mathews

Acknowledgments

It goes without saying that a PhD is not an individual pursuit. What has to be said is that mine would never have been possible without the considerable support and encouragement of many people, first of whom were without doubt my parents. They have been unrelenting in their support of my academic pursuits. Of course what I really mean is they kept their concerns to themselves and allowed me to continue my college education for 8 ½ years even when they thought better. Thanks must go to my siblings Ciara and Daragh, your ability to remain calm and thoughtful no matter what situation you face is something I hope I am starting to learn from you. This thesis is also dedicated to my grandparents who produced incredibly large but incredibly close families. I want to especially thank Muzz who in the strictest sense of the word *told* Dad a long time ago that his 'primary responsibility was to educate your kids as far as they want to go'. Needless to say without those words ringing in his ears he may have forced me to get a real job much sooner.
Thanks must also go to my many friends inside and outside college. At times over the last number of years I have pushed your patience as I found the PhD process frustrating but you kept me in good spirits and plenty of pints. You know who you are so thanks for listening.

Academically I would like to acknowledge the support of my Supervisors Dr. Alan Morrison and Mr. Brian Corbett. Their depth of knowledge on such a breadth of topics impressed me from my first day and I just hope to have taken a fraction of their knowledge and capabilities with me. I would also like to thank my 'third supervisor' Dr. Donagh O'Mahony. His patience during the early days was invaluable as he never lost hope despite my slow pace of progress or plentiful mistakes. His ability to teach me the more practical side of a PhD and remind of the bigger picture kept me on the right path.

Thank you to my examiners for taking the time to review my work and guide me in suitable directions. Your thoroughness in reviewing such a lengthy manuscript as a PhD thesis was certainly a lesson to me.

As I submitted my thesis and ended what has been a long journey, I was fortunate to be informed by my Aunt Brenda that if a career in technology does not work out, I now have viable alternatives…..

Ian, I'm glad to see you can mechanically stack solar cells, cos it means you can always get a night job stacking shelves in Tesco if this silly little job of yours doesn't work out. Impressed too with the sputtering and flip chipping which means you would be confident running your own chip van. Employing non native substates so you don't have to pay Irish substrates is a stroke of genius.

One thing though, I don't think selective wet etching is legal in Catholic Ireland. Just saying...

Ian

Abstract

Solar Energy is a clean and abundant energy source that can help reduce reliance on fossil fuels around which questions still persist about their contribution to climate and long-term availability. Monolithic triple-junction solar cells are currently the state of the art photovoltaic devices with champion cell efficiencies exceeding 40%, but their ultimate efficiency is restricted by the current-matching constraint of series-connected cells.

The objective of this thesis was to investigate the use of solar cells with lattice constants equal to InP in order to reduce the constraint of current matching in multi-junction solar cells. This was addressed by two approaches:

Firstly, the formation of mechanically stacked solar cells (MSSC) was investigated through the addition of separate connections to individual cells that make up a multi-junction device. An electrical and optical modelling approach identified separately connected InGaAs bottom cells stacked under dual-junction GaAs based top cells as a route to high efficiency. An InGaAs solar cell was fabricated on an InP substrate with a measured 1-Sun conversion efficiency of 9.3%. A comparative study of adhesives found benzocyclobutene to be the most suitable for bonding component cells in a mechanically stacked configuration owing to its higher thermal conductivity and refractive index when compared to other candidate adhesives. A flip-chip process was developed to bond single-junction GaAs and InGaAs cells with a measured 4-terminal MSSC efficiency of 25.2% under 1-Sun conditions.

Additionally, a novel InAlAs solar cell was identified, which can be used to provide an alternative to the well established GaAs solar cell. As wide bandgap InAlAs solar cells have not been extensively investigated for use in photovoltaics, single-junction cells were fabricated and their properties relevant to PV operation analysed. Minority carrier diffusion lengths in the micrometre range were extracted, confirming InAlAs as a suitable material for use in III-V solar cells, and a 1-Sun conversion efficiency of 6.6% measured for cells with 800 nm thick absorber layers.

Given the cost and small diameter of commercially available InP wafers, InGaAs and InAlAs solar cells were fabricated on alternative substrates, namely GaAs. As a first demonstration the lattice constant of a GaAs substrate was graded to InP using an $In_xGa_{1-x}As$ metamorphic buffer layer onto which cells were grown. This was the first demonstration of an InAlAs solar cell on an alternative substrate and an initial step towards fabricating these cells on Si.

The results presented offer a route to developing multi-junction solar cell devices based on the InP lattice parameter, thus extending the range of available bandgaps for high efficiency cells.

Related Publications

The research described in this thesis has been published in and submitted to several international journals. Furthermore, the work has been presented at various international peer reviewed conferences.

Journal Papers

"InAlAs solar cell on a GaAs substrate employing a graded $In_xGa_{1-x}As$ – InP Metamorphic Buffer Layer", **I. Mathews**, D. O'Mahony, A. Gocalinska, M. Manganaro, E. Pelucchi, M. Schmidt, A.P. Morrison, and B. Corbett, *Applied Physics Letters* 102, 033906 (2013).

"Theoretical performance of multi-junction solar cells combining III-V and Si materials", **I. Mathews**, D. O'Mahony, B. Corbett and A.P. Morrison, *Optics Express*, Vol. 20, Issue S5, pp. A754-A764 (2012)

"Adhesive bonding for improved transmission in Mechanically Stacked Solar Cells", **I. Mathews**, D. O'Mahony, K. Thomas, B. Corbett and A. P. Morrison. *Progress in Photovoltaics (Accepted: Progress in Photovoltaics).*

International Peer Reviewed Conference Presentations

"InAlAs and InGaAs solar cell development for use in monolithic triple-junction solar cell with improved spectrum splitting", **I. Mathews**, D. O'Mahony, A. Gocalinska, E. Pelucchi, K. Thomas, A.P. Morrison and B. Corbett. *EUPVSEC 2013*, Paris, October 2013.

"Nanostructures for High Efficiency Concentrator Photovoltaic Solar Energy", **I. Mathews**, D. O'Mahony, A. Gocalinzska, E. Pelucchi, A.P. Morrison and B. Corbett. *Euro Nano Forum 2013*, Dublin, June 2013.

"Evaluation of Polydimethylsiloxane (PDMS) as an adhesive for mechanically stacked multi-junction solar cells", **I. Mathews**, D. O'Mahony, B. Corbett A.P. Morrison, *Smart Surfaces for Solar and Biosensor applications*, Dublin, March 2012.

"Evaluation of the optical performance of a Si solar cell mechanically stacked GaAs using Polydimethylsiloxane (PDMS) as an adhesive", **I. Mathews**, D. O'Mahony, B. Corbett and A.P. Morrison, *Next Generation Solar Energy*, Erlangen, Germany, Dec. 2011.

"Optimisation of anti-reflection coatings for mechanically stacked solar cells", **I. Mathews**, D. O'Mahony, B. Corbett A.P. Morrison, *Photonics Ireland 2011*, Malahide, Dublin, Sept. 2011.

"Mechanically Stacked Solar Cells for Concentrator Photovoltaics", **I. Mathews**, D. O'Mahony, W. Yu, D. Gordon, N. Cordero, B. Corbett, A. Morrison, 2011, *International Conference on Renewable Energies and Power Quality*, Gran Canaria, Spain, April 2011.

"Concentrator photovoltaic technology development for III-V epitaxial nanostructures", D. O'Mahony, N. Cordero, W. Yu, **I. Mathews**, B. Corbett, D. Gordon and A. P. Morrison., *Nano for Clean Technologies Workshop (Photovoltaics)*, March 2011, University of Ulster, Northern Ireland.

"Design considerations for mechanically stacked solar cells in terrestrial Concentrating PV systems", **I. Mathews**, W. Yu, D. Gordon, D. O'Mahony, N. Cordero, B. Corbett, A. Morrison, *3rd International Workshop on Concentrating Photovoltaics: Optics and Power*, Bremerhaven, Germany, October 2010.

Table of Contents

Abstract v

Related Publications vi

List of Figures xii

Chapter 1 – Introduction and Motivation

1.1. Solar Energy 1

1.2. Competing photovoltaic technologies 2

1.3. Solar cell device physics 4

1.4. Multi-junction solar cells for concentrating photovoltaics 19

1.4.1. Better spectrum utilisation 20

1.4.2. Concentrating Photovoltaics 21

1.5. Mechanically stacked solar cells 23

1.6. Objectives 26

1.7. Thesis outline 26

1.8. References 27

Chapter 2 – High-efficiency multi-junction solar cells

2.1 Introduction 30

2.2 GaAs based multi-junction solar cells 31

2.3 Heterogeneous integration of solar cells through mechanical stacking 34

2.3.1 Materials 35

2.3.1.1 Ge 37

2.3.1.2 GaSb 38

2.3.1.3 InGaAs(P) 38

2.3.1.4 Silicon 40

2.4 Mechanical Stacking 40

2.4.1 Ohmic resistance 40

2.4.2 Optical losses 44

2.4.3 Reduced optical losses through Spectrum Splitting 48

2.5 Annual Energy Yield 51

2.6 Multi-junction solar cells with lattice constants equal or close to that of InP 51

2.7 References 52

Chapter 3 – Simulation and design of the photovoltaic properties of mechanically stacked solar cells

3.1. Introduction 57

3.2. Modelling solar cell and terminal configuration 57

3.2.1. Monolithic device structures 60

3.2.2. Comparative stacked cells 61

3.2.3. Modelling results 62

3.2.4. Efficiency versus illumination intensity 66

3.3. Modelling the effect of an adhesive interface on a GaAs-InGaAs tandem stack 67

3.3.1. Reflection model 68

3.3.2. Front surface reflection 70

3.3.3. Adhesive Interface 71

3.3.4. Absorption of Adhesives 73

3.3.5. Adhesive thickness 74

3.3.6. Thermal modelling 75

3.3.7. Combined interface properties 77

3.4. Final design and specifications 79

3.5. Summary 80

3.6. References 80

Chapter 4 – InGaAs and InAlAs solar cell development

4.1. Introduction 82

4.2. Cell 1: $In_{0.53}Ga_{0.47}As$ 1J solar cells 83

4.2.1. Emitter and Base region design 83

4.2.2. Optimised cell structure 86

4.2.3. Cell Processing 87

4.2.4. Photovoltaic characterisation 88

4.3. Cell 2: $In_{0.52}Al_{0.48}As$ 1J solar cell 91

4.3.1. InAlAs cell structure 91

4.3.2. Cell Processing 92

4.3.3. Photovoltaic characterisation 93

4.3.4. Electrical and material characterisation 94
4.4. Advanced substrate engineering 100
4.4.1. MOVPE growth of metamorphic buffer layers 100
4.4.2. Fabrication of $In_{0.52}Al_{0.48}As$ and $In_{0.53}Ga_{0.47}As$ solar cells on GaAs substrates 101
4.4.3. Material characterisation 102
4.4.4. Photovoltaic characterisation of cells on the MBL 104
4.4.5. Spectral response of cells on the MBL 105
4.4.6. Analysis on the effect of defects on InAlAs solar cell electrical properties 107
4.4.7. Alternative TDD analysis 110
4.5. Summary 111
4.6. References 112

Chapter 5 – BCB bonded GaAs-InGaAs mechanically stacked solar cell

5.1. Introduction 114
5.2. Single-Junction GaAs Solar Cells 115
5.2.1. GaAs cell design 115
5.2.2. Cell Processing 116
5.3. BCB Bonding 117
5.3.1. Phase 1: Bond Development 119
5.3.2. Phase 2: Final bonding process for MSSCs 123
5.4. Mechanical stack measurements 124
5.4.1. External Quantum Efficiency 126
5.4.2. Optical Analysis 128
5.5. Future implementation 131
5.6. Summary 132
5.7. References 133

Chapter 6 – Conclusions and Future Work

Appendices

Appendix A: Photovoltaic and Electrical characterisation 138
Appendix B: Detailed balance limit of efficiency calculation 143
Appendix C: PC1D 145
Appendix D: Nominal and measured solar cell structures grown by MOVPE 147

Appendix E: Si Solar Cell 148
Appendix F: Solar cell processing procedures, detailed processing conditions and mask layouts 150

List of Figures

Figure 1.1: *Global cumulative installed PV capacity since the year 2000 as in reference [1]…….2*

Figure 1.2: *Performance and price of competing photovoltaic technologies at year end 2008 as in reference [3]……3*

Figure 1.3: *Schematic representation of the depletion region, electric field, quasi-neutral p & n regions and the forces acting on the carriers in a p-n junction. ……6*

Figure 1.4: *(a) Steady-state minority carrier concentration in a p-n junction under forward bias and (b) ideal electron and hole current components through a p-n junction under forward bias…7*

Figure 1.5: *Measured DJV of an InGaAs solar cell (described in Chapter 4) with two regions of recombination identified. A straight line is fitted to each region and representative equations shown.……10*

Figure 1.6: *Energy band structures of GaAs and silicon as in [5]……11*

Figure 1.7: *Absorption coefficient as a function of wavelength for Si, GaAs, $In_{0.53}Ga_{0.47}As$ and $Al_{0.7}Ga_{0.3}As$ [5], [6]. Also shown is the photon flux of the AM1.5G standard solar spectrum as a function of wavelength.……12*

Figure 1.8: *Current-voltage characteristics of a p-n junction solar cell under illumination and in the dark as well as the equivalent circuit diagram.……13*

Figure 1.9: *Outline of the three principal recombination types in bulk semiconductor materials. ……15*

Figure 1.10: *(a) schematic outline of the emitter, depletion and base regions of a GaAs solar cell and (b) the contribution of each region to the overall IQE of a cell. ……18*

Figure 1.11: *ASTM G173-03 Air Mass 1.5 direct reference solar spectrum. The red area represents the portion of the spectrum absorbed by a Si solar cell.……19*

Figure 1.12: *ASTM G173-03 Air Mass 1.5 direct reference solar spectrum. The portion absorbed by each cell in a triple junction solar cell is highlighted. ……20*

Figure 1.13: *Schematic outline of a concentrating photovoltaic system. The optical and thermal design elements are shown. ……22*

Figure 1.14: *Outline of (a) a monolithic triple-junction solar cell and (b) a mechanically stacked triple-junction solar cell. Circuit diagrams are given to highlight the reduction of the current matching constraint in the stacked device. A Ge junction will produce approximately twice the current of the top cell (i.e. $I_2 \approx 2I_1$)……24*

Figure 2.1: *Detailed balance efficiency for the AM1.5d spectrum under 500 Suns concentration of a triple-junction solar cell with a GaInP/GaAs (1.9/1.41 eV) top cell and a series connected bottom cell (dashed line) or independently contacted bottom cell (solid line) as a function of the bottom cell Eg. The junction temperature for the model was 300 K. The peak efficiency for each cell type is highlighted as a red dot.……32*

Figure 2.2: *Bandgap (300 K) versus lattice constant for a range of semiconductor materials and alloys. The lattice matched GaInP/GaAs/Ge triple junction cell is highlighted with blue dots. The bandgap and % lattice mismatch to GaAs for $In_xGa_{1-x}As$ are shown as well as the range of bandgaps available for the GaInNAs material system.* 33

Figure 2.3: *The open-circuit voltage, measured under 1 Sun AM1.5G conditions, of the state of the art single-junction narrow bandgap cells stacked under GaAs or GaInP/GaAs top cells (black diamonds). Also shown is the Bandgap-Voltage offset (W_{oc}) of the cells (blue open circles) and the bandgap of the material (solid line). Note a measured value for a GaSb cell was unavailable [11]–[14].* 36

Figure 2.4: *The short-circuit current density, measured under 1 Sun AM1.5G conditions, of the state of the art single-junction narrow bandgap cells stacked under GaAs or GaInP/GaAs top cells (diamonds). Also shown is the photocurrent density of an ideal solar cell with 100% EQE as a function of bandgap (solid-line) for the AM1.5G spectrum for $\lambda > 880$ nm. The ratio of the measured short-circuit current density to the ideal photocurrent density is also given (open circles) [8], [11]–[14].* 37

Figure 2.5: *Simulated photovoltaic conversion efficiency of a single-junction 1 cm^2 GaAs solar cell under concentration as a function of series resistance. The simulations were carried out using PC1D [34] for a 250 nm p-GaAs emitter ($2x10^{18}$ cm^{-3}) and 3500 nm n-GaAs base ($3x10^{17}$ cm^{-3}) layers.* 41

Figure 2.6: *Mechanical Stacking strategies: (a) Metal holders (b) Epoxy bonding of solar sells (c) Direct semiconductor bonded solar cells (d) Grid metal bonding.* 42

Figure 2.7: *Weighted transmission of 880 – 1700 nm photons through n-GaAs as a function of doping level and thickness as calculated using data in [42].* 45

Figure 2.8: *The average reflection of wavelengths between 890-1680 nm at a GaAs-InGaAs interface as a function of the interface index of refraction modelled using Snell's law. The measured refractive indices (from an ellipsometric database) of GaAs and $In_{0.53}Ga_{0.47}As$ in this region are presented in the inset figure.* 46

Figure 2.9: *Simulated front surface reflection at normal incidence from a GaAs solar cell with a double-layer SiO_2/ZnS anti-reflection coating.* 47

Figure 2.10: *Spectrum splitting solar cell concepts (a) A dichroic mirror is used to reflect long wavelengths onto the narrow bandgap cell while higher energy photons are transmitted to the Wide Eg cell (b) A prism splits the relevant bandwidth range of photons onto each component sub-cell.* 49

Figure 2.11: *Selected results for the efficiency of multi-junction solar cells over the last decade. Additional references not in text: [55], [56].* 50

Figure 3.1: *The absorption co-efficients of the materials considered for multi-junction solar cells. The AM1.5d ASTM G173-03 spectrum is shown for comparison.* 58

Figure 3.2: *Triple-junction (a, b) and four-junction (c) series-connected multi-junction solar cell configurations modelled where the interface between Si and InGaAs and the other semiconductor materials is considered as a completely transparent and ideal ohmic contact.* *61*

Figure 3.3: *Triple-junction mechanically stacked solar cells formed using Si (a) and InGaAs (b) bottom solar cells and a four-junction configuration (c).* *62*

Figure 3.4: *The modelled electrical performance of a Si solar cell mechanically stacked under a dual junction AlGaAs/GaAs solar cell as a function of Si thickness.* *64*

Figure 3.5: *The modelled electrical performance of an InGaAs solar cell mechanically stacked under a dual junction AlGaAs/GaAs solar cell as a function of InGaAs combined emitter and base thickness.* *65*

Figure 3.6*: Iso-efficiency plot of the combined Si and InGaAs solar cell theoretical efficiencies (%) when stacked under an AlGaAs/GaAs dual junction solar cell as a function of Si (d_1) and InGaAs (d_2) thickness.* *65*

Figure 3.7: *Efficiency versus solar intensity for each of the modelled solar cell configurations.* ..*67*

Figure 3.8: *Outline of the prototype GaAs-InGaAs stacked tandem solar cell.* *68*

Figure 3.9: *Measured refractive index (real-part) of the dielectric materials considered for anti-reflection coatings.* *69*

Figure 3.10: *Measured extinction co-efficient of SiN_x and ZnS dielectric layers.* *70*

Figure 3.11: *Simulated reflection from the front surface of a single-junction GaAs solar cell for each of the optimised ARC designs.* *71*

Figure 3.12: *The measured absorption in PDMS.* *73*

Figure 3.13: *The simulated light-generated photocurrent density of an InGaAs cell stacked under a GaAs top cell as a function of adhesive and its thickness.* *74*

Figure 3.14: *Outline of the thermal heat load and path for the tandem stack.* *75*

Figure 3.15: *Temperature increase in a GaAs top cell as a function of BCB bond thickness and cell size under AM1.5d x500 Suns.* *77*

Figure 3.16: *The overall stack efficiency losses due to the combined optical and thermal losses as a function of adhesive bonding layer material and thickness.* *78*

Figure 3.17*: Schematic outline of the as designed MSSC.* *79*

Figure 4.1: *Simulated light-generated photocurrent density from an InGaAs solar cell under a GaAs based top cell as a function of InGaAs absorber layer and InP window thickness. Reflection was not considered at any interface.* *84*

Figure 4.2: *Simulated open-circuit voltage of a p-on-n InGaAs solar cell as a function of emitter doping level.* *85*

Figure 4.3: *Simulated open-circuit voltage of a p-on-n InGaAs solar cell as a function of base doping level.* *86*

Figure 4.4: *Outline of the as processed InGaAs solar cell with the SiN ARC/passivation layer highlighted.....88*

Figure 4.5: *Measured photocurrent density-voltage characteristics of InGaAs solar cells under 1-Sun conditions.....88*

Figure 4.6: *Measured EQE of the stand-alone InGaAs solar cell as well as the measured reflection from the front surface and the simulated absorption of the AM1.5G spectrum in a 100 nm InP layer.....90*

Figure 4.7: *Cross-sectional TEM image of the strained $In_{0.35}Al_{0.65}As$ window layer. No defects are visible.....92*

Figure 4.8: *Outline of the as processed InAlAs single-junction solar cells.....93*

Figure 4.9: *Measured photocurrent density-voltage characteristics of InAlAs solar cells under 1-Sun (AM1.5G) conditions.....94*

Figure 4.10: *Measured dark current density-voltage of InAlAs solar cells at 20 ^{o}C (black line) and the extracted ideality (black dashed line) as a function of voltage. The straight lines fitted to the J_{o1} and J_{o2} dominated regions are shown as red and blue dashed lines respectively.....96*

Figure 4.11: *Measured External Quantum Efficiency (blue circles) and front-surface reflection (dashed black line) as measured for the InAlAs solar cells. The best-fit and low front-surface recombination simulated responses are given as a blue line and dotted red line respectively.....97*

Figure 4.12: *Overview of the metamorphic buffer layer growth profile. The homoepitaxial buffer GaAs layer is followed by alloys of a continuous convex compositional gradient of the In content from x = 0 % to 53 %. The grading comprises of three sections: first 400 nm along a parabolic curve, then linearly, with the slope of the curve reduced for the final 190 nm. The structure is capped with an InP layer, grown under the best growth conditions as established in [14]. 101*

Figure 4.13: *Outline of the (a) InAlAs and (b) InGaAs solar cells structures grown by MOVPE on MBL-GaAs substrates.....102*

Figure 4.14: *Cross-sectional bright field TEM image of the MBL of the solar cell structure.....103*

Figure 4.15: *Cross-sectional bright field TEM image of the complete MBL and InAlAs photoactive region. Only partial focus was achieved at low magnification with the 'grain' structure visible not real; but a clear delineation of each material layer obvious. Higher magnification stitched-images show the permeation of defects through the complete epitaxially grown structure. 104*

Figure 4.16: *Measured photocurrent density-voltage characteristics of InAlAs solar cells on InP and GaAs substrates under 1-Sun conditions.....105*

Figure 4.17: *Measured photocurrent density-voltage characteristics of InGaAs solar cells on InP and GaAs substrates under 1-Sun conditions.....105*

Figure 4.18: *External Quantum Efficiency as measured for both the InAlAs and InGaAs solar cells grown on GaAs (blue diamonds) and InP substrates (dotted line). The simulated response for cells on a GaAs substrate is given as a solid blue line. 106*

Figure 4.19: *Comparison of the current density-voltage measurements for InAlAs cells grown on InP and GaAs substrates taken in the dark at 20 ^{o}C. A straight line is fitted in the 0.7 – 1.0 V region to extract J_{o2}.* 109

Figure 4.20: *SEM image of the InGaAs MBL layer after InAlAs removal by wet etching. The 'defects' are directly visible and were used to estimate the defect density in the MBL*.....111

Figure 5.1: *Schematic outline of the fabricated GaAs-InGaAs stacked solar cell as designed in Chapter 3.*.....114

Figure 5.2: *Optical image of a processed 1/4 wafer of single-junction GaAs solar cell material with both p- (grid line and bus bars) and n-type contacts (bus bars only) visible on the front surface. An anti-reflection coating was not deposited on this chip.*.....117

Figure 5.3: *Outline of the processed (a) control and (b) front surface contacted GaAs solar cells.* 117

Figure 5.4: *Flip Chip Bonder FINEPLACER® pico MA (© Finetech 2013: http://www.flickr.com/photos/30984232@N02/2903755265).*.....118

Figure 5.5: *BCB layer thickness versus spin speed for both BCB resins considered in this study where 3022-57 is the higher viscosity solution.* 119

Figure 5.6: *Optical image of quartz pieces bonded to Si solar cells using (a) 3022-46 and (b) 3022-57 grade BCB resin. In (a) the voids formed during processing are highlighted in the yellow bubble and in (b) the region where pressure was applied by the flip-chip bonder is highlighted by a dashed yellow square in (b).*.....120

Figure 5.7: *Optical image of a Si chip bonded to an InGaAs solar cell (post scribing to form cross-section for imaging) used for development of the flip-chip process.* 121

Figure 5.8: *Outline of the two stack set-ups used to evaluate the effectiveness of BCB in reducing interface reflection (a) a DLARC deposited on the back surface of an n-GaAs chip and (b) a single-layer ZnS ARC and BCB bond between an n-GaAs chip and the Si solar cell.*.....122

Figure 5.9: *Measured EQE response of a Si solar cell before stacking with GaAs (black triangles) and post stacking with an air gap (red diamonds) and a BCB bond (blue diamonds). Also shown is the improvement pre-bonding with BCB for a single-layer ZnS ARC (green diamonds).* 122

Figure 5.10: *Optical images of (a) the fabricated and packaged GaAs-InGaAs stacked cell, the inset image shows the wire bonding to the cell bus bars, and (b) the BCB bond between a GaAs top and InGaAs bottom cell post dicing.* 124

Figure 5.11: *Measured photocurrent density-voltage characteristics of a control GaAs cell (closed circles), top-contacted GaAs cell (open circles), stand alone InGaAs cell (triangles) and stacked InGaAs cell (open triangles) under 1-Sun conditions.* 126

Figure 5.12: *Measured EQE (green diamonds) of the stand-alone InGaAs solar cell as well as the measured reflection from the front surface and the simulated absorption of the AM1.5G spectrum in a 100 nm InP layer. 127*

Figure 5.13: *Measured EQE of the GaAs (blue triangles) and InGaAs (green circles) cells in stacked formation. Also shown is the measured reflection from the stack (solid line) and the EQE of the InGaAs cell pre-bonding (dots). 128*

Figure 5.14: *Measured EQE of an InGaAs bottom cell stacked under a GaAs top cell with a 360 μm thick substrate (red circles) and a 140 μm thick substrate (blue substrates). 129*

Figure 5.15: *Simulated reflection at the cell interface for the optimum (black) and fabricated (grey) optical coatings. The red line is the simulated as fabricated coatings when 'wedging' is considered. 129*

Figure 5.16: *Measured reflection from the front surface of the stacked solar cell (blue line). Also shown is the simulated reflection for the fabricated optical system (black line) and the optimum optical coating regime (purple dots). 130*

Figure 5.17: *Outline of BCB wafer bonding process: (a) BCB is spin coated on the back of the top cell and front of the bottom cell at ~ 5 μm thickness providing a planar surface for bonding (b) cells are bonded by contacting the BCB layers and curing. 131*

Figure 5.18: *Planarization ratio as a function of metal line width for dry etch grade BCB (3022 series). The metal line height is 4 μm [5]. 132*

Figure 6.1*: Selected results for the efficiency of multi-junction solar cells over the past decade including results from this thesis. 135*

Fig. A: *Layout of the lamp housing of the Newport Oriel 91193 Solar Simulator. 138*

Fig. B*: Picture of the solar simulator. 139*

Fig. C: *Readout meter and reference cell assembly.....140*

Fig. D: *Picture of the inside of the dark housing showing a solar cell under test (lamp shutter closed). The reference cell is also shown although it is placed on the adjustable stage when reading light intensity. 140*

Fig. E: *Picture of the Bentham PVE300 with relevant parts labelled. 141*

Fig. F: *Picture of the measurement set-up within the spectral response kit. A calibrated Si photodetector is shown under the illuminating beam (not on). Only one probe is shown for clarity.....142*

Fig. G: *Screenshot of the parameter input screen of PC1D. 145*

Fig. H: *Screenshot of the output screen of PC1D. 146*

Fig. I: *Optical image of NAREC Si solar cell. 148*

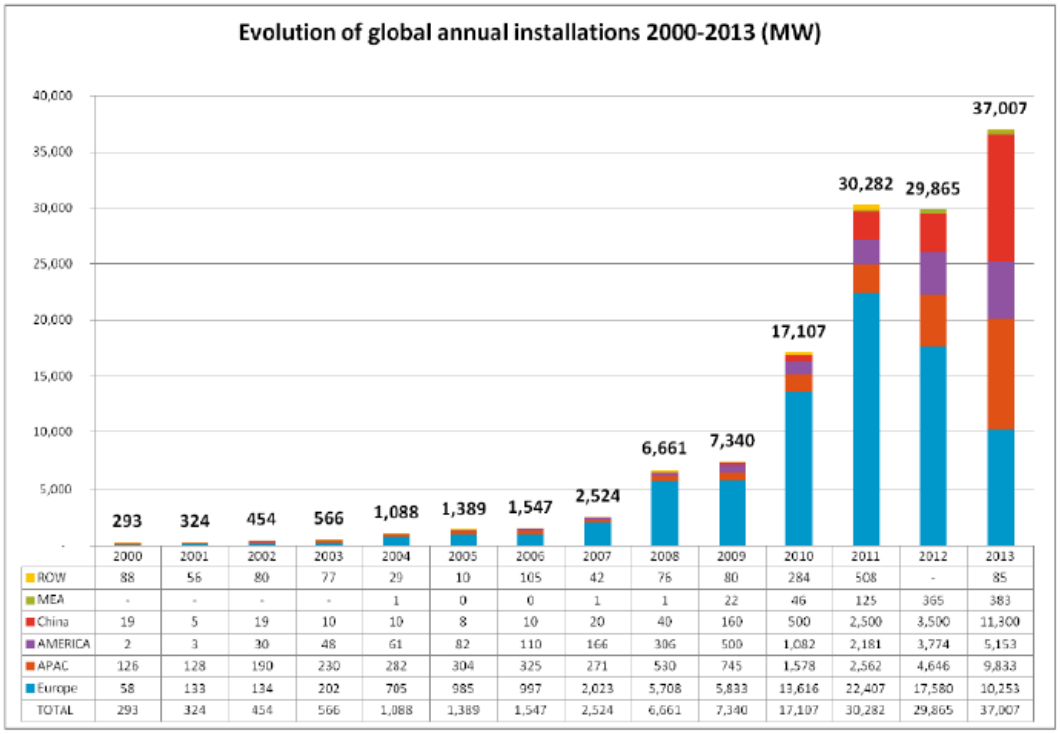
Fig. J: *Measured 1-Sun IV characteristics of single-junction NAREC Si solar cell.....149*

Chapter 1

Introduction and Motivation

1.1. Solar Energy

Solar Energy is a clean and abundant energy source which can help reduce reliance on fossil fuels around which questions still persist about their contribution to climate change and long-term availability. Photovoltaic (PV) devices convert sunlight to useful electrical energy and have proven to be a cost-effective option in niche power supply applications such as calculators and off-grid homes as well as for grid-tied power generation in locations with high electricity costs. In the last decade the introduction of government subsidies in the form of feed-in-tariffs in a number of EU countries has led to a proliferation of installed PV capacity (Figure 1.1) with 50% of worldwide PV installations in 2011 occurring in Germany and Italy alone [1]. In the last decade 51 GW of PV power generation capacity has been commissioned in the EU placing photovoltaics as the third most installed electricity generation technology surpassed only by Natural Gas (116 GW) and Wind Power plants (84 GW) over the same period. In the last two years the worldwide cumulative capacity almost doubled from 70 GW to 137 GW. The impressive growth in 2013 was led by China and Japan who added 11.3 GW and 6.9 GW capacity respectively. Despite the impressive growth of capacity, at the end of 2013 PV represented < 1 % of global electricity demand. The 2012 cutbacks in German and UK feed-in-tariffs show the appetite for state-supported PV power markets is abating in the current economic crisis. Optimistic projections foresee the growth of installed capacity to 330 GW by 2016 [1] but it is clear for large-scale global adoption PV electricity generation systems must compete with fossil fuel sources in major electricity markets without state-aid.



	2000	2001	2002	2003	2004	2005	2006	2007	2008	2009	2010	2011	2012	2013
ROW	88	56	80	77	29	10	105	42	76	80	284	508	-	85
MEA	-	-	-	-	1	0	0	1	1	22	46	125	365	383
China	19	5	19	10	10	8	10	20	40	160	500	2,500	3,500	11,300
AMERICA	2	3	30	48	61	82	110	166	306	500	1,082	2,181	3,774	5,153
APAC	126	128	190	230	282	304	325	271	530	745	1,578	2,562	4,646	9,833
Europe	58	133	134	202	705	985	997	2,023	5,708	5,833	13,616	22,407	17,580	10,253
TOTAL	293	324	454	566	1,088	1,389	1,547	2,524	6,661	7,340	17,107	30,282	29,865	37,007

Figure 1.1: Global cumulative installed PV capacity since the year 2000 as in reference [1].

1.2. Competing photovoltaic technologies

The cost of photovoltaic power plants is mostly accounted for by the balance of system components and installation costs (~40%), power equipment (~10%) and the cost of photovoltaic modules themselves (~50%) [2]. Flat-plate crystalline-Si solar panels have been the standard photovoltaic module for decades and enjoy up to 90% market share [3]. Even with the recent flood of cheap modules from China the cost of electricity generated from these systems is still greater than from fossil fuels. New technologies are emerging which look to reduce the cost ($/W) of photovoltaics by using thin-film (CIGS, a-Si, CdTe) or organic materials (Dye Sensitised Solar Cells). Alternatively the $/W of a PV module can be reduced by increasing the power produced i.e. by using technologies with high photovoltaic conversion efficiencies such as multi-junction solar cells for concentrating photovoltaics which are the focus of this thesis. Figure 1.2 compares the cost and market share of competing PV technologies as of 2008. Although the data is 5 years out of date is provides a useful comparison of the relative difference between solar cell technologies.

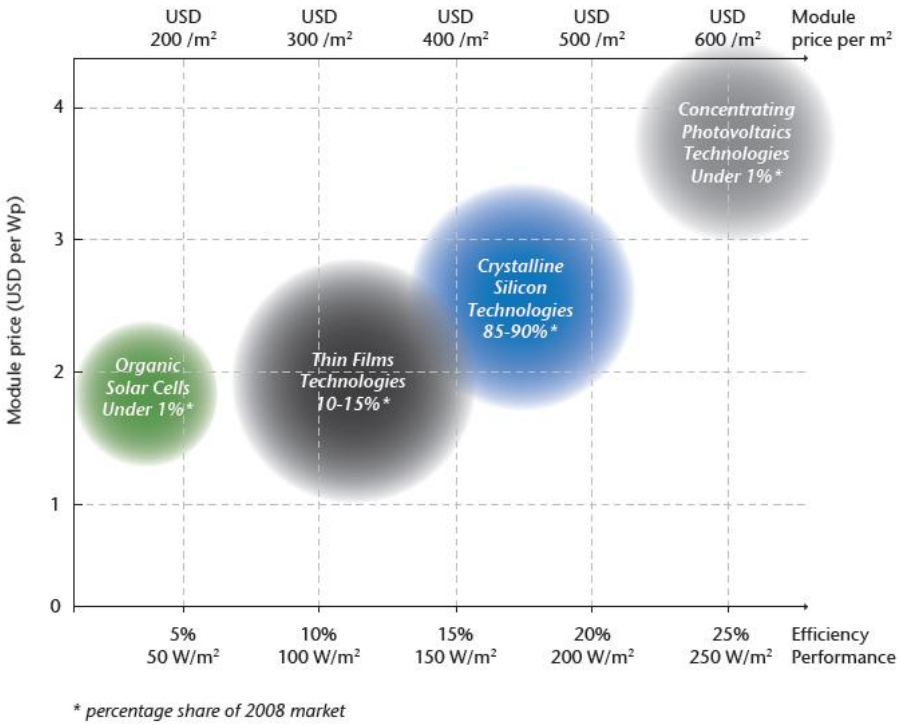


Figure 1.2: Performance and price of competing photovoltaic technologies at year end 2008 as in reference [3].

Although thin-film and organic solar cells are already cheaper than crystalline-Si modules they share only 10-15% of the market. This is due to the relatively high cost of installing these modules as well as the large area required for significant deployment given their low power output per unit area. Concentrating photovoltaic technologies are still the most expensive technology but have the potential for dramatically lower costs if the efficiency and concentration ratios of optical elements can be increased as well as the photovoltaic conversion efficiency of the component multi-junction solar cells. It is predicted that bulk electricity generation from concentrating photovoltaics with 50% efficient solar cells will be cost effective without government subsidies in all of southern Europe and a large portion of the US [4].

1.3. Solar cell device physics

1.3.1 Semiconductors and extrinsic doping

Semiconductor materials have conductivities between those of insulators and conductors. They have discrete energy bands, which can be populated by electrons, electrons in the semiconductors conduction band are free to move within the material and contribute to current flow. Electrons in the next lowest energy band, the *valence band*, do not contribute to flow but at very low temperatures, the valence band is full and the conduction band empty, so the semiconductor behaves as an insulator. At higher temperatures energy is supplied to electrons that cross the gap from the valence band to the conduction band. Through this process a vacant state is created in the valence band termed a *hole* which behaves like a positive charge carrier with the same magnitude of charge but opposite sign to an electron. In an intrinsic semiconductor the number of electrons in the conduction band and number of holes in the valence band must be equal and their concentration is known as the intrinsic carrier concentration, n_i. This carrier concentration is dependent on the semiconductor material and its temperature (silicon: $n_i = 1.4 \times 10^{10}$ cm^{-3} at 300 K). The forbidden energy band between the conduction and valence band is characteristic of each semiconductor material and is known as the bandgap where silicon and GaAs have bandgaps of 1.1 eV and 1.41 eV respectively at 300 K.

To increase the carrier population above intrinsic levels, and reduce resistivity, semiconductor materials are 'doped' by adding impurities to the crystal. Considering a Group IV element such as silicon which has 4 covalent bonds in a pure crystal, adding a Group V material such as Phosphorous to the lattice leads to an excess electron with no bond (n-type semiconductor). Similarly adding Boron (Group III element) leads a Boron atoms three outer electrons forming covalent bonds with silicon atoms but a fourth silicon atom forms a weak bond with the Boron atom which leads to an excess hole concentration (p-type semiconductor). The doping carrier concentrations of holes and electrons in semiconductors are typically given as N_A and N_D which are the concentration of acceptors and donors respectively.

1.3.2 Carrier transport and p-n junctions

An electric field applied to a semiconductor will produce a force on electrons and holes and the mobile ones experience an acceleration and movement. Carrier movement under influence of an electric field is known as *drift*. A drift current exists that is the net movement of charge and is proportional to the electric field and the charge mobility, $\mu_{n,p}$ *(cm^2/Vs)*, that describes how well a

particle will move due to an electric field. Equation 1.1 describes the drift current density for electrons and holes, $J_{n,p}$, where it is noted that electrons have a negative electronic charge, q, and move in the opposite direction to the electric field, $\hat{E}$.

$$\textbf{For electrons}: J_{n,} = -(qn)\left(-\mu_n \hat{\mathrm{E}}\right) = q\mu_n n\hat{\mathrm{E}} \qquad \textbf{For holes}: J_p = q\mu_p p\hat{\mathrm{E}} \qquad (1.1)$$

A second mechanism that induces a current in a semiconductor is *diffusion* whereby mobile carriers move from regions of high to low concentration. In this case the diffusion current is proportional to the carrier density gradient of electrons or holes (Equation 1.2). Additionally a term called the diffusion coefficient, $D_{n,p}$ *(cm^2/s)*, is introduced which describes how well a carrier diffuses.

$$\textbf{For electrons}: J_n = qD_n \frac{dn}{dx} \qquad \textbf{For holes}: J_p = -qD_p \frac{dp}{dx} \qquad (1.2)$$

Interfacing regions of n-type and p-type doping forms a semiconductor p-n junction. A common method of forming a p-n junction is by diffusing gaseous Phosphorous atoms into n-type silicon bulk wafers in a furnace at high temperatures to produce a p-doped region. At the p-n interface, the excess of *p* and *n* carriers leads to a diffusion of these majority carriers across the junction. This creates a build up of charge at the junction that induces an electric field (Figure 1.3). The electric field drives mobile charge in the opposite direction to the diffusion current. When this drift current balances the diffusion current, equilibrium is reached. A depletion region is formed which is characterised by its lack of mobile charge carriers while the remaining *n* and *p* type regions maintain their charge neutrality and are termed quasi-neutral regions (QNR). At this condition the net current flow in the junction is zero.

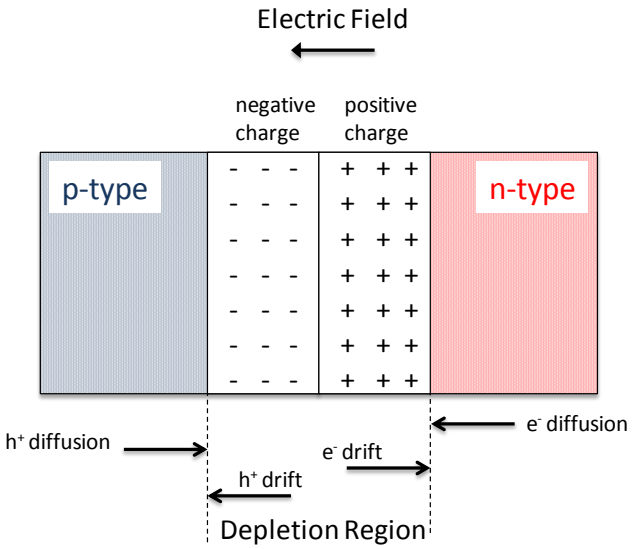


Figure 1.3: Schematic representation of the depletion region, electric field, quasi-neutral p & n regions and the forces acting on the carriers in a p-n junction.

Combining Equations 1.1 & 1.2 gives four possible independent current mechanisms which can be used to describe current flow in a p-n junction (Equation 1.3). A contribution is seen from the drift current for electrons and holes and the diffusion currents for electrons and holes where the total current density at any region in a p-n junction is the sum of all four.

$$J = J_n + J_p = q\mu_n n\hat{\mathrm{E}} + qD_n\frac{dn}{dx} + q\mu_p p\hat{\mathrm{E}} - qD_p\frac{dp}{dx} \qquad (1.3)$$

A p-n junction is operating in *forward* bias when a positive bias is applied to the p-type region. The bias is of opposite polarity to built-in electric field that exists in the depletion region and reduces the field strength. The smaller electric field at the depletion region reduces the barrier confining the majority electrons and holes to the n and p regions respectively. The majority electrons diffuse across the depletion region to the p-region (and vice versa for holes) where they become minority carriers and recombine i.e. the minority carrier concentration reduces away from the depletion region (Figure 1.4 (a)). This recombination of minority carriers is termed the diffusion current and as shown later its magnitude is an important parameter in determining the voltage of a solar cell.

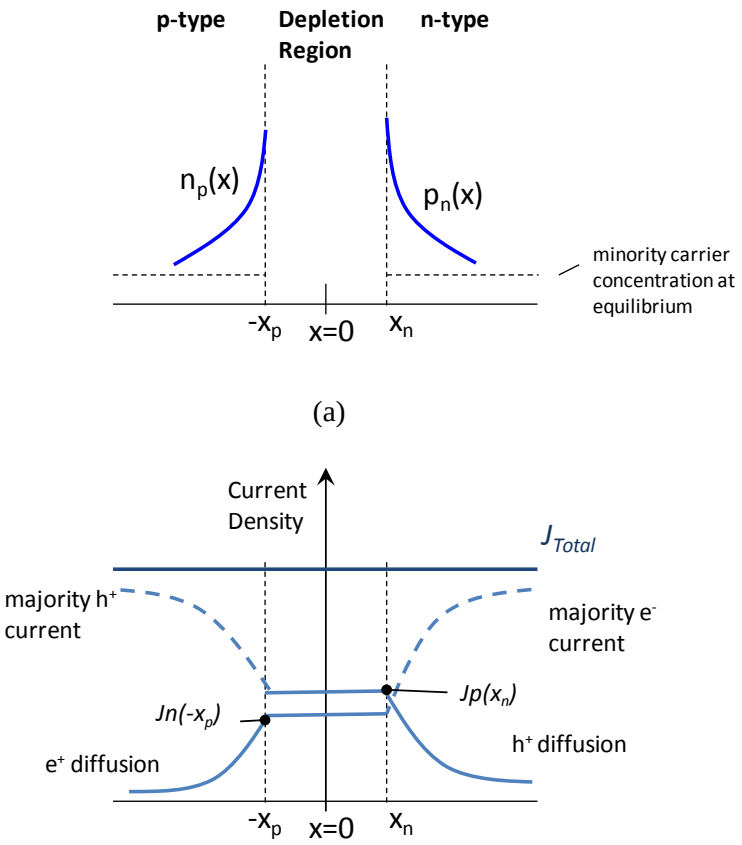


Figure 1.4: (a) Steady-state minority carrier concentration in a p-n junction under forward bias and (b) ideal electron and hole current components through a p-n junction under forward bias.

A number of assumptions allow us to determine the total current across a p-n junction under forward bias. Firstly it is assumed the electric field created in the depletion region is confined to the depletion region i.e. there is no drift current in the QNRs. Additionally it is assumed there is no generation or recombination of carriers in the depletion region and the currents through it are constant. This allows the minority carrier diffusion currents to be used to derive the current-voltage relationship of the p-n junction. At the depletion region edges a hole and minority carrier diffusion current exist that are combined to give the total current density i.e. J_n is found at $-x_p$ and J_p is found at x_n (Figure 1.4(b)). The diffusion current equations can be combined with formulae for the carrier densities [5] to give the ideal current-voltage relationship of a p-n junction (Equation 1.4).

$$J(V) = J_{o1}\left(e^{qV/kT} - 1\right) \tag{1.4}$$

where

$$J_{o1} = qn_i^2\left[\frac{D_p}{N_A L_p} + \frac{D_n}{N_D L_n}\right] \tag{1.5}$$

J_{o1} is called the reverse saturation current density. L_p and L_n are known as the hole and electron minority carrier diffusion lengths that describe the average length a minority carrier will travel in a material before recombining. The diffusion length is linked to the lifetime of carriers through the relation $L = (D\tau)^{0.5}$. The diffusion length is a key parameter for real solar cells and, as it determines the diffusion current, it has a significant bearing on the voltage of the solar cell (Equation 1.11) where greater diffusion lengths are desirable as they lead to lower reverse saturation current densities. Minority carrier diffusion length is referred to throughout this thesis as a useful measure of solar cell material quality (Table 1.1).

The assumptions used to derive the ideal current-voltage relationship of a p-n junction neglect any effects occurring in the depletion region. The actual relationship deviates from ideal due to additional currents in the depletion region caused by recombination. Imperfections in the semiconductor crystal lead to energy states which exist in the material bandgap to which electrons and holes can relax and recombine with other carriers. Under forward bias electrons and holes are injected into the depletion region where recombination of some of these excess carriers will occur. The recombination rate of excess electrons and holes is given by the Shockley-Read-Hall (SRH) formula (Equation 1.6) where τ_n and τ_p are the lifetimes for the capture of electrons and holes respectively by the trap and n_t and n_p are the trap densities. In its simplest form U will increase when np increases, although τ is also dependent on n and p.

$$U = \frac{np - n_i^2}{\tau_n(p + p_t) + \tau_p(n + n_t)} \tag{1.6}$$

Adding additional terms for the carrier concentrations, n and p [5], allows the formula to be used to find a recombination current for excess carriers in the depletion region (Equation 1.7) where, W, is the depletion region width and n is the diode ideality which for the recombination current should be ~2.

$$J_{o2} = \frac{qWn_i}{2\tau} exp^{\left(\frac{qV}{nkT}\right)} \quad (1.7)$$

The total forward-bias current density in a p-n junction is the sum of the recombination and ideal diffusion current densities which provides the double-diode equation of a p-n junction (Equation 1.8).

$$J(V) = J_{o1}\left(e^{\frac{qV}{kT}} - 1\right) + J_{o2}\left(e^{\frac{qV}{nkT}} - 1\right) \quad (1.8)$$

The double diode equation introduces the concept of a diode ideality *n*. For a large forward-bias voltage, the diffusion term, J_{o1}, dominates and theoretically varies according $e^{qV/kT}$. For lower forward-bias voltages recombination in the junction region, J_{o2}, dominates and varies according to the same exponential with an additional ideality, *n,* term which theoretically is equal to 2. In practice the diode idealty, *n*, ~ 2 and an additional ideality is seen in the exponential of the diffusion term. Idealities reveal the nature of the recombination and diffusion currents in a p-n junction solar cell.

The *dark current-voltage* (DJV) relationship of a solar cell is typically measured and plotted on a log scale to show the relationship versus bias. Figure 1.5 outlines the *DJV* relationship of an InGaAs cell (introduced in Chapter 4) where two distinct recombination regions are seen. Treating the low and high bias regions separately allows estimations to be made for the diode parameters. Neglecting the diffusion and *-1* terms in Equation 1.8 and taking its natural log we obtain:

$$\ln(J) = V.\frac{q}{nkT} + \ln\left(J_{o2}\right) \quad (1.9)$$

Estimations are made for the recombination parameters in the depletion region by plotting *DJV* on a log scale and taking J_{o2} as the intercept of the y-axis and the ideality, *n*, equal to the *q/mkT* where *m* is the line slope. The same analysis can be completed for the diffusion current where the ideality is theoretically equal to one.

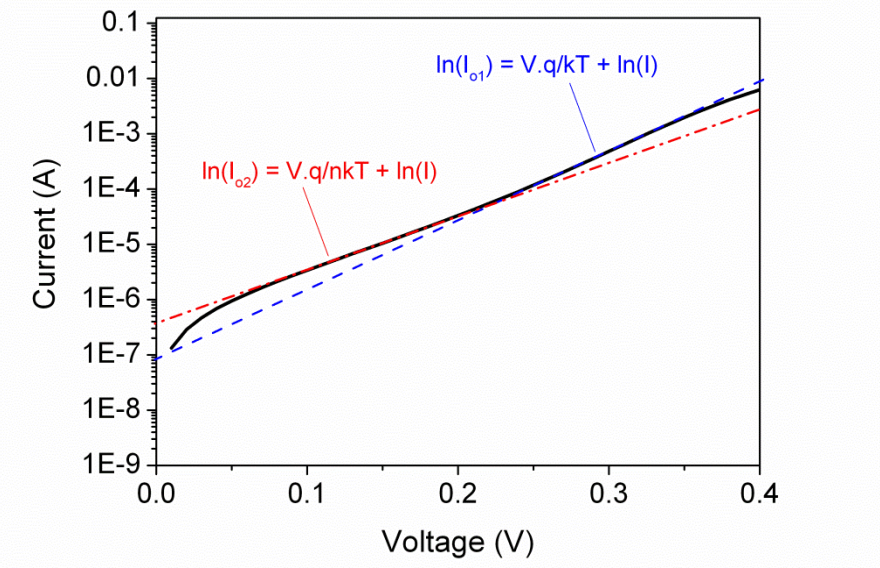


Figure 1.5: Measured *DJV* of an InGaAs solar cell (described in Chapter 4) with two regions of recombination identified. A straight line is fitted to each region and representative equations shown.

1.3.3 p-n junction under illumination

Illuminating a p-n junction with an incident spectrum and connecting a load allows the extraction of power (*J.V*) from the device and is the basic operating principle of a solar cell. The first key process in the photovoltaic effect is the absorption of photons incident on a material. Semiconductors can either be 'direct' or 'indirect' bandgap materials which determine their absorption properties. For direct bandgap materials such as GaAs, the minimum of the conduction band and maximum of the valence band are aligned with the same crystal momentum (Figure 1.6). A photon is absorbed by transferring its energy to an electron in the valence band, where the electron is excited across the material to the conduction band. For an indirect bandgap material, such as silicon, the minimum and maximum are not aligned and, as well as photon absorption, a second momentum energy transfer from a phonon to an electron is required to excite it across the bandgap. The probability of this additional energy transfer reduces the likelihood of a photon being absorbed.

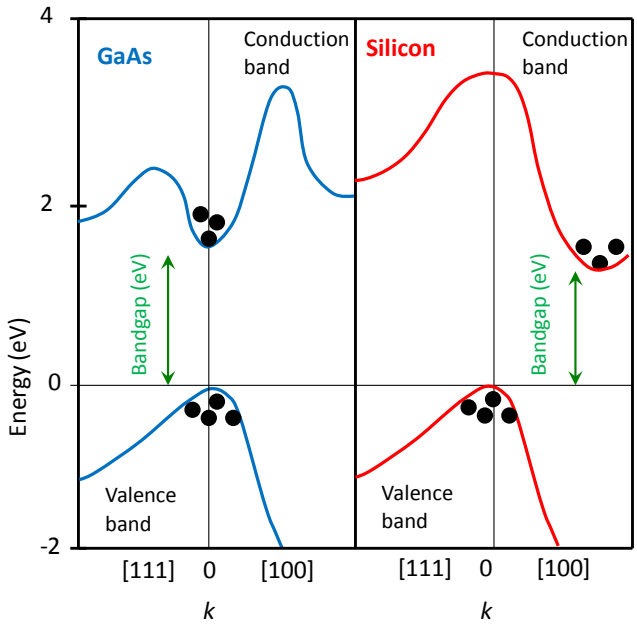


Figure 1.6: Energy band structures of GaAs and silicon as in [5].

A semiconductors absorption coefficient, α (cm^{-1}), is a measure of the number of photons absorbed, per unit thickness of the material. The absorption coefficients of silicon and a number of III-V direct bandgap materials are given in Figure 1.7. A semiconductors absorption curve is derived through knowledge of the energy band diagram of the material. Silicon, an indirect bandgap material, exhibits a lower absorption coefficient for long wavelength photons near its band edge (1100 nm) where phonon energy transfer is required, but at shorter wavelengths (< 400 nm) its absorption coefficient is very large as direct transitions are possible at these energies (Figure 1.6). The III-V materials exhibit strong absorption at all wavelengths below their bandgap. The Standard Solar Spectrum (AM1.5G) is given for comparison it is clear that $In_{0.53}Ga_{0.47}As$ solar cells, with a bandgap of 0.74 eV at 300 K, will absorb the largest portion of the solar spectrum producing a greater photocurrent density than the other III-V materials. Some materials such as aluminium gallium arsenide can be dominated by either direct or indirect optical absorption as their energy band structure changes depending on the composition of each element. The absorption curve of $Al_{0.3}Ga_{0.7}As$ is given in Figure 1.7 which is dominated by direct absorption. $Al_xGa_{1-x}As$ with Al compositions greater than 40% are dominated by indirect absorption.

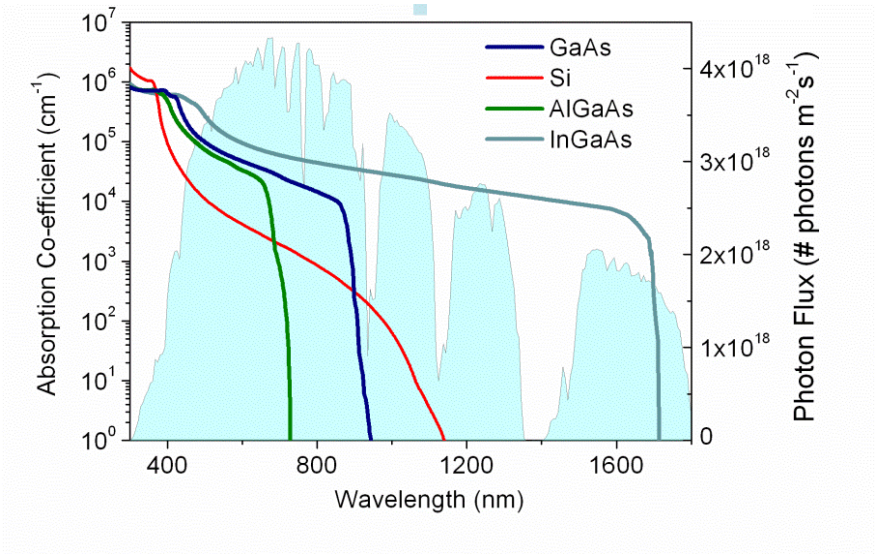


Figure 1.7: Absorption coefficient as a function of wavelength for Si, GaAs, $In_{0.53}Ga_{0.47}As$ and $Al_{0.3}Ga_{0.7}As$ [5], [6]. Also shown is the photon flux of the AM1.5G standard solar spectrum as a function of wavelength.

As photons are absorbed in a semiconductor of thickness, *t*, the intensity of the incident spectrum reduces according to the Beer-Lambert law (Equation 1.10). The number of electron-hole pairs generated can be found, as a function of wavelength, by calculating the light intensity after travelling through thickness, *t*, and subtracting from the original intensity.

$$I(\lambda, t) = I_o e^{-\alpha\lambda(t)} \tag{1.10}$$

In a p-n junction solar cell under illumination, electron-hole pairs are created throughout the material where the greatest concentration is near the front of the device. While this generation does not greatly alter the majority carrier concentration, the minority carrier concentration greatly increases and these minority carriers diffuse towards the junction where they are swept across by the electric field. These become majority carriers and either recombine or are collected at the solar cell contacts where they contribute to the light-generated current and voltage. This light-generated current acts in the opposite direction to both the junction recombination and diffusion currents. A light-generated current density term, J_L, is now added to the double diode equation (Equation 1.11). The magnitude of this photocurrent is dependent on the absorption coefficient, thickness, and carrier transport properties of the solar cell but is independent of the applied voltage and added as a lumped term.

$$J(V) = J_{o1}\left(e^{\frac{qV}{kT}} - 1\right) + J_{o2}\left(e^{\frac{qV}{nkT}} - 1\right) - J_L \qquad (1.11)$$

We now have an idealised current-voltage relationship for a solar cell where the power density delivered by the cell = -*J.V*. The equivalent circuit and typical current-voltage relationship of a solar cell in the light and dark are given in Figure 1.8. The illuminated behaviour of a solar cell is a superposition of its current-voltage behaviour in the dark and the photocurrent generated.

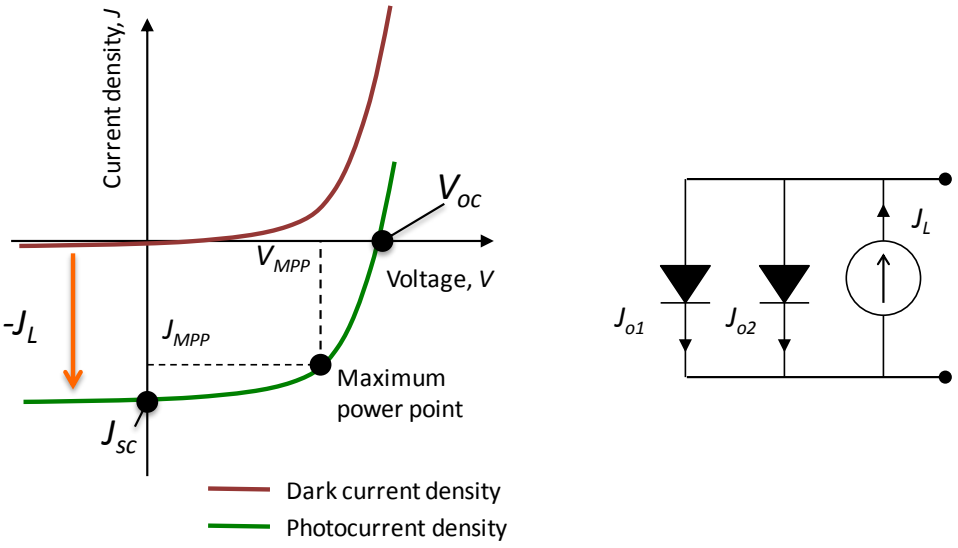


Figure 1.8: Current-voltage characteristics of a p-n junction solar cell under illumination and in the dark as well as the equivalent circuit diagram.

A number of key solar cell parameters outlined in Figure 1.8 are used throughout this thesis to describe solar cell behaviour. They are the open-circuit voltage, V_{oc} *(V)*, where the light generated current exactly balances the recombination and diffusion currents. A relationship between V_{oc} can be derived from Equation 1.4:

$$V_{oc} = \frac{kT}{q} ln\left(\frac{J_{sc}}{J_{o1}}\right) \qquad (1.12)$$

The short-circuit current density, J_{sc} *(mA/cm^2)*, which is the current-density at zero bias, and the maximum power point(V_{MPP}, I_{MPP}) are also outlined. A fill factor term, *FF (%)*, is also used in this thesis to compare cells (Equation 1.13) that is a ratio of the actual power produced by the cell to the idealised case:

$$FF = \frac{J_{MPP}V_{MPP}}{J_{sc}V_{oc}} \quad (1.13)$$

The efficiency (Equation 1.14) is given by the ratio of the power produced by the solar cell to the power of light incident on its front surface which for standard test conditions (AM1.5G) is taken as 1kW/m^2.

$$PV\ efficiency\ (\%) = \frac{J_{MPP}V_{MPP}}{P_{in}} \quad (1.14)$$

1.3.4 Recombination in solar cells

Additional recombination mechanisms are seen in the bulk regions of p-n junctions. There are three main recombination types within the bulk semiconductor itself. Non-radiative recombination that occurs through traps located in the energy gap where an excited carrier relaxes to the energy of the trap before a second relaxation process to the valence band (Figure 1.9). The energy lost is given off as heat into the lattice and so is termed *non-radiative* recombination. For recombination through a single trap state the rate is given by the Shockley-Read-Hall (SRH) formula previously given (Equation 1.6).

Radiative recombination is the relaxation of an electron from the conduction band to the valence band through the emission of a photon (Equation 1.15, where *B* is the radiative recombination coefficient). This is the primary recombination source in direct bandgap materials such as GaAs. Radiative recombination is a rapid process as compared to other recombination types.

$$R_{rad} = B(pn - n_i^2) \quad (1.15)$$

$$R_{Auger} = \left(C_n n + C_p p\right)\left(np - n_i^2\right) \quad (1.16)$$

A third recombination source in semiconductor materials is Auger recombination which requires an electron-hole pair and another carrier. The electron and hole recombine across the bandgap but the energy is transferred to another electron in the conduction band or a hole below the valence band. Equation 1.16 is the general equation for Auger recombination where $C_{n,p}$ are the Auger

coefficients. Auger recombination becomes a fast process in highly doped semiconductors as there is a high concentration of carriers available to take part in the process.

Carrier lifetimes in semiconductors materials are a combination of the lifetimes due to each recombination process (Equation 1.17).

$$\frac{1}{\tau_{Total}} = \frac{1}{\tau_{SRH}} + \frac{1}{\tau_{rad}} + \frac{1}{\tau_{Auger}} \tag{1.17}$$

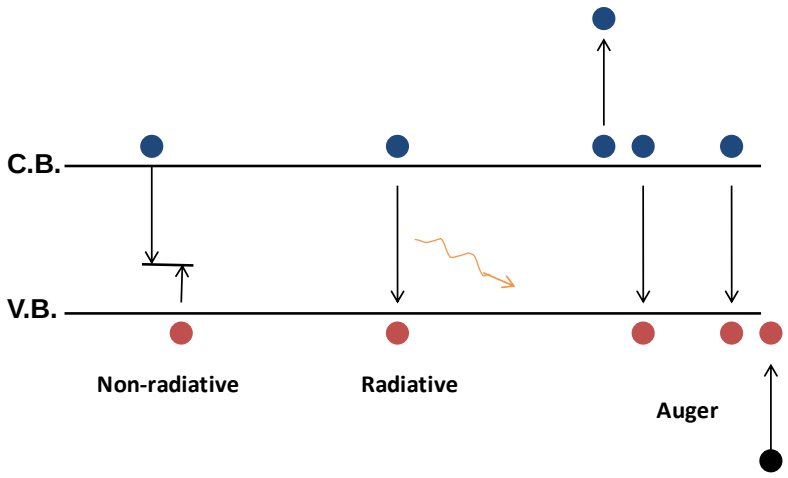


Figure 1.9: Outline of the three principal recombination types in bulk semiconductor materials.

Recombination also occurs at the surface of semiconductor materials. When a semiconductor is abruptly terminated, the periodicity of the lattice structure is broken and defects are created. This leads to the creation of energy states within the bandgap which contribute to recombination. In practice, solar cells are typically passivated to reduce the number of dangling bonds at the surface and reduce the surface recombination rate. Silicon solar cells are passivated using dielectrics such as SiO_2 or SiN_x. For III-V materials hetero-structures are formed with wide E_g materials placed between the bulk solar cell and the front or back surface which acts as potential barriers reducing the number of minority carriers that travel to a surface and recombine.

The following Table 1.1 provides a brief summary of the typical values expected for the minority carrier transport and optical properties of silicon and GaAs solar cells. As a direct bandgap material the diffusion lengths and lifetimes in GaAs are shorter than for silicon. Given the larger absorption coefficients for GaAs, however, thin cells absorb most of the incident solar radiation. Therefore GaAs cells are the state of the art for single-junction cells with a champion cell

efficiency of 28.8% efficiency under 1-Sun conditions [7]. Auger and SRH recombination limits the lifetime and ultimate efficiency of silicon solar cells where radiative recombination is negligible in the indirect bandgap material. Auger recombination is slow in low doped materials but lifetimes can reduce to a few nanoseconds at very high doping levels [8]. The longer lifetimes and diffusion lengths in silicon allow the photons absorbed deep in the device to travel to the junction without recombining. Therefore thicker cells are used to overcome lower absorption coefficients as compared to GaAs. Recombination in material defects (SRH) is also present in both silicon and GaAs where the defect density in commercially available GaAs wafers is higher than silicon.

Table 1.1: Key differences in material and optical properties between silicon and GaAs solar cells.

	Silicon	**GaAs**
Eg (300 K)	1.1 eV	1.41 eV
Absorption	Indirect: Cell thickness ~ 200 µm	Direct: Cell thickness ~ 5 µm
Primary recombination mechanisms	Auger, SRH	Radiative, SRH
Minority carrier lifetime	~ 1 µs [9]	~ 1 - 50 ns [10]
Minority carrier diffusion length	~ 100 - 300 µm [9]	~ 1 - 20 µm [10]
Commercial wafer defect density	10 – 30 cm^{-2}	1000 – 5000 cm^{-2}
Surface recombination reduction	SiO_2 passivation	Wide E_g hetero-interface

1.3.5 Quantum Efficiency

Quantum Efficiency (QE) measurements are a measure of the ratio of electrons extracted from a solar cell to the number of photons incident upon the cell and are taken as a function of wavelength. For different photon energies, carriers are excited at different depths in the cell as indicated by the absorption co-efficient of the material which varies with wavelength. Analysis of a cell's quantum efficiency versus incident wavelength reveals information about the likelihood of carrier extraction for photons absorbed at various depths in the device. This allows estimations to be made for the minority carrier diffusion lengths, minority carrier lifetimes and surface recombination velocities of the solar cell layers which are the primary parameters which affect carrier collection probability. The External Quantum Efficiency (EQE), Internal Quantum

Efficiency (IQE) and Reflection of solar cells is presented throughout this thesis and were measured using a Bentham Instruments PVE300 PV Characterisation System (Appendix A). A standard model [11] was used to fit the EQE data to provide estimates for the diffusion lengths and surface recombination velocities of fabricated solar cells.

The standard model is described as follows: The IQE of an ideal solar cell with a finite base thickness, x_b, emitter thickness, x_e, and depletion width, W_d, (Figure 1.10) is equal to the sum of the contribution from each of these regions as in Equation 1.18.

$$IQE = IQE_{emitter} + IQE_{depl} + IQE_{base}.e^{[-\propto(x_e+W_d)]} \tag{1.18}$$

where

$$IQE_{emitter} = f_{\propto}(L_e)\left(l_e + \propto L_e e^{(-\propto x_e)} \times \frac{l_e \cosh\left(\frac{x_e}{L_e}\right) + \sinh\left(\frac{x_e}{L_e}\right)}{l_e \sinh\left(\frac{x_e}{L_e}\right) + \cosh\left(\frac{x_e}{L_e}\right)} - \propto L_e e^{(-\propto x_e)} \right) \tag{1.19}$$

$$IQE_{base} = f_{\propto}(L_b)\left(\propto L_b - \frac{l_b \cosh\left(\frac{x_b}{L_b}\right) + \sinh\left(\frac{x_b}{L_b}\right) + (\propto L_b - l_b)e^{(-\propto x_b)}}{l_b \sinh\left(\frac{x_b}{L_b}\right) + \cosh\left(\frac{x_b}{L_b}\right)} \right) \tag{1.20}$$

$$f_{\propto}(L) = \frac{\propto L}{(\propto l)^2 - 1} \tag{1.21}$$

where absorption in the proceeding emitter and depletion regions is accounted for in Equation 1.18. The contribution from the depletion region consists of all photons absorbed in this region as it is assumed all carriers are extracted from this region (Equation 1.22).

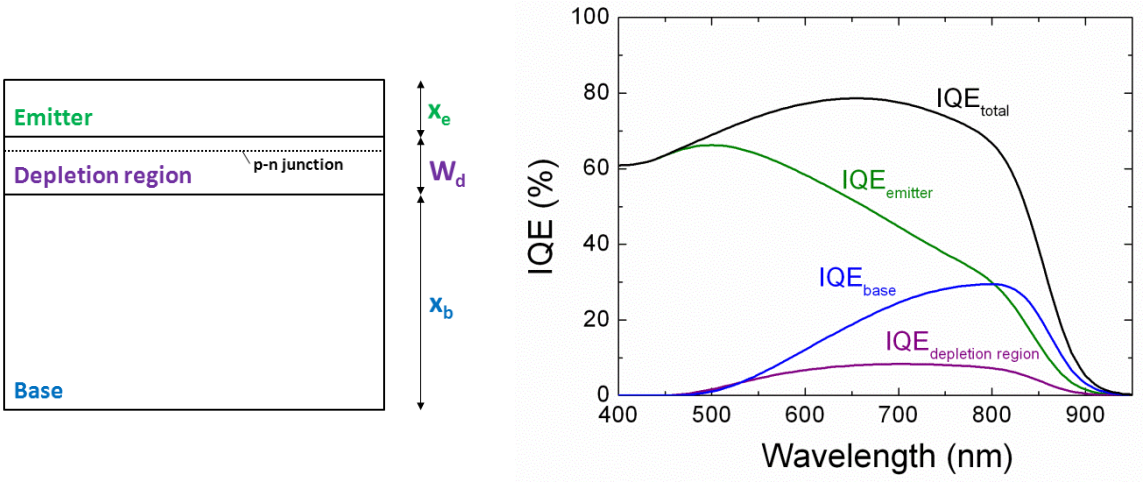
$$IQE_{depl} = e^{(-\propto x_e)}\left[1 - e^{-\propto W_d}\right] \tag{1.22}$$

The quantities μ, L and S are, respectively, the mobility, diffusion length and surface recombination velocity of minority carriers in the base or emitter regions.

$$l_b = \frac{S_b L_b}{D_b}, l_e = \frac{S_e L_e}{D_e}, D_b = \frac{kT\mu_b}{q}, D_e = \frac{kT\mu_e}{q} \quad (1.23)$$

$$EQE(\lambda) = \big(1 - R(\lambda)\big).\big(1 - A(\lambda)\big).IQE(\lambda) \quad (1.24)$$

The EQE (Equation 1.24) is the internal quantum efficiency less the wavelength dependent reflection and absorption losses. Absorption in the dielectric materials used for anti-reflection coating and window layers is accounted for using the measured extinction coefficient of the material through the Beer-Lambert law (Equation 1.10). An outline of the expected contribution to the total IQE (Equation 1.18) in a GaAs solar cell is given in Figure 1.10 (b). The base contribution is low due to the thin layer of 500 nm modelled.



(a) (b)

Figure 1.10: (a) schematic outline of the emitter, depletion and base regions of a GaAs solar cell and (b) the contribution of each region to the overall IQE of a cell.

1.4. Multi-junction solar cells for concentrating photovoltaics

The performance of solar cells made from a single p-n junction is restricted by the broad range of wavelengths present in the solar spectrum (Figure 1.11). The maximum photocurrent that can be extracted by a solar cell is determined by the bandgap of the semiconductor material used, as only photons with energy greater than this bandgap are absorbed efficiently. Photons absorbed with energy greater than the material bandgap lose this excess energy through a process known as thermalisation by transferring heat to the crystal lattice. The solar cell photovoltage is a function of the material bandgap (Eg) i.e. the voltage increases with *Eg* while the photocurrent decreases with bandgap. The balance of bandgap choice for high absorption and high photovoltage means a value of approximately 1.4 eV is optimum for single-junction solar cells. Si has a bandgap of 1.1 eV and so it is limited to a maximum theoretical photovoltaic conversion efficiency of 33% [12]. To date the highest photovoltaic conversion efficiency achieved by any Si solar cell in the laboratory has been 25% [13]. The bandgap of GaAs (1.42 eV at 300 K [14]) is closer to the optimum for single-junction cells with flat-plate modules currently being developed by Alta Devices [15] but the cost of using compound semiconductors for large area modules may be prohibitive to large scale adoption.

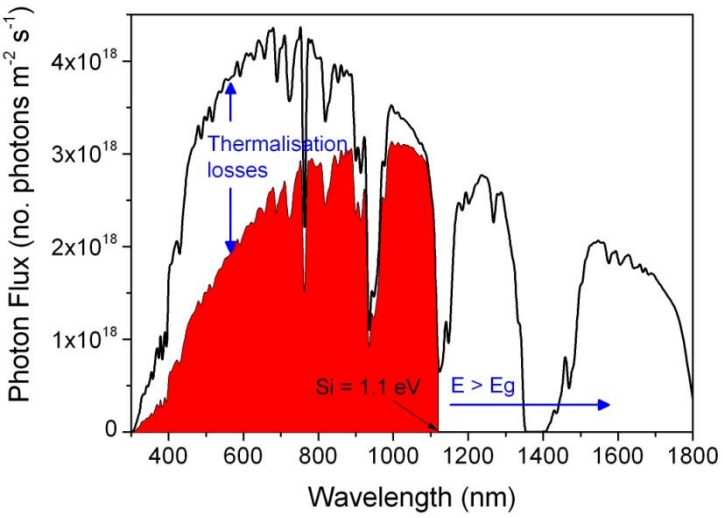


Figure 1.11: ASTM G173-03 Air Mass 1.5 direct reference solar spectrum. The red area represents the portion of the spectrum absorbed by a Si solar cell.

1.4.1. Better spectrum utilisation

Multi-junction solar cells are formed by combining a number of p-n junctions in one photovoltaic structure. Each junction absorbs a different portion of the solar spectrum producing a photocurrent in each. The junctions are stacked so that the incident solar spectrum is first absorbed by the material with the highest bandgap with each junction underneath being of a lower bandgap as shown in Figure 1.12. By utilising three junctions these solar cells can convert twice as much of the solar spectrum into useful electrical energy when compared with single-junction Si devices with currently seven research institutes/companies reporting externally verified conversion efficiencies of over 40% [16]–[21]. These technologies are summarised in Table 1.2 and discussed in greater detail in Chapter 2.

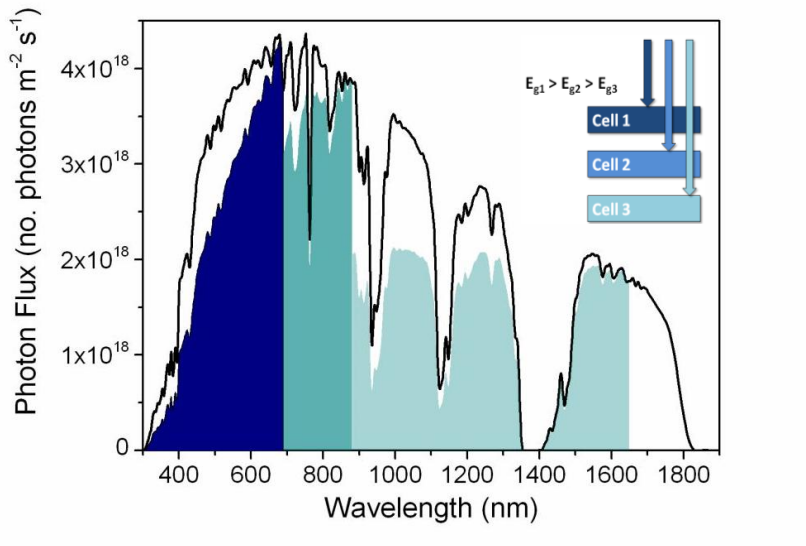


Figure 1.12: ASTM G173-03 Air Mass 1.5 direct reference solar spectrum. The portion absorbed by each cell in a triple junction solar cell is highlighted.

Commercially available multi-junction solar cells utilise the lattice matched GaInP/GaAs material system on Ge or GaAs substrates. The production of III-V devices is significantly more expensive than Si cell production due to material and processing costs. Multi-junction solar cells were initially utilised in space applications where specific power (W/kg) and radiation hardness are the key performance criteria and their cost was not prohibitive. More recently monolithic multi-junction solar cells are being used in terrestrial concentrating photovoltaic systems where inexpensive optics focus sunlight onto small photovoltaic cells thus reducing the amount of semiconductor material required.

Table 1.2: Summary of the state of the art photovoltaic devices with confirmed lab efficiencies of greater than 40% under concentration.

Champion efficiency	Concentration ratio (suns)	Material combination	Company/ Research Institute	Measurement lab	Year
44%	947	Unpublished (Probably lattice matched GaInP/GaAs/GaInNAs)	Solar Junction	NREL	2013
43.5%	306	Inverted metamorphic GaInP/GaAs/InGaAs	Sharp	Fraunhofer ISE	2013
42.6%	327	Inverted metamorphic GaInP/GaAs/Ga(In)As	NREL	NREL	2012
42.4%	325	Inverted metamorphic GaInP/GaAs/GaInAs	Emcore	NREL	2012
42.3%	406	Bi-facial growth GaInP/Ga(In)As –GaAs substrate- GaInAs	Spire	NREL	2011
41.6%	364	Lattice matched GaInP/Ga(In)As/Ge	Spectrolab	NREL	2009
41.1%	454	Metamorphic GaInP/GaInAs/Ge	Fraunhofer ISE	Fraunhofer ISE	2009

1.4.2. Concentrating Photovoltaics

Concentrating photovoltaic (CPV) systems are seen as a promising route to the generation of renewable energy electricity at prices competitive with fossil fuel sources. CPV systems use refractive (lenses) or reflective (mirrors) optics to focus sunlight onto a small photovoltaic cell as in Figure 1.13. This reduces the required area of the solar cell and allows the use of devices made from III-V semiconductor materials. In a typical system the solar cell area is 500 times less than the total area of captured light while the feasibility of up to 1000 suns concentration is under investigation in order to further drive down the cost of these systems [22]. A secondary optic is typically attached to the cell to increase concentration and alignment tolerance and homogenize the incident beam while the use of concentrating optics predicates the use of tracker systems to collect direct radiation from the sun. CPV systems are suited to large ground-mounted installations in areas with high direct-normal irradiance with tracking providing a higher energy yield (kWh/installed kW) than flat-plate Si modules. As with all photovoltaics clear skies are desirable but this is more pronounced in CPV systems as diffuse radiation is not collected.

CPV systems benefit from the increased performance of solar cells with increasing illumination. For an increase in illumination intensity, X (suns), the photocurrent produced, I, scales linearly, however, the photovoltage of a solar cell, V_{oc}, scales logarithmically with this increased photocurrent (Equation 1.25) where, P_{in}, is the power of the incident solar spectrum, FF, is the fill factor of the device and Io is the reverse saturation current density.

$$PV\ conversion\ efficiency = \frac{X.I.FF.V_{oc}}{X.P_{in}} \quad where \quad V_{oc} \sim ln\left(\frac{X.I}{I_o}\right) \tag{1.25}$$

CPV systems for Si solar cells use low concentration ratios (< 100 suns) as Si cell performance degrades more rapidly under increased temperature than III-V cells. Most CPV manufacturers utilise high performance multi-junction solar cells and high concentration ratios (~ 500 suns) to produce twice the power of an industry standard flat-plate silicon PV panel with Semprius recently demonstrating a world record module efficiency of 33.9% [23]. CPV installations climbed to 50 MW worldwide in 2011 [24].

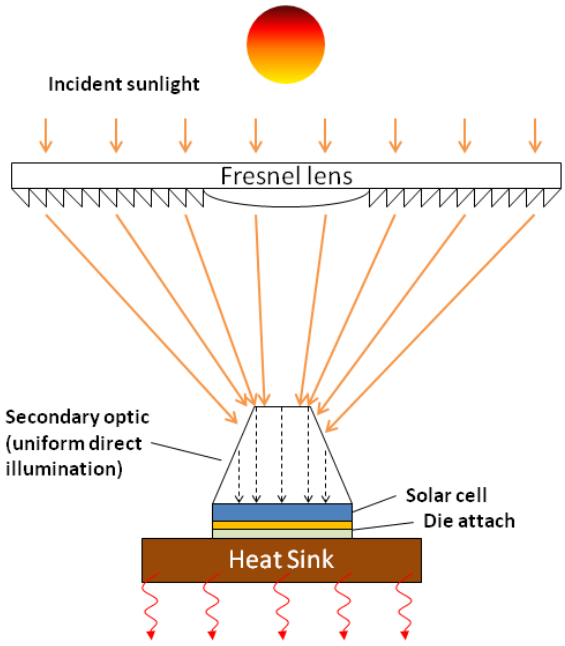


Figure 1.13: Schematic outline of a concentrating photovoltaic system. The optical and thermal design elements are shown.

The high power density of incoming sunlight in CPV systems subjects the solar cells to high performance criteria when compared to other PV devices. The ohmic resistance of solar cells in CPV systems must be low as any resistance will increase under the elevated operating temperatures of CPV cells. Furthermore high thermal conductivity is required to remove the large thermal load of concentrated sunlight from the cell. Typically 40% of the incident radiation is converted to electricity with the remaining 60% is dissipated as heat. As the photovoltaic conversion efficiency of all solar cells decreases with higher temperature this load is removed to a mounted heat sink. The device temperature is typically maintained at 70^{o}C although lower is desirable.

1.5. Mechanically stacked solar cells

Greater than 50% cell efficiency has been identified as a tipping point at which large scale CPV deployment will be cost-effective without government subsidies. The current state of art monolithic multi-junction solar cells have broken the 40% efficiency barrier and are increasing by 0.5 – 1 % each year. In monolithic triple-junction devices the cells are connected in series using transparent and ohmic tunnel junctions to inter-connect individual cells. For series connected devices the photocurrent produced is limited to the lowest produced by any cell. Thus bandgap combinations which split the solar spectrum into equal currents in each junction are required. This is difficult given the constraints of monolithic device production where materials are grown at the same lattice spacing to reduce defects, resulting form strain between lattice mismatched materials, which adversely affect the electrical characteristics of cells. For a triple-junction device the optimum bandgap combination of 1.74, 1.17 and 0.7 eV is not found in any lattice matched material system [21]. The standard approach is to produce high performance triple-junction solar cells utilising the high quality lattice matched materials of $Ga_{0.5}In_{0.5}P$, $Ga_{0.99}In_{0.01}As$ and Ge. The Ge junction, however, produces twice the photocurrent of the top two junctions with this excess current wasted. The constraints of lattice and current matching limit the performance of these devices with alternative technologies required to reach the 50% efficient cell target.

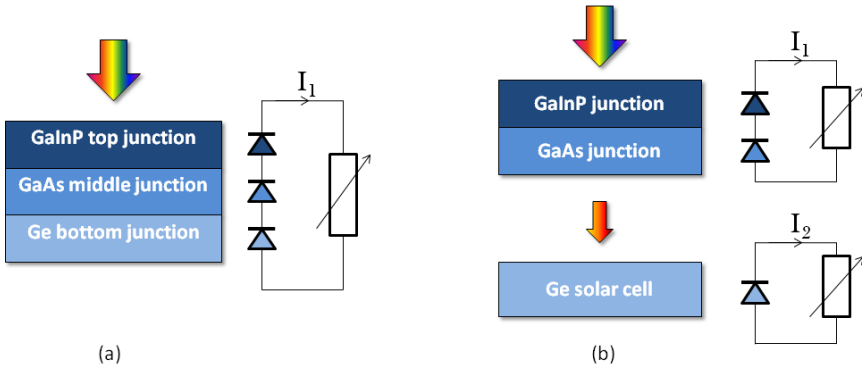


Figure 1.14: Outline of (a) a monolithic triple-junction solar cell and (b) a mechanically stacked triple-junction solar cell. Circuit diagrams are given to highlight the reduction of the current matching constraint in the stacked device. A Ge junction will produce approximately twice the current of the top cell (i.e. $I_2 \approx 2I_1$).

In order to improve multi-junction cell performance lattice matched materials which better split the solar spectrum are required or the integration of lattice mismatched materials with optimum bandgap combinations. Mechanically stacked solar cells (MSSC) are a technology which remove the constraints of monolithic devices by combining individual solar cells in a stack using techniques such as direct or epoxy bonding [25], [26]. They introduce better bandgap combinations for better current matching through the heterogeneous integration of lattice mismatched materials. Alternatively they improve the performance of multi-junction cells by providing electrical connection to individual junctions making up the stack, extracting the maximum current from each and eliminating the requirement for current matching. While the theoretical performance of mechanically stacked solar cells is greater than current triple-junction technology they suffer from drawbacks which are summarised and compared to monolithic devices in Table 1.3.

Table 1.3: Critical criteria for evaluating solar cell suitability for high performance and use in CPV systems. Monolithically inter-connected and mechanically stacked devices are compared.

	Monolithic multi-junction solar cells	**Mechanically stacked solar cells**
Photovoltaic performance	Constrained By bandgaps of available lattice matched alloys Lattice mismatched alloys can be integrated but so far limited to triple-junction solar cells	Potentially > 50% Potentially any bandgap combination possible Additional terminals remove current matching constraint
Optical losses	Relatively low Require broadband anti-reflection coatings for next-generation devices (i.e. four-junction)	Relatively high Require broadband anti-reflection coatings for low Eg bottom junction Reflection losses at interface between cells Non-useful absorption of photons in semiconductor substrates Metal contact grids must be aligned
Resistance	Low Balance between grid shading and resistance	Potentially high Resistance of direct-bond interfaces Complex contacting schemes introduce additional resistive elements (e.g. lateral conduction layers)
Thermal resistance	Low	High Airgap or epoxy interfaces have low thermal conductivities
Reliability	So far proven Commercially deployed cells given 20 year guarantee (space qualified) Tunnel junction process yield concerns	Thermal expansion issues Integration of materials with potentially large differences in thermal expansion coefficients, bonds may fail under stress of high temperature CPV use
Cost	Greater than flat-plate Si Innovation still required to compete with Si installations	High The use of additional solar cells and complex processing routes may be prohibitive to industry use

1.6. Objectives

The objectives of this thesis are motivated by the need to pursue photovoltaic technologies that will prove cost-effective in large scale CPV deployment through the advancement of solar cell efficiencies beyond 50%. Two strategies to improve multi-junction solar cell performance will be evaluated.

- The first is the integration of readily available solar cells of lattice-mismatched materials through novel stacking methods. A solar cell and terminal configuration that avoids the need for complex bandgap engineering or advanced epitaxy capability will be developed. In order to reach the cell performance predicted by theory the optical losses at the interface between the stacked cells will be reduced using adhesive bonding and suitable anti-reflection coating design. A fabrication route for a triple-junction GaInP/GaAs-$In_{0.53}Ga_{0.47}As$ solar cell with > 50% efficiency under concentration is presented. Prototype GaAs-$In_{0.53}Ga_{0.47}As$ tandem stacked cells are evaluated
- The second route investigates alternative lattice-matched *Eg* combinations that can be accessed on the InP lattice constant. A novel $In_{0.52}Al_{0.48}As$ solar cell has been identified, which can be used to provide an alternative to the well established GaAs solar cell. As wide bandgap InAlAs solar cells have not been extensively investigated for use in photovoltaics, single-junction cells will be fabricated and their properties relevant to PV operation analysed.

1.7. Thesis outline

This thesis presents theoretical and experimental work developing high-efficiency photovoltaics through mechanically stacked integration of solar cells with lattice constants based on the InP lattice constant. The chapters are organised as follows:

Chapter 2 reviews the state of the art in multi-junction solar cells with a particular focus on the combination of bandgaps of lattice mismatched semiconductor materials. The challenges and constraints of mechanically stacked solar cells based on GaAs top cells are reviewed as well as

efforts to integrate novel bandgap combinations in multi-junction devices at the GaAs or InP lattice constants.

Chapter 3 presents the simulation of the PV efficiency of mechanically stacked solar cells composed of AlGaAs, GaAs, Si and InGaAs cells. A parallel connected InGaAs cell stacked under a GaAs based dual-junction top cell is chosen as the most suitable route for high performance mechanically stacked solar cells. A design methodology is presented to determine the most suitable adhesive to bond such cells in a fashion which reduces the thermal and optical losses in the stack. Benzocyclobutene is chosen as the most suitable owing to its relatively high refractive index and thermal conductivity when compared to other potential bonding adhesives.

Chapter 4 outlines the development of single-junction solar cells lattice matched on InP. InGaAs solar cells were designed for use as the bottom cell in a mechanical stack under a GaAs based top cell. InAlAs solar cells were fabricated in order to probe the material's properties relevant to photovoltaic use. An experimental demonstration of alternative substrates for solar cells based on the InP lattice constant is provided by grading the lattice constant of a GaAs host substrate to that of InP onto which InAlAs and InGaAs solar cells are grown. The cells are compared to those grown on InP substrates in order to evaluate the effectiveness of the $In_xGa_{1-x}As$ grading layers.

Chapter 5 presents the process development and final results of a GaAs-InGaAs mechanically stacked solar cell. Single-junction GaAs solar cells on n-GaAs substrates were fabricated to form the top cell in a stack with an optical design completed to increase transmission of wavelengths in the 880 – 1700 nm range. Cell bonding, using Benzocyclobutene, is used to form III-V mechanically stacked solar cells.

Chapter 6 summaries the content of this thesis and recommends future work to further develop the concepts presented.

1.8. References

[1] "Global Market Outlook for Photovoltaics 2014 - 2018," European Photovoltaic Industry Association, May 2014.

[2] "$1/W Photovoltaic Systems, A Grand Challenge for Electricty from Solar," U.S. Department of Energy, Aug. 2010.

[3] "Technology Roadmap - Solar Photovoltaic Energy," International Energy Agency, 2010.

[4] R. R. King, D. Bhusari, D. Larrabee, X.-Q. Liu, E. Rehder, K. Edmondson, H. Cotal, R. K. Jones, J. H. Ermer, C. M. Fetzer, D. C. Law, and N. H. Karam, "Solar cell generations over 40% efficiency," *Prog. Photovolt. Res. Appl.*, vol. 20, no. 6, pp. 801–815, 2012.

[5] S. M. Sze, *Physics of Semiconductor Devices*. John Wiley and Sons, 1981.

[6] S. Adachi, *Physical Properties of III–V Semiconductor Compounds*. John Wiley and Sons, 1992.

[7] L. S. Mattos, S. R. Scully, M. Syfu, E. Olson, L. Yang, C. Ling, B. M. Kayes, and G. He, "New module efficiency record: 23.5% under 1-sun illumination using thin-film single-junction GaAs solar cells," in *2012 38th IEEE Photovoltaic Specialists Conference (PVSC)*, 2012, pp. 003187–003190.

[8] J. Schmidt, N. Thiemann, R. Bock, and R. Brendel, "Recombination lifetimes in highly doped aluminum-doped silicon," *J. Appl. Phys.*, no. 106, p. 093703, 2009.

[9] J. A. del Alamo and R. M. Swanson, "Modelling of minority-carrier transport in heavily doped silicon emitters," *Solid-State Electron.*, vol. 30, no. 11, pp. 1127–1136, Nov. 1987.

[10] M. R. Brozel and G. E. Stillman, *Properties of Gallium Arsenide*. INSPEC, 1996.

[11] A. Luque and S. Hegedus, *Handbook of Photovoltaic Science and Engineering*. John Wiley & Sons Ltd, 2011.

[12] M. A. Green, "Radiative efficiency of state-of-the-art photovoltaic cells," *Prog. Photovolt. Res. Appl.*, vol. 20, no. 4, pp. 472–476, 2012.

[13] J. Zhao, A. Wang, M. A. Green, and F. Ferrazza, "19.8% efficient 'honeycomb' textured multicrystalline and 24.4% monocrystalline silicon solar cells," *Appl. Phys. Lett.*, vol. 73, no. 14, pp. 1991–1993, Oct. 1998.

[14] I. Vurgaftman, J. R. Meyer, and L. R. Ram-Mohan, "Band parameters for III–V compound semiconductors and their alloys," *J. Appl. Phys.*, vol. 89, no. 11, pp. 5815–5875, Jun. 2001.

[15] "Alta Devices: Next Gen PV Challenges Status Quo : Greentech Media." [Online]. Available: http://www.greentechmedia.com/articles/read/stealthy-alta-devices-next-gen-pv-challenging-the-status-quo/. [Accessed: 27-Aug-2012].

[16] M. A. Green, K. Emery, Y. Hishikawa, W. Warta, and E. D. Dunlop, "Solar cell efficiency tables (version 41)," *Prog. Photovolt. Res. Appl.*, vol. 21, no. 1, pp. 1–11, 2013.

[17] J. F. Geisz, A. Duda, R. M. France, D. J. Friedman, I. Garcia, W. J. Olavarria, J. M. Olson, M. A. Steiner, J. S. Ward, and M. Young, "Optimization of 3-junction inverted metamorphic solar cells for high-temperature and high-concentration operation,"," presented at the CPV8, Toledo, Spain, Toledo, Spain, 2012.

[18] D. Aiken, E. Dons, N. Miller, F. Newman, P. Patel, and P. Sharps, "Commercial concentrator cell results and record IMM solar cell efficiency," presented at the CPV8, Toledo, Spain, Toledo, Spain, 2012.

[19] S. Wojtczuk, P. Chiu, X. Zhang, D. Pulver, C. Harris, and B. Siskavich, "42% 500X Bi-Facial Growth Concentrator Cells," *AIP Conf. Proc.*, vol. 1407, no. 1, pp. 9–12, Dec. 2011.

[20] R. R. King, A. Boca, W. Hong, X.-Q. Liu, D. Bhusari, D. Larrabee, K. M. Edmondson, D. C. Law, C. M. Fetzer, S. Mesropian, and N. H. Karam, "Band-Gap-Engineered Architectures for High-Efficiency Multijunction Concentrator Solar Cells," *Present. 24th Eur. Photovolt. Sol. Energy Conf. Exhib. Hambg. Ger. 21–25 Sept. 2009*.

[21] W. Guter, J. Schone, S. P. Philipps, M. Steiner, G. Siefer, A. Wekkeli, E. Welser, E. Oliva, A. W. Bett, and F. Dimroth, "Current-matched triple-junction solar cell reaching 41.1% conversion efficiency under concentrated sunlight," *Appl. Phys. Lett.*, vol. 94, no. 22, pp. 223504–3, Jun. 2009.

[22] C. Algora, E. Ortiz, I. Rey-Stolle, V. Diaz, R. Pena, V. M. Andreev, V. P. Khvostikov, and V. D. Rumyantsev, "A GaAs solar cell with an efficiency of 26.2% at 1000 suns and 25.0% at 2000 suns," *IEEE Trans. Electron Devices*, vol. 48, no. 5, pp. 840–844, May 2001.

[23] K. Ghosal, D. Lilly, J. Gabriel, S. Seel, E. Menard, S. Burroughs, R. Daniel, S. Lowe, and C. Kudija, "Performance of a micro-cell based transfer printed HCPV system in the South Eastern US," *AIP Conf. Proc.*, vol. 1477, no. 1, pp. 327–330, Oct. 2012.

[24] S. Kurtz, "Opportunities and Challenges for development of a mature Concentraing Photovoltaic power industry," NREL, Jun. 2012.

[25] K. Tanabe, A. Fontcuberta i Morral, H. A. Atwater, D. J. Aiken, and M. W. Wanlass, "Direct-bonded GaAs/InGaAs tandem solar cell," *Appl. Phys. Lett.*, vol. 89, no. 10, pp. 102106–3, 2006.

[26] L. Zhao, G. Flamand, Y. Mols, J. Van der Heide, and J. Poortmans, "Novel Mechanically Stacked Multi-Junction Solar Cells Applying Ultra-Thin III-V Cells and Wafer Based Germanium Cell," 2010, pp. 1123–1128.

Chapter 2

High-Efficiency Multi-Junction Solar Cells

2.1 Introduction

A review of the state of art in high-efficiency multi-junction solar cells is presented in this chapter. It starts by reviewing strategies to improve upon the performance of industry standard GaAs based triple-junction solar cells which centre around improving the current-matching between cells through the integration of better bandgap combinations. The chapter continues by providing an overview of mechanically stacked solar cells which can eliminate the current matching constraint by providing parallel connection to sub-cells. The characteristics of single-junction Ge, GaSb, InGaAs(P) and Si solar cells which can be used to provide narrow bandgap bottom cells under GaAs based top cells are discussed. While the potential performance of mechanically stacked solar cells is superior to monolithic cells, the challenges preventing this improvement being realised are outlined with particular emphasis on the resistive and optical challenges presented. Finally attempts to provide novel bandgap combinations for triple-junction solar cells by moving to solar cells based on lattice constants equal or close to InP are reviewed.

Throughout this chapter the thermodynamic limiting efficiency of multi-bandgap solar cells is presented. These efficiencies are found using the 'Detailed Balance Limit of Efficiency Method' first presented by Shockley and Queisser [1]. The simulation procedure calculates the efficiency of a multi-bandgap cell arrangement by considering:

- the current generated in each junction found by integrating over the solar spectrum and assuming all absorbed carriers create an electron-hole pair
- Radiative recombination as the only loss mechanism
- Maximum power is computed by considering the voltage-current dependency with current matching considered between junctions where required

i.e. solar cells are assumed ideal with no resistive, thermal or optical losses which are highly dependent on cell structure and design. EtaOpt [2] is a free software program available from the

Fraunhofer Institute which uses the detail balance limit of efficiency method to compare the potential power output of bandgap arrangements in single or multi-junction solar cells. An outline of the simulation procedure from [2] is given in Appendix B.

The chapter begins by reviewing the state of the art monolithic triple-junction solar cells comprising GaInP and GaAs top and middle junctions respectively. Strategies for improving the current matching with the bottom junction are presented. Alternative mechanically stacked bottom cells are then reviewed namely GaSb, InGaAs, Si and Ge cells. The resistive and optical constraints presented by mechanically stacking are reviewed. Finally recent work on InGaAlAs based triple-junction cells is reviewed. These cells aim to improve the current matching in series connected triple junction cells by considering alternative lattice constants.

2.2 GaAs based multi-junction solar cells

Current production multi-junction solar cells for terrestrial concentrating photovoltaic (CPV) systems comprise the mature GaInP/Ga(In)As/Ge lattice matched material system. The ultimate efficiency of this configuration is restricted by the non optimal 1.9, 1.39, 0.67 eV bandgap combination [3] and the current matching requirement for monolithically interconnected junctions. The large current produced in the low-bandgap Ge junction is wasted as the device current is restricted to the lowest produced by any of the junctions in the series connected device while the narrow bandgap material contributes a low voltage. Figure 2.1 outlines the detailed balance limit of efficiency of a monolithic or mechanically stacked GaInP/GaAs/narrow-bandgap triple junction solar cell as a function of the bottom cell bandgap. In the monolithic configuration, a bottom cell bandgap of 1.04 eV produces the largest voltage that also matches the current produced by the top two junctions leading to a peak efficiency of 53.6%. If the bottom junction is individually contacted, as in a stacked formation, a higher efficiency can be achieved as the photocurrent response increases with decreasing bandgap. A peak of 58.6% is achieved with a bandgap of 0.7 eV as the voltage of narrower *Eg* materials becomes too low. The troughs in efficiency are due to ozone and moisture absorption in the solar spectrum which significantly reduces the incident intensity at certain wavelengths. The photovoltaic performance of GaAs based triple-junction solar cells can be improved by the monolithic integration of a ~ 1eV bottom junction or the integration of a separately contacted bottom cell.

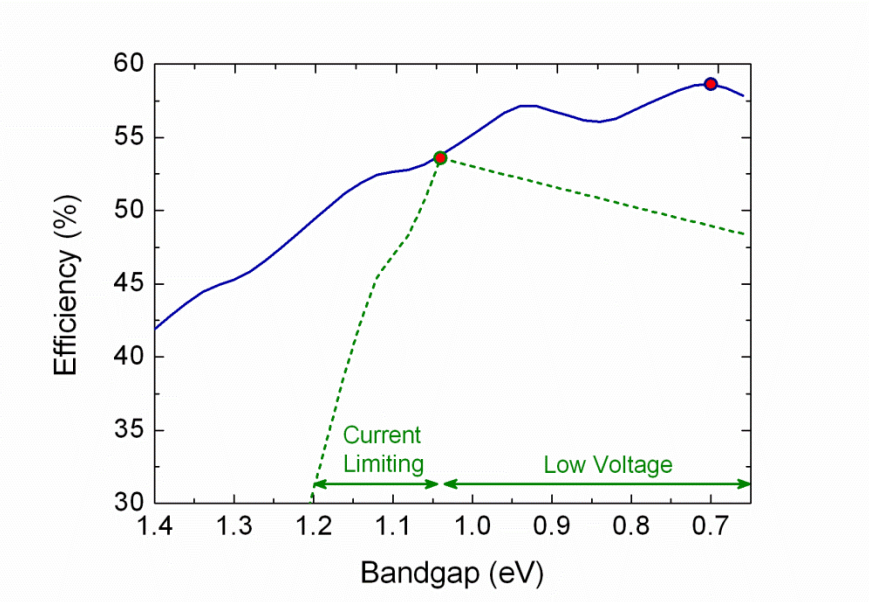


Figure 2.1: Detailed balance efficiency for the AM1.5d spectrum under 500 Suns concentration of a triple-junction solar cell with a GaInP/GaAs (1.9/1.41 eV) top cell and a series connected bottom cell (dashed line) or independently contacted bottom cell (solid line) as a function of the bottom cell *Eg*. The junction temperature for the model was 300 K. The peak efficiency for each cell type is highlighted as a red dot.

The current state of the art triple-junction solar cell for concentrating photovoltaics is produced by Solar Junction and incorporates a ~ 1 eV bottom junction using dilute nitride III-V materials [4]. The dilute nitride GaInNAs material system can be lattice matched to GaAs by adding In and N to GaAs at a ratio of 2.7 to 1 allowing access to lattice matched bandgaps in the 1.4 – 0.7 range [4] (Figure 2.2). The only details of this cell design are given in the solar cell efficiency tables but list a GaInP/GaAs/GaInNAs triple-junction material system with an efficiency of 44% under concentration as measured at the NREL test facility [5].

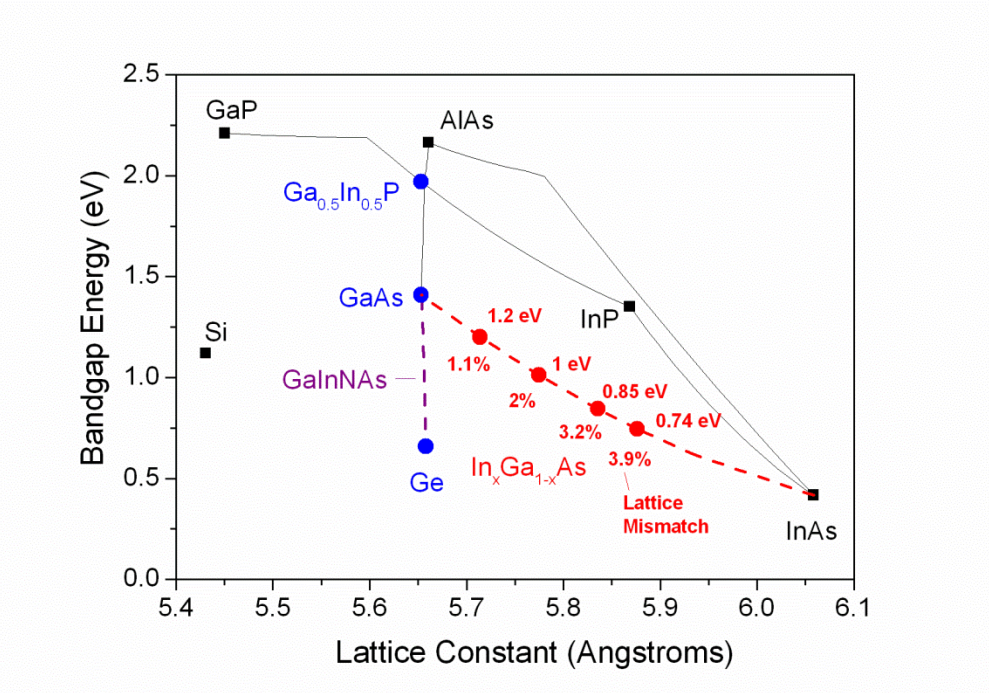


Figure 2.2: Bandgap (300 K) versus lattice constant for a range of semiconductor materials and alloys. The lattice matched GaInP/GaAs/Ge triple junction cell is highlighted with blue dots. The bandgap and % lattice mismatch to GaAs for $In_xGa_{1-x}As$ are shown as well as the range of bandgaps available for the GaInNAs material system.

Metamorphic (MM) compositionally graded buffer layers are grown in order to combine lattice-mismatched junction materials in monolithic multi-junction solar cells. Threading and misfit dislocations caused by strain must be contained to these graded layers in order to reduce the density of defects in the junction region of devices. Dislocations will cause a drop in efficiency due to increased nonradiative recombination [6]. Spire have developed a bi-facial growth process to integrate lattice-matched GaInP and GaAs materials with lattice-mismatched $In_{0.35}Ga_{0.65}As$ [7]. In this growth sequence the GaInP and GaAs top and middle junctions are grown lattice matched to a GaAs substrate; An $In_{0.35}Ga_{0.65}As$ bottom junction is grown by flipping the wafer post growth of the top two junctions and growing on the back side using step graded $In_yGa_{1-y}As$ layers. As absorption in the GaAs substrate will reduce the photoresponse of the InGaAs cell; N-type substrates with low doping are used as they are known to suffer less free carrier absorption losses than other doped GaAs substrates [8]. The bi-facial growth method for triple-junction solar cells has produced photovoltaic conversion efficiencies of 42.3% under 343 suns, however, the commercial potential of this technology is questionable due to the cost of growing the relatively thick (5.8 μm) layers required for the InGaAs cell. While this system has achieved high

performance the potential of an separately contacted $In_xGa_{1-x}As$ bottom junction with a lower bandgap remains greater and forms the focus of this thesis.

Current matching can also be achieved in GaAs based triple-junction cells on Ge substrates by increasing the In content of the top two junctions thus reducing their bandgaps. Guter *et al.* grew step-graded $Ga_{1-y}In_yAs$ buffer layers on active Ge substrates altering the In content from 0% (lattice matched to Ge) to 17%. A 65% In content $Ga_{1-x}In_xP$ top junction is grown as the top cell resulting in 1.1% lattice constant mismatch between the top two cells and the host substrate producing a triple-junction bandgap combination of 1.67, 1.18 and 0.67 eV. The generation of defects is contained in the 1400 nm thick graded-structure leading to a high performance device where the bandgap combination produces a high 16.4 mA/cm^2 photocurrent density under one-sun illumination and has a photovoltaic conversion efficiency of 41.1% under 454 suns [3].

2.3 Heterogeneous integration of solar cells through mechanical stacking

The primary difficulties in advancing the performance of monolithic multi junction solar cells beyond that of an optimised triple junction device are providing an optically transparent, low resistance and reliable ohmic contact between the required lattice mismatched alloys for optimum spectrum splitting in a cost-effective way. Mechanically stacked solar cells offer alternative routes to multi junction solar cells that can reduce these constraints through additional terminals to the cells which make up the stack. Typically a GaAs solar cell or the well established lattice and current matched GaInP/GaAs dual junction solar cell is grown on a GaAs substrate and stacked above a separately fabricated lower bandgap cell. An additional terminal to the low bandgap bottom junction removes the constraint of current matching as the extra current is not wasted in series connection. This fabrication route removes the need for step-graded buffer layers or an ohmic contact between the middle and bottom junctions.

Given the constraints of monolithically integrating cells, mechanical stacks have received renewed interest from the PV community. Currently the state of the art multi-junction solar cell is a 4J series connected GaInP/GaAs-InGaAsP/InGaAs solar cell [9]. The cell is fabricated through direct bonding of dual-junction cells on GaAs and InP substrates with a peak efficiency of 44.7% at Suns.

2.3.1 Materials

Figure 2.1 shows that 0.7 eV is the optimum bandgap, for highest conversion efficiency, for the bottom cell stacked under a dual junction GaInP/GaAs top cell. This bandgap corresponds closely to a number of candidate materials, namely Ge, GaSb and $Ga_{0.47}In_{0.53}As$ which have corresponding bandgaps of 0.67 eV, 0.72 eV and 0.74 eV at 300 K, respectively. A local maximum is seen for the bottom cell at 0.95 eV which can be achieved with $Ga_{0.25}In_{0.75}As_{0.54}P_{0.46}$ and is close to the bandgap of Si (1.1 eV) solar cells which have also been used owing more to their low cost compared to compound semiconductor devices.

Figure 2.3 is a graph of the open-circuit voltages achieved by the state of the art narrow bandgap cells stacked under GaAs or GaInP/GaAs top cells under 1 sun illumination. To compare the performance of each material the bandgap-voltage offset at open-circuit voltage (W_{oc}) is also shown [10]. As the open-circuit voltage of a solar cell is directly linked to the materials bandgap; W_{oc} offsets are a useful comparison of the experimental and theoretical performance of single junction cells and are calculated as shown in Equation 2.1.

$$W_{oc}\,(V) = \frac{E_g}{q} - V_{oc} \qquad (2.1)$$

While InGaAs and InGaAsP cells have been stacked with W_{oc} offsets of < 0.4 V, the offsets for Ge and Si devices are greater, showing there is potential for improvement in solar cells made from Group IV materials.

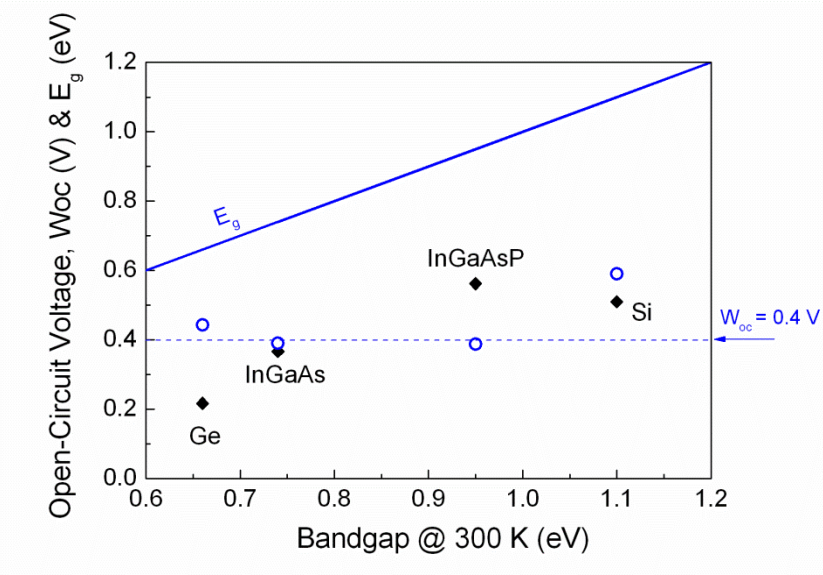


Figure 2.3: The open-circuit voltage, measured under 1 Sun AM1.5G conditions, of the state of the art single-junction narrow bandgap cells stacked under GaAs or GaInP/GaAs top cells (black diamonds). Also shown is the Bandgap-Voltage offset (W_{oc}) of the cells (blue open circles) and the bandgap of the material (solid line). Note a measured value for a GaSb cell was unavailable [11]–[14].

Figure 2.4 is a plot of the short-circuit current densities of the state of the art narrow bandgap cells stacked under GaInP/GaAs or GaAs solar cells under 1 sun illumination. Also shown is the expected photocurrent density of an ideal solar cell with 100% EQE for photons with energy greater than the material bandgap, calculated for the AM1.5G spectrum cut-off at 880 nm (i.e. the spectrum transmitted by a GaAs based solar cell). The offsets between the state of the art and the ideal are given as a percentage of experimentally measured to ideal short-circuit current density and show the photocurrent offset increases with decreasing bandgap except for the state of the art Si device. A probable cause of this is the broader spectrum of photons the top cell must be transparent to as the bandgap is decreased. Reflection at the front surface of the GaAs based top cell and the interface between the top cell and bottom cell contribute a significant loss to the measured photocurrent density. The reduction of these reflection losses is more easily achieved over a narrower wavelength range, e.g. 880 - 1305 nm (InGaAsP), than for a broader 880 – 1860 nm range (Ge).

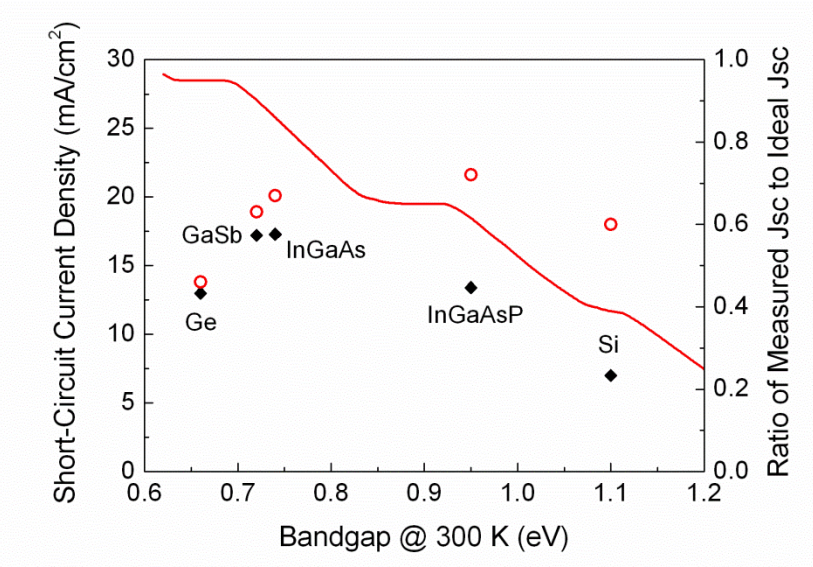


Figure 2.4: The short-circuit current density, measured under 1 Sun AM1.5G conditions, of the state of the art single-junction narrow bandgap cells stacked under GaAs or GaInP/GaAs top cells (diamonds). Also shown is the photocurrent density of an ideal solar cell with 100% EQE as a function of bandgap (solid-line) for the AM1.5G spectrum for $\lambda > 880$ nm. The ratio of the measured short-circuit current density to the ideal photocurrent density is also given (open circles) [8], [11]–[14].

The following sections discuss the reasons for the bandgap-voltage offset and the < 1 ratio of actual to theoretical short-circuit current density for narrow bandgap bottom cells fabricated from Ge, GaSb, InGaAs(P) and Si and stacked under GaAs based top cells.

2.3.1.1 Ge

While the bandgap of Ge is close to optimum for sub-cell use under a GaAs device the performance of such cells is constrained by the low voltages achieved. Front surface passivation is critical as dangling bonds lead to high surface recombination, *S*, and a drop in the voltage produced by devices [15], [16]. The problem is further complicated by the need for thin emitter layers as most photons are absorbed near the cell surface leaving the junction close to this recombination zone. In monolithic triple junction solar cells GaAs passivates the n-Ge surface but additional techniques are required for stand-alone Ge cells. IMEC have developed a PECVD amorphous-Si layer deposition process which can reduce S to < 20 cm/s on lowly doped ($2x10^{14}$ cm^{-3}) p-Ge wafers [17], [18]. The combination of an a-Si layer and metal contact formation on the front surface is challenging due to surface cleaning requirements for high passivation which are

restricted by the metal used and the lack of an a-Si wet or dry etch with high selectivity on Ge. A diffused contact is realised where metal is patterned and deposited on the a-Si layer and a heat treatment process used to diffuse this metal through the layer to contact Ge [17]. This innovative method allows surface cleaning using methods suitable for good passivation but does not require a-Si layer patterning. This has led to Ge cells with an efficiency of 7.8% with an open-circuit voltage of 268.7 mV and a Fill Factor of 62.4% under 1-Sun conditions (AM11.5G). Such Ge cells have been stacked with a thin GaAs top cell using a Dow Corning epoxy (DC 93-500) to form a mechanical stack with a 1-sun (AM1.5G) conversion efficiency of 25.1% where the Ge cell contributed 1.9% [14].

2.3.1.2 GaSb

The use of GaSb infrared converters for mechanical stacks and thermophotovoltaics has been pioneered by the IOFFE institute. Their work concentrates on the use of relatively low-cost liquid phase epitaxy and Zn diffusion to produce 0.72 eV cells [19]. An n-GaSb layer is grown epitaxially on a heavily doped n+ substrate in order to provide a high quality GaSb crystalline material into which a p-layer is formed through Zn diffusion. The use of a high quality crystalline epitaxial n-type layer increases the carrier diffusion length in the n-GaSb material and improves the IR response as the long wavelengths absorbed deep in the device are collected making them suitable for stacking under GaAs top cells. An efficiency of 6.2% at 290 suns was achieved for a GaSb cell under a GaInP/GaAs top cell giving a maximum stack efficiency of 35% under 50 suns concentration [8]. The Fraunhofer institute have also fabricated III-V solar cells using liquid phase epitaxy (LPE). Their LPE GaSb cell, initially developed as an IR converter for thermophotovoltaics [20], was combined with a MOCVD GaInP/GaAs solar cell to produce a stack with an efficiency of 33.5% at 308 suns [21]. A CPV module incorporating GaAs and GaSb LPE solar cells was fabricated with an efficiency of 21.3% [22].

2.3.1.3 InGaAs(P)

InGaAs (53% In) grown lattice matched to InP has a bandgap of 0.74 eV at 300 K. Sumitomo Electronic Industries have developed an MOVPE growth process to prepare InGaAs solar cells. The cell structure consists of a n-on-p configuration owing to the larger minority carrier diffusion lengths in p-InGaAs [23]. The longer lifetime for electrons in the p-type base layer leads to a low reverse saturation current and higher open-circuit voltages but at the expense of short wavelength

response owing to the reduced lifetime in the n-type emitter. Cell performance was maintained over large areas with a 5 x 5 cm^2 InGaAs cell stacked under a GaAs cell to produce a tandem cell efficiency 28.9% under 1-sun AM1.5G conditions [11]. The IOFFE institute have applied their liquid phase epitaxy technology to lattice-matched InGaAs cells on InP [24]. The cell structure is grown inverted on an InP substrate (i.e. the emitter layer is grown before the base layer), and the GaAs-InGaAs stack formed with the InP substrate between the InGaAs epitaxy structure and the overlying GaAs stacked solar cell. This allows the n-type InP substrate to act as an extremely thick lateral conduction layer and removes the need for grid lines on the front of the InGaAs device. The reduced shading area increases the photo response with an EQE of 97.5% achieved at 1.2 μm. The devices achieved a photovoltaic conversion efficiency of 7.4 – 7.35% between 500 – 1000 suns (wavelengths < 880 nm were absorbed by the InP substrate) showing the potential benefit of narrow bandgap InGaAs solar cells [25]. This thesis will utilise a narrow bandgap InGaAs cell to form a mechanically stacked solar cell. While the bandgap-voltage offset [10] of the state of the art device is low, the photocurrent produced allows room for improvement. Strategies to reduce optical losses due to reflection or parasitic absorption are presented as well as a solar cell structure which is designed for near-infrared absorption.

Yamada *et al*. have grown single junction $Ga_{0.25}In_{0.75}As_{0.54}P_{0.46}$ (0.95 eV) solar cells lattice matched to InP for use as the bottom junction in a stacked GaAs-InGaAsP cell [12]. A stacked cell performance of 31.1% under 1-sun AM1.5G conditions for 1 cm^2 cells was achieved through improved growth conditions for the InGaAsP cell which reduced defects at InGaAsP-InP hetero-interfaces reducing surface recombination and improving short wavelength response.

Lattice-matched monolithic dual-junction InGaAsP-InGaAs (0.95 and 0.74 eV at 300 K) solar cells have been developed as low bandgap series connected cells for use in multi-junction solar cells [26]. An efficiency of 7.9% has been achieved for 1-sun conditions under a GaAs filter [27]. Steiner *et al*. used three terminals to remove the current matching condition allowing thicker junctions to be grown for improved photo response and less sensitivity to spectral variations. The cell, designed for use in a spectrum splitting module [28], achieved 10.2% under 1-sun conditions and 11.9% under 45 suns under an 871 nm filter [29].

2.3.1.4 Silicon

The 1.1 eV bandgap of Si at 300 K results in a low photocurrent when stacked below GaAs based devices but because of their availability and low cost Si devices are used in mechanical stacks to provide a cost-effective efficiency boost. Si solar cells have typically been combined in stacks by using the back point contact Si cell thus allowing epoxy bonding [30]. A more interesting arrangement involves the use of a Si solar cell as a cost-effective carrier for an epitaxial lift off III-V solar cell [31]. The 100% difference in thermal expansion co-efficient between GaAs and Si provides a constraint to use in high concentration systems as the stress between the layers at elevated temperatures may lead to cracking of the thin GaAs cells.

The monolithic integration of III-V solar cells with Si is of interest as its 1.1 eV bandgap is close to the desired 1 eV value for the bottom junction in triple junction monolithic multi-junction solar cells. The Fraunhofer Institute have bonded a GaInP/GaAs dual junction solar cell to a Si solar cell [32]. An etch stop/bonding interface layer is used to selectively remove the GaAs substrate and the GaInP/GaAs cell bonded to the 1.1 eV Si solar cell at room temperature thus avoiding stresses caused by the 100% difference in thermal expansion coefficients. A conversion efficiency of 20.5% under 1 sun illumination was achieved where cell performance was limited by the low photocurrent produced by the Si junction which should be overcome by thinning the top cells. The resistance of the interface lead the performance under concentration to peak at 71 sun illumination (efficiency = 23.6%).

2.4 Mechanical Stacking

The stacking methods used to form multi-junction solar cells from individual cells need to overcome the constraints of ohmic resistance, optical losses (through interface reflection, increased metal shading, substrate absorption and a lack of broadband anti-reflection coatings), heat sinking, thermal expansion and cost.

2.4.1 Ohmic resistance

The resistance of multi-junction solar cells is of critical importance when used in concentrating systems owing to the high currents of up to 7 A/cm^2 produced as power losses scale with module resistance ($P = RI^2$). For series connected devices the main source of power loss is the front

contact where a balance has to be found between percentage shading and series resistance [33]. In mechanically stacked solar cells, the packaging of individual devices in a stack introduces additional resistive elements which may contribute a more significant power loss than the front contact. These include lateral conduction layers used to provide both contacts on one side of the device, metal holders or in the case of wafer bonding, the direct bond interface. Figure 2.5 is a simulated iso-efficiency plot of a GaAs single junction solar cell as a function of concentration (suns) and internal series resistance (ohms). For high concentration operation (> 100 suns) a series resistance of less than 0.01 ohms must be achieved in order to not significantly degrade device performance.

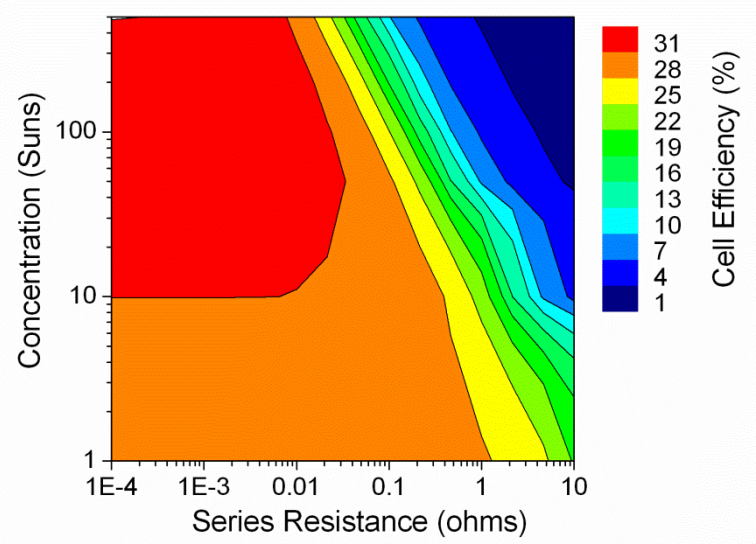


Figure 2.5: Simulated photovoltaic conversion efficiency of a single-junction 1 cm^2 GaAs solar cell under concentration as a function of series resistance. The simulations were carried out using PC1D [34] for a 250 nm p-GaAs emitter ($2x10^{18}$ cm^{-3}) and 3500 nm n-GaAs base ($3x10^{17}$ cm^{-3}) layers.

Metal Holders

Initial approaches to stacking low bandgap subcells underneath GaAs based solar cells used metal holders which held the cells in proximity, as in Figure 2.6 (a). Typically Cu structures acted as both electrical contacts and heat sinks. The doped substrates of the solar cells act as lateral conduction layers which are of adequate thickness to contribute < 0.01 Ω to the series resistance of the cells. Andreev *et al*. combined a GaAs top cell, which is highly transparent to near infrared radiation (400 um thick, n-type ($1x10^{17}$ cm^{-3})), with their inverted structure $In_{0.53}Ga_{0.47}As$ bottom cell using a copper holder [24]. The holder contacts the edge of the back of the GaAs device on

one side and the edge of the InP substrate (which faces the sun) on the other. While these systems are bulky they are to date the most favourable route for producing mechanical stacks for operation under concentration. Bett *et al*. used a Cu holder to combine GaInP/GaAs-GaSb solar cells in a system whose performance peaked at 308 suns with an efficiency of 33.5% [21]. The drawback of these systems is the significant reflection loss at the air gap interface between the cells and absorption in the top cell substrate. Removing heat from the top cell is also difficult as the Cu heat sink is only in contact with the edge of the back of the cell rather than the whole back surface leaving a narrow path for heat conduction.

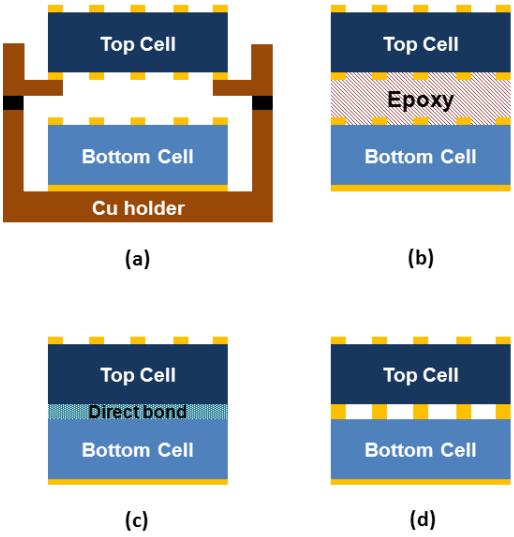


Figure 2.6: Mechanical Stacking strategies: (a) Metal holders (b) Epoxy bonding of solar sells (c) Direct semiconductor bonded solar cells (d) Grid metal bonding.

Epoxy Bonding

Combining solar cells through epoxy bonding (Figure 2.6 (b)) leads to increased packaging resistance owing to the complex contacting schemes required for the cells. Polyimide dispersed with Indium Tin Oxide (ITO) particles has been used to bond Si and amorphous Si cells [35]. ITO particles with an average diameter of 20 μm were mixed in Polyimide and spin-coated onto the cells where the ratio of the thin-film area occupied by particles was 10%. Post bonding, the connecting resistivity between the cells was 2.3 Ωcm^2 with the optical interface being 80% transparent in the 500 to 1000 nm wavelength range. The connecting resistivity of the 20 μm

conducting adhesive is too high for concentration operation as it would contribute an internal series resistance of 0.43 Ω to a 1 cm^2 cell. When electrically insulating epoxies are used to bond cells, contacts are typically provided on one surface of each cell. This requires the growth of lateral conduction layers or using the substrates for current spreading which leads to optical losses due to free-carrier absorption. Alternatively, metal fingers can be patterned on the back side of the GaAs device [36]. While this maintains a low series resistance the increased number of lithography steps increases fabrication costs.

Direct Semiconductor Bonding

Direct semiconductor to semiconductor bonding (Figure 2.6 (c)) produces monolithic series connected devices where the key challenges are the production of large area void free bonds with suitably low ohmic resistance and high optical transparency. Tanabe *et al*. first demonstrated a direct bonded GaAs-InGaAs tandem solar cell where the bottom cell was grown lattice-matched to InP while the upper cell is grown inverted and lattice-matched to a GaAs substrate with this substrate removed post bonding [37]. The device had a low series resistance of 0.12 Ωcm^2 at the interface with a 10% absolute decrease in the spectral response of the bottom InGaAs cell. The open-circuit voltage of both cells was maintained post bonding showing the process did not significantly damage the crystal layers nor were there a high number of defects at the interface. While the resistance of the bonded interface is low enough for 1-sun operation it is an order of magnitude too large for concentrating photovoltaics. The large ohmic resistance at the bond interface has led further research into direct bonded devices to focus on large area solar cells for space applications which operate under 1-sun conditions (AM0) where four and five junction solar cells have been produced [38].

Grid Bonding

To reduce the resistance of bonding interfaces intermediary bonding layers are under investigation. Aiken *et al*. realised Au-Ge eutectic bonds of perpendicularly orientated grids with specific resistivity of 0.014 Ωcm^{-2} [39]. The air-cavity created by this bond type results in high reflection losses at the interface which Lin *et al.* overcome by using a GaInP or SiO_2 filler layer [40]. 1 μm of GaInP is grown as the final layer of an inverted GaInP/GaAs solar cell. Photolithography and a selective wet etch are used to create a grid pattern in the optical coupling layer. Metal contacts are deposited on the GaAs contact layer in these etched regions. The grid contacts deposited on the back of the GaAs device are aligned and eutectic bonded to the grid

contacts on the top of the InP based bottom cell as outlined in Figure 2.6 (d). While the bonded grid-metal provides the mechanical strength between cells the GaInP layer is grown to the same height as the expected bonded metal thickness thus providing complete optical coupling post bonding as GaInP provides excellent index-matching between GaAs and InGaAs. The most complex device produced has been a GaInP/GaAs tandem cell bonded to an InGaAs bottom cell with an open circuit voltage of 2.7 V demonstrating sufficient electrical coupling although this is less than the open circuit voltages of the individual cells pre-bonding indicating some damage occurred. Boca *et al.* used carbon nanotube composite thin films to provide the optical, electrical and mechanical coupling between InP and GaAs based solar cells [41]. The minimal contact resistance between the thin film and a III-V material layer was too high for concentrated sunlight applications at 0.21 Ωcm^2. Whole wafer bonding was completed on 3" GaAs wafers and typically yielded bond-pairs with 60% of the wafer area well bonded.

2.4.2 Optical losses

Optical losses contribute a significant loss in mechanically stacked solar cells as the wavelength range over which the system must be designed for reduced reflection and parasitic absorption is broad. For optimum ~0.7 eV bandgap bottom cells the relevant wavelength range extends from 300 – 1770 nm. This section outlines strategies for improving the optical performance of stacked solar cells with particular emphasis on the photocurrent response of the narrow bandgap bottom cell.

Substrate absorption

A significant source of optical loss in GaAs based mechanically stacked solar cells is free carrier absorption in substrates since a portion of the photons with wavelengths greater than the bandgap of GaAs are not transmitted to the bottom cell. Low-doped n-type substrates are commonly used for GaAs based stacked solar cells as their absorption co-efficients are less than other doped GaAs substrates. Hence the p-on-n structure is typically used in the GaAs cell despite the penalty of reduced lifetime in the emitter layer. The percentage transmission of near infrared photons (880 – 1680 nm) by a GaAs substrate as a function of thickness and n-type doping is shown in Figure 2.7. The lowest doped $1x10^{17}$ cm^{-3} substrate has high transmission of 96% for a substrate thickness of 650 μm. Semi-insulating GaAs substrates offer an alternative high transparency substrates as the nominally un-doped wafers suffer negligible free carrier absorption.

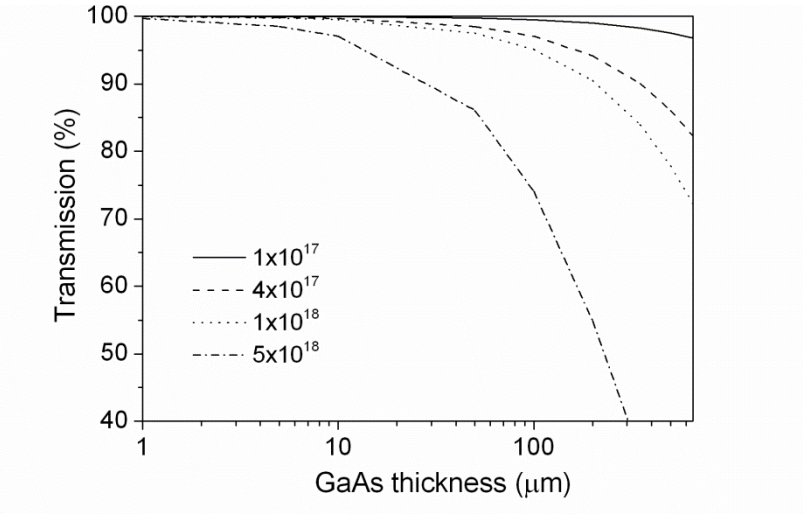


Figure 2.7: Weighted transmission of 880 – 1700 nm photons through n-GaAs as a function of doping level and thickness as calculated using data in [42].

The typical doping of substrates used for a GaAs cell is in the $5x10^{17}$ cm^{-3} range. A 350 μm substrate of this doping will absorb 10% of incoming photons, incurring a significant penalty on the photocurrent of the narrow bandgap cell. Substrates with a higher doping level can be used to reduce resistance in the mechanical stack. If a $1x10^{18}$ cm^{-3} substrate is used, however, the substrate needs to be thinned to 100 μm to achieve the same absorption level as a 650 μm and $1.3x10^{17}$ cm^{-3} substrate showing the balance required between resistance and absorption losses.

In order to eliminate substrate absorption the epitaxial solar cell structure may be removed from the GaAs substrate post MOVPE growth. The epitaxial lift-off (ELO) technique [44] for GaAs based solar cells was developed as a cost saving process which allows re-growth on the host substrate and a saving on cell cost. An AlAs release layer is grown as the first layer before a GaAs solar cell structure. The high Al content layer is selectively etched in hydrofluoric acid to release the rest of the epitaxial structure from the substrate [43]. The III-V device is typically bonded to a handle substrate such as glass or a Si wafer or a heat sink for mechanical support. The III-V device may also be bonded to a lower bandgap solar cell to create a mechanically stacked solar cell with low parasitic absorption losses [14], [31].

Interface reflection

The stacking of solar cells introduces a refractive index step between the semiconductor devices. The magnitude of reflection at this optical interface is a function of the refractive index of the

material between the stacked cells. The reflection must be reduced over a broad range of wavelengths from 880 nm to the bandgap of the bottom cell. Figure 2.8 shows the expected transmission of a GaAs-Interface-InGaAs as a function of interface refractive index, considering simple Snell's law reflection only at each interface, as averaged over the 890 – 1680 nm range.

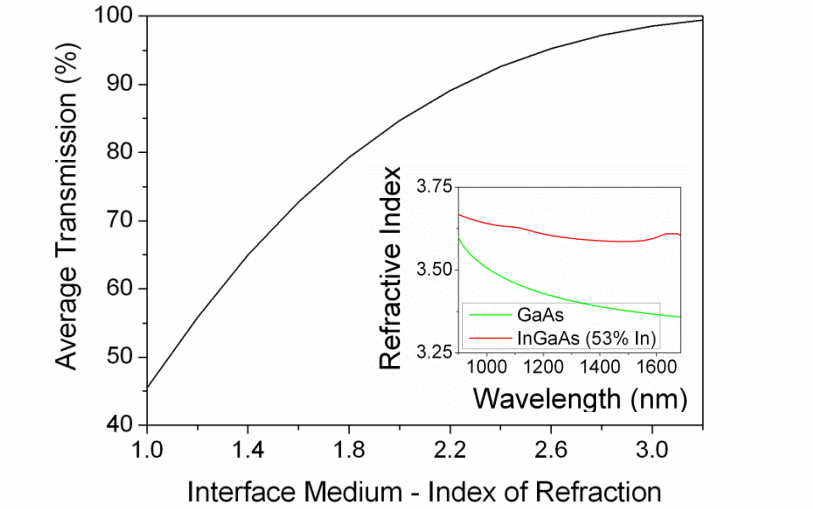


Figure 2.8: The average reflection of wavelengths between 890-1680 nm at a GaAs-InGaAs interface as a function of the interface index of refraction modelled using Snell's law. The measured refractive indices (from an ellipsometric database) of GaAs and $In_{0.53}Ga_{0.47}As$ in this region are presented in the inset figure.

45% transmission is seen for an air gap (n = 1) interface owing to the significant index step between the semiconductors and air which causes a reflection loss of ~ 33% at each interface. The typical reduction strategy used involves grading the index between the semiconductor and air using anti-reflection coatings optimised for near infra-red radiation transmitted through GaAs and absorbed by the bottom cell [11]. To remove the air interface a filler medium with a higher refractive index, such as an epoxy, is used which may also bond the cells. Adhesives which have been proposed or used for bonding of solar cells include Dow Corning's 93-500 Space-Grade silicone encapsulant [14], benzocyclobutene (BCB) [44] and bolyimide [35] whose material properties are shown in Table 2.1 as well as those of polydimethylsiloxane (PDMS) which is investigated as part of this thesis.

Table 2.1: Thermal and optical properties of the materials discussed for use in a bonded cell.

Material	Nominal refractive index (800 – 1650 nm)	Thermal conductivity (W/mK)	Linear Co-efficient of Thermal Expansion (ppm)
Dow Corning 93-500	1.41	0.146	3000
Polydimethlysiloxane	1.41	0.2	310
Benzocyclobutene	1.54	0.29	42
Polyimide	1.78	0.146	13
GaAs	3.4	55	5.73
$In_{0.53}Ga_{0.47}As$	3.6	5	5.66
InP	3.45	68	4.6

Bonding the cells with polyimide (n = 1.78) will reduce the reflection losses to 21% without any additional grading from an AR coating, while silicone based polymers such as DC93-500 and PDMS create an interface with a reflection loss of 35%. Direct semiconductor bonding leads to the highest transmission but at the expense of increased resistance in the cell [37]. This thesis focuses on the use of BCB as a high refractive index epoxy, in conjunction with dielectric anti-reflection coating layers, to reduce the reflection between the bonded cells while allowing the fabrication of low resistance contacts to the bottom cell.

Broadband anti-reflection coatings

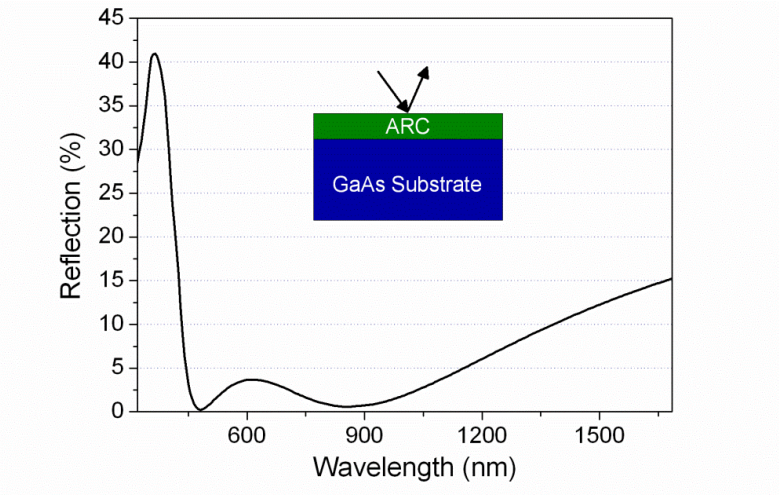


Figure 2.9: Simulated front surface reflection at normal incidence from a GaAs solar cell with a double-layer SiO_2/ZnS anti-reflection coating.

Broadband anti-reflection coatings are required for multi-junction solar cells as the terrestrial solar spectrum extends from the UV wavelength range to the near-infrared. Double-layer anti-reflection coatings (DLARC) such as ZnS/MgF are adequate for use in GaInP/GaAs/Ge multi-junction solar cells as the requirement to reduce reflection above 880 nm is reduced as the Ge junction produces an excess current which is wasted in the series connected device. A small (10 – 15%) reflection loss at wavelengths > 880 nm does not reduce the Ge cell current below the matched value of the top two junctions. Therefore they have become the standard in production cells. Figure 2.9 shows the modelled reflection from a ZnS/SiO_2 DLARC optimised for the front surface of a GaAs solar cell in a tandem stack. While reflection can be reduced to < 4% across the GaInP/GaAs absorption wavelengths (400 - 880 nm) the double layer system is limited in the spectrum over which reflection will be reduced. The photocurrent of any additional junctions, as with a narrow bandgap InGaAs cell, is reduced. Anti-reflection coating systems with more than two dielectric layers have been proposed [45] and are likely to become common in future multi-junction cell architectures. The most common strategy to improve the broad reflection characteristics of coatings is to vary the index of an applied coating in order to grade from that of the cell encapsulant (n ~ 1.4) to the semiconductor material, theoretically reducing reflection to zero across all wavelengths [46]. As conventional or dielectric materials with this required range of indices is not available the use of materials of varying porosity is being pursued [47]. As the index changes with porosity in these coatings various deposition methods are being developed [48]. It remains to be seen if these nanoscale systems can survive the packing and operation conditions of multi-junction solar cells.

2.4.3 Reduced optical losses through Spectrum Splitting

Spectrum splitting systems combine individual solar cells in a multi-junction combination by splitting the incident solar radiation into bandwidths and directing the relevant portion onto solar cells of relevant bandgaps. As outlined in Figure 2.10 optical elements such as dichroic mirrors or prisms are used to split the incoming radiation onto component sub-cells. Splitting the incoming radiation onto each component cell removes the reflection losses at the interface between stacked cells and absorption in the substrates. The first experimental multi-junction solar cell was an $Al_{0.24}Ga_{0.76}As$-Si spectrum splitting module which incorporated a dichroic filter [49].

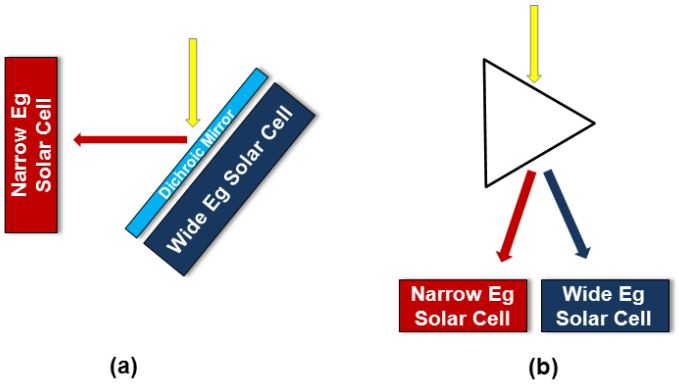


Figure 2.10: Spectrum splitting solar cell concepts (a) A dichroic mirror is used to reflect long wavelengths onto the narrow bandgap cell while higher energy photons are transmitted to the Wide *Eg* cell (b) A prism splits the relevant bandwidth range of photons onto each component sub-cell.

The Very High Solar Cell Efficiency (VHESC) program is a research consortium led by the University of Delaware which aims to integrate high performance solar cells and optics to achieve greater than 40% solar module efficiency. The group is looking to combine high bandgap (2.4 eV), GaInP/GaAs, Si and low bandgap (0.9 and 0.75 eV) solar cells in a spectrum splitting concentrating module [50] using dichroic mirrors. The provision of high reflectance dichroic mirrors is well understood but producing high transmittance over large bandwidths remains a challenge for PV systems which incorporate low bandgap cells. A module efficiency of 38.5% under 20 suns concentration using a dichroic mirror and GaInP/GaAs and GaInAsP/InGaAs solar cells has been achieved [51]. This performance compares very well to other CPV module efficiencies which normally lie in the 25-30% range for 500x systems although the higher concentration ratios put these systems in a different design space. Their measured cell efficiency includes optical losses due to packaging and concentration not typically given for state of the art multi-junction solar cells. While the promise of these systems remains high their optical performance must be proven. The predicted reflectance is complicated by the use of concentration optics as filters are typically designed for a 45^{o} angle of incidence. By their use in concentration systems there is always a divergence in the light angle incident on the filter and thus the transmission will vary across the filter which reduces system efficiency. If low loss dichroic mirrors can be produced reliably the cost of these systems may still be inhibitive due to the large number of semiconductor substrates required.

The development of well defined optical coatings has led to an increase in the complexity of dielectric layers that can be deposited for dichroic mirrors. Grob *et al*. designed a PV system incorporating a dichroic mirror which requires maximum transmission in the wavelength region of 850 – 1800 nm at an angle of incidence of 45°. The optimised optical design incorporates 220 alternating TiO_2 and SiO_2 layers, the thickness of which ranges from 1 to 400 nm in an irregular fashion highlighting the high tolerances required [52]. This mirror was combined with another filter design with high transmittance at wavelengths > 1100 nm in a GaInP/GaAs, Si and GaSb solar cell configuration to produce a measured cell efficiency of 34% under non-concentrated but collimated direct outdoor sunlight [53].

Khvostikov *et al*. are looking to combine their liquid phase epitaxy solar cells in a spectrum splitting system in order to reduce the cell cost component of the system [54]. They combine $Al_{0.3}Ga_{0.7}As$, GaAs and GaSb solar cells to produce a system with a module photovoltaic conversion efficiency of 24.3% under single sun illumination.

Spectrum Splitting modules are currently the highest performing photovoltaic technology incorporating independently contacted multi-junction solar cells as shown in Figure 2.11.

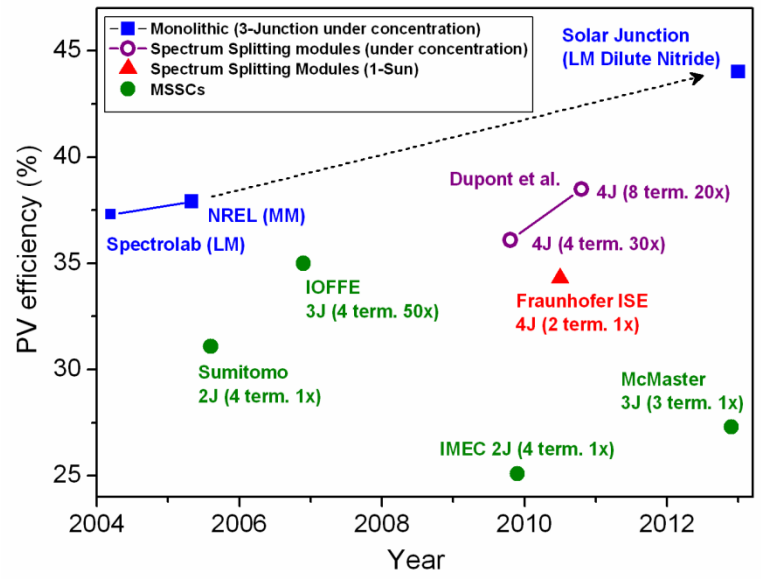


Figure 2.11: Selected results for the efficiency of multi-junction solar cells over the last decade. Additional references not in text: [55], [56].

2.5 Annual Energy Yield

While this chapter compares the simulated efficiency of solar cells under standard spectral conditions, which for a given number of junctions are typically higher for multi-junction cells which introduce additional cell terminals, an overlooked advantage of the additional terminals is reduced spectral sensitivity. As the time of day and year varies so does the solar spectrum incident on a solar cell. As the the current from a series-connected cell is limited to the lowest of any cell in the device, this varying spectrum significantly alters the efficiency of the cell and leads to a lower annual energy output as compared to a cell with individual terminals where the current is not constrained. Mols et al. simulated the total energy output of a triple-junction cell under 500 Suns concentration in Las Vegas for a calendar year [57]. The 1.87/1.42/0.67 bandgap cell's efficiency was simulated using etaOpt. For this bandgap combination a maximum cell efficiency of 48.7% was found for the standard AM1.5d spectrum. This reduced to a 44.3% annual energy yield which they calculated as the ratio of total energy produced by the cell divided by total energy incident on the cell for a given year. Providing individual terminals to each cell in a stacked formation increased the simulated efficiency to 59.2% under the standard AM1.5d spectrum. The annual energy yield, however, was found to be 60.1% i.e. close to the simulated cell efficiency indicating the low losses seen as current matching constraints were removed.

2.6 Multi-junction solar cells with lattice constants equal or close to that of InP

Monolithic multi-junction solar cells based on a lattice parameter near that of GaAs are limited in the range of alloys accessible to match with the solar spectrum. It has been highlighted that a move to a multi-junction material system based on a lattice parameter approaching that of InP would offer greater potential for increasing overall cell efficiency [58]. Recently, the growth and fabrication of an InAlAs-based solar cell on an InP substrate has been reported with a 1-Sun efficiency of 14% [59] and this has further been extended to the demonstration of a InAlAs/InGaAsP/InGaAs triple-junction structure also lattice matched to InP with a 1-sun AM1.5d efficiency of 13.8% [60]. In order to further develop the feasibility of this material system for commercial multi-junction device production, there is a justification for considering alternatives to InP substrates given its cost, maximum available substrate diameter and mechanical robustness, in particular when compared with GaAs or Ge. Leite *et al*. have proposed a lattice matched multi-junction configuration based on a 5.807 Å lattice constant. The (1.93 eV)

InAlAs / (1.39 eV) InGaAsP / (0.96 eV) InGaAs bandgap combination has been proposed to achieve > 51% photovoltaic conversion efficiency under 100 suns using real-world material data [61]. A suitable substrate has been developed for lattice matched growth of this cell design using wafer scale strain engineering [62]. The complex fabrication process, however, involves epitaxial growth of $In_xGa_{1-x}As$ layers, substrate removal, thin layer handling and bonding to a host substrate which may lead to challenges during commercial development.

2.7 References

[1] W. Shockley and H. J. Queisser, "Detailed Balance Limit of Efficiency of p-n Junction Solar Cells," *J. Appl. Phys.*, vol. 32, no. 3, pp. 510–519, Mar. 1961.

[2] G. Letay and A. W. Bett, "EtaOpt - a program for calculating limiting efficiency and optimum bandgap structure for multi-bandgap solar cells and TPV cells," *Proc 17th EU-PVSEC Munich*, p. Paper VA1.25, 2001.

[3] W. Guter, J. Schone, S. P. Philipps, M. Steiner, G. Siefer, A. Wekkeli, E. Welser, E. Oliva, A. W. Bett, and F. Dimroth, "Current-matched triple-junction solar cell reaching 41.1% conversion efficiency under concentrated sunlight," *Appl. Phys. Lett.*, vol. 94, no. 22, pp. 223504–3, Jun. 2009.

[4] V. Sabnis, H. Yuen, and M. Wiemer, "High-efficiency multijunction solar cells employing dilute nitrides," *AIP Conf. Proc.*, vol. 1477, no. 1, pp. 14–19, Oct. 2012.

[5] M. A. Green, K. Emery, Y. Hishikawa, W. Warta, and E. D. Dunlop, "Solar cell efficiency tables (version 41)," *Prog. Photovoltaics Res. Appl.*, vol. 21, no. 1, pp. 1–11, 2013.

[6] C. L. Andre, D. M. Wilt, A. J. Pitera, M. L. Lee, E. A. Fitzgerald, and S. A. Ringel, "Impact of dislocation densities on n+/p and p+/n junction GaAs diodes and solar cells on SiGe virtual substrates.," *J. Appl. Phys.*, vol. 98, no. 1, p. 014502, 2005.

[7] S. Wojtczuk, P. Chiu, X. Zhang, D. Pulver, C. Harris, and M. Timmons, "Bifacial Growth InGaP/GaAs/InGaAs Concentrator Solar Cells," *IEEE J. Photovoltaics*, vol. 2, no. 3, pp. 371–376, 2012.

[8] M.Z. Shvarts,, V.P. Khvostikov, V.M. Lantratov, N.K. Timoshina, "InGaP/GaAs–GaSb and InGaP/GaAs/Ge–InGaAsSb hybrid monolithic/stacked tandem concentrator solar cells," *Proc. 24th EUPVSEC*, 2006.

[9] A. W. Bett, "Overview of Technology Perspectives for High Efficiency Solar Cells for Terrestrial and Space Applications," in *in Proceedings of the 28th European Photovoltaic Solar Energy Conference and Exhibition*, Paris, 2013.

[10] R. R. King, D. Bhusari, A. Boca, D. Larrabee, X.-Q. Liu, W. Hong, C. M. Fetzer, D. C. Law, and N. H. Karam, "Band gap-voltage offset and energy production in next-generation multijunction solar cells," *Prog. Photovoltaics Res. Appl.*, vol. 19, no. 7, pp. 797–812, 2010.

[11] T. Yamada, A. Moto, Y. Iguchi, M. Takahashi, S. Tanaka, T. Tanabe, and S. Takagishi, "5× 5 cm2 GaAs and GaInAs Solar Cells with High Conversion Efficiency," *Jpn. J. Appl. Phys.*, vol. 44, pp. L985–L987, Jul. 2005.

[12] T. Yamada, A. Moto, Y. Iguchi, M. Takahashi, S. Tanaka, T. Tanabe, and S. Takagishi, "Mechanically Stacked GaAs/GaInAsP Dual-Junction Solar Cell with High Conversion Efficiency of More than 31%," *Jpn. J. Appl. Phys.*, vol. 44, pp. L988–L990, Jul. 2005.

[13] J. Yang, Z. Peng, D. Cheong, and R. N. Kleiman, “III-V on Silicon Multi-Junction Solar Cell with 25% 1-Sun Efficiency via Direct Metal Interconnect and Areal Current Matching,” in *in Proceedings of the 27th European Photovoltaic Solar Energy Conference and Exhibition*, Frankfurt, Germany, 2012.

[14] L. Zhao, G. Flamand, Y. Mols, J. Van der Heide, and J. Poortmans, “Novel Mechanically Stacked Multi-Junction Solar Cells Applying Ultra-Thin III-V Cells and Wafer Based Germanium Cell,” 2010, pp. 1123–1128.

[15] D. D. Krut, B. T. Cavicchi, and D. R. Lillington, “The development of Ge bottom cell for monolithic and stacked multi-junction applications,” in *Photovoltaic Specialists Conference, 1991., Conference Record of the Twenty Second IEEE*, 1991, pp. 90–92 vol.1.

[16] D. J. Friedman and J. M. Olson, “Analysis of Ge junctions for GaInP/GaAs/Ge three-junction solar cells,” *Prog. Photovoltaics Res. Appl.*, vol. 9, no. 3, pp. 179–189, 2001.

[17] N. E. Posthuma, J. van der Heide, G. Flamand, and J. Poortmans, “Emitter Formation and Contact Realization by Diffusion for Germanium Photovoltaic Devices,” *IEEE Trans. Electron Devices*, vol. 54, no. 5, pp. 1210–1215, May 2007.

[18] N. E. Posthuma, G. Flamand, W. Geens, and J. Poortmans, “Surface passivation for germanium photovoltaic cells,” *Sol. Energy Mater. Sol. Cells*, vol. 88, no. 1, pp. 37–45, Jun. 2005.

[19] V. P. Khvostikov, O. A. Khvostikova, P. Y. Gazaryan, S. V. Sorokina, N. S. Potapovich, A. V. Malevskaya, N. A. Kaluzhniy, M. Z. Shvarts, and V. M. Andreev, “Photovoltaic Cells Based on GaSb and Ge for Solar and Thermophotovoltaic Applications,” *J. Sol. Energy Eng.*, vol. 129, no. 3, pp. 291–297, 2007.

[20] O. V. Sulima and A. W. Bett, “Fabrication and simulation of GaSb thermophotovoltaic cells,” *Sol. Energy Mater. Sol. Cells*, vol. 66, no. 1–4, pp. 533–540, Feb. 2001.

[21] A. W. Bett, “Development of high-efficiency mechanically stacked GalnP/GalnAs-GaSb triple junction concentrator solar cells,” 2001.

[22] A. W. Bett, F. Dimroth, M. Hein, G. Lange, M. Meusel, U. Schubert, and G. Siefer, “Development of III-V-based concentrator solar cells and their application in PV-modules,” in *Photovoltaic Specialists Conference, 2002. Conference Record of the Twenty-Ninth IEEE*, 2002, pp. 844–847.

[23] H. Matsubara, T. Tanabe, A. Moto, Y. Mine, and S. Takagishi, “Over 27% efficiency GaAs/InGaAs mechanically stacked solar cell,” *Sol. Energy Mater. Sol. Cells*, vol. 50, no. 1–4, pp. 177–184, Jan. 1998.

[24] V. M. Andreev, L. B. Karlina, A. B. Kazantsev, V. P. Khvostikov, V. D. Rumyantsev, S. V. Sorokina, and M. Z. Shvarts, “Concentrator tandem solar cells based on AlGaAs/GaAs-InP/InGaAs(or GaSb) structures,” in *Photovoltaic Energy Conversion, 1994., Conference Record of the Twenty Fourth. IEEE Photovoltaic Specialists Conference - 1994, 1994 IEEE First World Conference on*, 1994, vol. 2, pp. 1721–1724 vol.2.

[25] L. B. Karlina, A. S. Vlasov, M. M. Kulagina, E. P. Rakova, N. K. Timoshina, and V. M. Andreev, “Highly Efficient Photovoltaic Cells Based on In0.53Ga0.47As Alloys with Isovalent Doping,” *Semiconductors*, vol. 44, no. 2, pp. 228–232, 2010.

[26] M. Emziane, R. J. Nicholas, D. C. Rogers, and J. Dosanjh, “Investigation of InGaAsP-based solar cells for double-junction photovoltaic devices,” *Thin Solid Films*, vol. 516, no. 20, pp. 6744–6747, Aug. 2008.

[27] N. Szabó, B. E. Sağol, U. Seidel, K. Schwarzburg, and T. Hannappel, “InGaAsP/InGaAs tandem cells for a solar cell configuration with more than three junctions,” *Phys. Status Solidi RRL - Rapid Res. Lett.*, vol. 2, no. 6, pp. 254–256, Dec. 2008.

[28] A. Barnett, X. Wang, N. Waite, P. Murcia, C. Honsberg, D. Kirkpatrick, D. Laubacher, F. Kiamilev, K. Goossen, M. Wanlass, M. Steiner, R. Schwartz, J. Gray, P. Sharps, K. Emery, and L. Kazmerski, “Initial test bed for Very High Efficiency Solar Cell,” in *Photovoltaic Specialists Conference, 2008. PVSC ’08. 33rd IEEE*, 2008, pp. 1–7.

[29] M. A. Steiner, M. W. Wanlass, J. J. Carapella, A. Duda, J. S. Ward, T. E. Moriarty, and K. A. Emery, “A monolithic three-terminal GaInAsP/GaInAs tandem solar cell,” *Prog. Photovoltaics Res. Appl.*, vol. 17, no. 8, pp. 587–593, 2009.

[30] J.G. Werthen, B.A. Arau, C.W. Ford, N.R. Kaminar, M.S. Kuryla, M.L. Ristow, C.R. Lewis, H.F. MacMillan, G.F. Virshup, and J.M. Gee, “Recent advances in high-efficiency InGaAs concentrator cells,” in *Photovoltaic Specialists Conference, 1988., Conference Record of the Twentieth IEEE*, 1988, pp. 640–643 vol.1.

[31] H. Taguchi, T. Soga, and T. Jimbo, “Epitaxial lift-off process for GaAs solar cell on Si substrate,” *Sol. Energy Mater. Sol. Cells*, vol. 85, no. 1, pp. 85–89, Jan. 2005.

[32] K. Derendorf, S. Essig, E. Oliva, V. Klinger, T. Roesener, S. P. Philipps, J. Benick, M. Hermle, M. Schachtner, G. Siefer, W. Jager, and F. Dimroth, “Fabrication of GaInP/GaAs//Si Solar Cells by Surface Activated Direct Wafer Bonding,” *IEEE J. Photovoltaics*, vol. 3, no. 4, pp. 1423–1428, 2013.

[33] M. Steiner, S. P. Philipps, M. Hermle, A. W. Bett, and F. Dimroth, “Validated front contact grid simulation for GaAs solar cells under concentrated sunlight,” *Prog. Photovoltaics Res. Appl.*, vol. 19, no. 1, pp. 73–83, 2011.

[34] D. A. Clugston and P. A. Basore, “PC1D version 5: 32-bit solar cell modeling on personal computers,” in , *Conference Record of the Twenty-Sixth IEEE Photovoltaic Specialists Conference, 1997*, 1997, pp. 207 –210.

[35] T. Sameshima, J. Takenezawa, M. Hasumi, T. Koida, T. Kaneko, M. Karasawa, and M. Kondo, “Multi Junction Solar Cells Stacked with Transparent and Conductive Adhesive,” *Jpn. J. Appl. Phys.*, vol. 50, no. 5, p. 052301, 2011.

[36] L. Zhao, G. Flamand, Y. Mols, J. van der Heide, and J. Poortmans, “Development of ultra-thin one-side contacted GaAs solar cells for mechanically stacked multi-junction solar cells,” in *2009 34th IEEE Photovoltaic Specialists Conference (PVSC)*, Philadelphia, PA, USA, 2009, pp. 000202–000205.

[37] K. Tanabe, A. Fontcuberta i Morral, H. A. Atwater, D. J. Aiken, and M. W. Wanlass, “Direct-bonded GaAs/InGaAs tandem solar cell,” *Appl. Phys. Lett.*, vol. 89, no. 10, pp. 102106–3, 2006.

[38] D. Bhusari, D. Law, R. Woo, J. Boisvert, S. Mesropian, D. Larrabee, W. Hong, and N. Karam, “Direct Semiconductor Bonding Technology (SBT) for high efficiency III-V multi-junction solar cells,” in *2011 37th IEEE Photovoltaic Specialists Conference (PVSC)*, 2011, pp. 001937 –001940.

[39] D. Aiken, P. Sharps, M. Stan, H. Atwater, A. Fontcuberta i Morral, J. Zahler, and M. Wanlass, “Development of a high efficiency mechanically stacked multi-junction solar cell,” 2005. [Online]. Available: http://authors.library.caltech.edu/8556/. [Accessed: 15-Jan-2010].

[40] C.-T. Lin, W. E. McMahon, J. S. Ward, J. F. Geisz, M. W. Wanlass, J. J. Carapella, W. Olavarria, M. Young, M. A. Steiner, R. M. Frances, A. E. Kibbler, A. Duda, J. M. Olson, E. E. Perl, D. J. Friedman, and J. E. Bowers, “Fabrication of two-terminal metal-interconnected multijunction III-V solar cells,” in *2012 38th IEEE Photovoltaic Specialists Conference (PVSC)*, 2012, pp. 000944 –000948.

[41] A. Boca, J. C. Boisvert, D. C. Law, S. Mesropian, N. H. Karam, W. D. Hong, R. L. Woo, D. M. Bhusari, E. Turevskaya, P. Mack, and P. Glatkowski, "Carbon nanotube-composite wafer bonding for ultra-high efficiency III–V multijunction solar cells," in *Photovoltaic Specialists Conference (PVSC), 2010 35th IEEE*, 2010, pp. 003310–003315.

[42] W. G. Spitzer and J. M. Whelan, "Infrared Absorption and Electron Effective Mass in n-Type Gallium Arsenide," *Phys. Rev.*, vol. 114, no. 1, pp. 59–63, Apr. 1959.

[43] G. J. Bauhuis, P. Mulder, E. J. Haverkamp, J. C. C. M. Huijben, and J. J. Schermer, "26.1% thin-film GaAs solar cell using epitaxial lift-off," *Sol. Energy Mater. Sol. Cells*, vol. 93, no. 9, pp. 1488–1491, Sep. 2009.

[44] N. G. Toledo, D. J. Friedman, R. M. Farrell, E. E. Perl, C.-T. (Tony) Lin, J. E. Bowers, J. S. Speck, and U. K. Mishra, "Design of integrated III-nitride/non-III-nitride tandem photovoltaic devices," *J. Appl. Phys.*, vol. 111, no. 5, pp. 054503–054503–8, Mar. 2012.

[45] D. J. Aiken, "High performance anti-reflection coatings for broadband multi-junction solar cells," *Sol. Energy Mater. Sol. Cells*, vol. 64, no. 4, pp. 393–404, Nov. 2000.

[46] M. J. Minot, "Single-layer, gradient refractive index antireflection films effective from 0.35 to 2.5 μ," *J. Opt. Soc. Am.*, vol. 66, no. 6, pp. 515–519, Jun. 1976.

[47] D. J. Poxson, M. F. Schubert, F. W. Mont, E. F. Schubert, and J. K. Kim, "Broadband omnidirectional antireflection coatings optimized by genetic algorithm," *Opt. Lett.*, vol. 34, no. 6, pp. 728–730, Mar. 2009.

[48] S. R. Kennedy and M. J. Brett, "Porous Broadband Antireflection Coating by Glancing Angle Deposition," *Appl. Opt.*, vol. 42, no. 22, pp. 4573–4579, Aug. 2003.

[49] R. L. Moon, L. W. James, H. A. Vander Plas, T. O. Yep, G. A. Antypas, and Y. Chai, 'Multigap solar cell requirements and the performance of AlGaAs and Si cells in concentrated sunlight', in *13th Photovoltaic Specialists Conference*, 1978, vol. -1, pp. 859–867.

[50] A. Barnett, C. Honsberg, D. Kirkpatrick, S. Kurtz, D. Moore, D. Salzman, R. Schwartz, J. Gray, S. Bowden, K. Goossen, M. Haney, D. Aiken, M. Wanlass, and K. Emery, "50% Efficient Solar Cell Architectures and Designs," in *Photovoltaic Energy Conversion, Conference Record of the 2006 IEEE 4th World Conference on*, 2006, vol. 2, pp. 2560–2564.

[51] J. D. McCambridge, M. A. Steiner, B. L. Unger, K. A. Emery, E. L. Christensen, M. W. Wanlass, A. L. Gray, L. Takacs, R. Buelow, T. A. McCollum, J. W. Ashmead, G. R. Schmidt, A. W. Haas, J. R. Wilcox, J. Van Meter, J. L. Gray, D. T. Moore, A. M. Barnett, and R. J. Schwartz, "Compact spectrum splitting photovoltaic module with high efficiency," *Prog. Photovoltaics Res. Appl.*, vol. 19, no. 3, pp. 352–360, May 2011.

[52] B. GroB, G. Peharz, G. Siefer, M. Peters, J. C. Goldschmidt, M. A. Steiner, W. Guter, V. Klinger, B. George, and F. Dimroth, "Highly Efficient Light Splitting Photovoltaic Receiver," in *Proceedings of the 24th European Photovoltaic Solar Energy Conference*, Hamburg, Germany, 2009.

[53] B. Mitchell, G. Peharz, G. Siefer, M. Peters, T. Gandy, J. C. Goldschmidt, J. Benick, S. W. Glunz, A. W. Bett, and F. Dimroth, "Four-junction spectral beam-splitting photovoltaic receiver with high optical efficiency," *Prog. Photovoltaics Res. Appl.*, vol. 19, no. 1, pp. 61–72, Jan. 2011.

[54] A. S. Vlasov, V. P. Khvostikov, L. B. Karlina, S. V. Sorokina, N. S. Potapovich, M. Z. Shvarts, N. K. Timoshina, V. M. Lantratov, S. A. Mintairov, N. A. Kalyuzhnyy, E. P. Rakova, V. I. Vasil'ev, and V. M. Andreev, "Spectral Splitting CPV Modules with AlGaAs/GaAs/GaSb and GaInP/GaAs/InGaAs(P)

Solar Cells," in *Proceedings of the 26th European Photovoltaic Solar Energy Conference and Exhibition*, Hamburg, Germany, 2011.

[55] R. R. King, C. M. Fetzer, P. C. Colter, K. M. Edmondson, D. C. Law, A. P. Stavrides, H. Yoon, G. S. Kinsey, H. L. Cotal, J. H. Ermer, R. A. Sherif, and N. H. Karam, "Lattice-matched and metamorphic GaInP/GaInAs/Ge concentrator solar cells," in *Conference Record, 3rd World Conference on Photovoltaic Energy Conversion*, Osaka, 2003.

[56] M. W. Wanlass, S. P. Abrenkiel, D. S. Albin, K. Emery, J. J. Carapella, A. Duda, J. F. Geisz, S. Kurtz, T. Moriarty, and M. J. Romero, "GaInP/GaAs/GaInAs monolithic tandem cells for high-performance solar concentrators.," in *Proceedings of the International Conference on Solar Concentrators for the Generation of Electricity or Hydrogen*, Scottsdale, Arizona, 2005.

[57] Y. Mols, L. Zhao, G. Flamand, M. Meuris, and J. Poortmans, "Annual energy yield: A comparison between various monolithic and mechanically stacked multijunction solar cells," in *2012 38th IEEE Photovoltaic Specialists Conference (PVSC)*, 2012, pp. 002092–002095.

[58] M. P. Lumb, M. Gonzalez, I. Vurgaftman, J. R. Meyer, J. Abell, M. Yakes, R. Hoheisel, J. G. Tischler, P. P. Jenkins, P. N. Stavrinou, M. Fuhrer, N. J. Ekins-Daukes, and R. J. Walters, "Simulation of novel InAlAsSb solar cells," 2012, p. 82560S–82560S–13.

[59] M. S. Leite, R. L. Woo, W. D. Hong, D. C. Law, and H. A. Atwater, "Wide-band-gap InAlAs solar cell for an alternative multijunction approach," *Appl. Phys. Lett.*, vol. 98, p. 093502, 2011.

[60] R. L. Woo, W. D. Hong, S. Mesropian, M. S. Leite, H. A. Atwater, and D. C. Law, "First Demonstration of Monolithic InP-Based InAIAs/InGaAsP/InGaAs Triple Junction Solar Cells," in *Proceeedings of the 37th IEEE Photovoltaic Specialists Conference*, Seattle, Washington, 2011.

[61] M. S. Leite and H. A. Atwater, "Device modeling of an Optimized monolithic all lattice-matched 3-Junction solar cell with efficiency > 50%," in *Proceeedings of the 38th IEEE Photovoltaic Specialists Conference*, Austin, Texas, 2012.

[62] M. S. Leite, E. C. Warmann, G. M. Kimball, S. P. Burgos, D. M. Callahan, and H. A. Atwater, "Wafer-Scale Strain Engineering of Ultrathin Semiconductor Crystalline Layers," *Adv. Mater.*, vol. 23, no. 33, pp. 3801–3807, Sep. 2011.

[63] I. Mathews, D. O'Mahony, A. Gocalinska, M. Manganaro, E. Pelucchi, M. Schmidt, A. P. Morrison, and B. Corbett, "InAlAs solar cell on a GaAs substrate employing a graded InxGa1−xAs–InP metamorphic buffer layer," *Appl. Phys. Lett.*, vol. 102, no. 3, pp. 033906–033906–4, Jan. 2013.

Chapter 3

Simulation and design of the photovoltaic properties of mechanically stacked solar cells

3.1. Introduction

The first half of this chapter outlines the development of an electrical and optical solar cell modelling approach used to investigate the potential performance of Mechanically Stacked Solar Cells (MSSC). The efficiency of solar cell and terminal configurations which avoid the need for complex bandgap engineering or advanced epitaxy capability were evaluated. Multi-junction solar cells consisting of $Al_{0.3}Ga_{0.7}As$, GaAs, Si and $In_{0.53}Ga_{0.47}As$ were considered for their ready availability and coverage of the broad solar spectrum range. A stacked solar cell consisting of a dual-junction $Al_{0.3}Ga_{0.7}As$/GaAs top cell and separately connected $In_{0.53}Ga_{0.47}As$ bottom cell was chosen as the most suitable combination for high performance.

In the second half of this chapter adhesive bonding of the top and bottom cells to form an MSSC was investigated as a fabrication route. The effect of an adhesive bond on the thermal and optical performance of the stack under concentration and the subsequent efficiency drop was modelled. BCB is proposed as a suitable adhesive to bond and form an MSSC which combined with a suitable optical coating design minimizes interface reflection between the cells. Finally a design specification for an MSSC combining a GaAs top cell, InGaAs bottom cell and BCB adhesive bond interface is given.

3.2. Modelling solar cell and terminal configuration

The ideal diode equations for photovoltaics introduced in Chapter 1 were used to determine the electrical performance of solar cells. The model is based on the semiconductor transport properties of each material and its absorption profile. It was assumed the solar cell junction behaves according to the ideal current-voltage relationship of a single-diode (Equation 3.3) where bulk minority carrier lifetimes for the *p* and *n* type regions of the solar cells were used to estimate

the recombination current density. Each absorbed photon was assumed to create one electron-hole pair and no ohmic or optical losses were considered. While these assumptions will result in an overestimation of the performance of the multi-junction solar cells, since in practical applications these losses are non-zero, the model can be used to assess the relative performance of each technology.

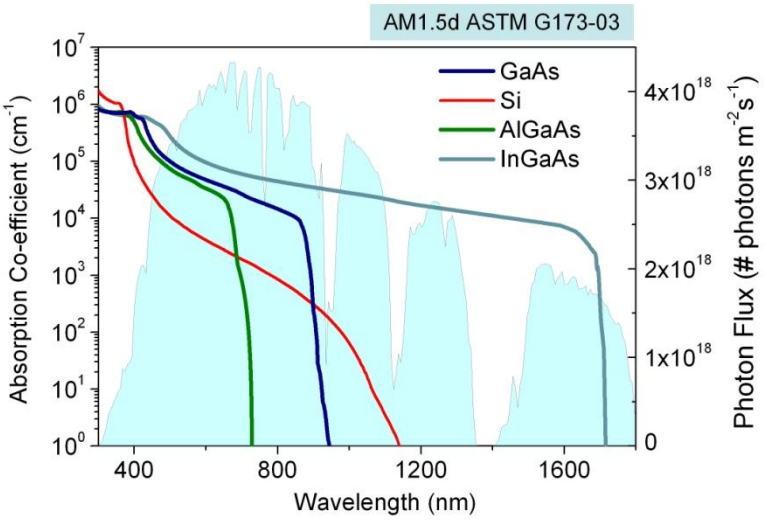


Figure 3.1: The absorption co-efficients of the materials considered for multi-junction solar cells. The AM1.5d ASTM G173-03 spectrum is shown for comparison. References as in Fig. 1.7.

The light generated current per unit area, J_L (mA/cm^2), in a cell was determined using the AM1.5 Direct Solar Spectrum from the ASTM G-173-03 reference standard [1]. The photon flux, *PF(λ)* (# photons m^{-2}s^{-1}) incident on a solar cell was determined using Equation 3.1 where, I_o, is the power density (W m^{-2} nm^{-1}) of the AM1.5 direct solar spectrum at wavelength λ (nm), *h*, is planck's constant and *c*, is the speed of light.

$$PF(\lambda) = \frac{I_o(\lambda)}{hc/\lambda}\Delta\lambda \tag{3.1}$$

The absorption profile and thickness of each material in a solar cell have been used to determine J_L, where, *α(λ)*, is the absorption co-efficient as a function of wavelength. The absorption profiles given in Figure 3.1 were taken from the literature [2], [3]. The light generated current per unit area, J_L, was taken as the number of photons absorbed across the entire thickness of the solar cell, *x*, as in Equation 3.2 where, *q*, is the charge per electron.

$$J_L = \int_{280\ nm}^{\lambda=2500\ nm} qPF(\lambda)(1 - e^{-\alpha(\lambda)x})\Delta\lambda \quad (3.2)$$

The ideal diode equation (Equation 3.3) was used to determine the photocurrent density-voltage, *J(V),* characteristics of a solar cell where, *T*, is the temperature of the cell taken as 300 K and, *k*, is Boltzmann's constant.

$$J(V) = J_o\left(e^{\frac{qV}{kT}} - 1\right) - J_L \quad (3.3)$$

In the case of a multi-junction solar cell the spectrum incident on the nth material junction, I_n, was adjusted for absorption in the preceding materials as in Equation 3.4 where, d_{n-1}, (cm) is the thickness of the preceding material and, I_{n-1}, is the illumination intensity incident on the previous junction ($I_n = I_o$ for the top junction).

$$I_n(\lambda) = I_{n-1}(\lambda)e^{-\alpha(\lambda)d_{n-1}} \quad (3.4)$$

The recombination current per unit area (Equation 3.5), J_o, was calculated as the sum of the contribution of the n- and p-type layers assuming uniform doping in each.

$$J_o = qn_i^2\left(\frac{D_e}{N_A L_e} + \frac{D_h}{N_D L_h}\right) \quad (3.5)$$

The intrinsic carrier concentration (n_i), the minority carrier diffusion constants (D_e, D_h) and the electron and hole minority carrier diffusion lengths (L_e, L_h) are calculated in the usual manner. The minority carrier mobilities (μ_e, μ_h) and minority carrier lifetimes (τ_e, τ_h) are taken from the literature and are given in Table 3.1.

When a number of junctions are series-connected, the current matching condition was first found using an iterative process by varying the thickness of each junction so the contribution from each was equal and maximised. It should be noted that this optimisation should be carried out while considering the operating current of the device, J_{MPP}, but in this case the light-generated current density, J_L, was used as it was deemed to be sufficiently similar to not greatly reduce the accuracy of the model. The illuminated photocurrent-density voltage characteristics of a series-connected multi-junction solar cell with *n* integer junctions were found by adding the voltages of each junction when this matched current was present in each (Equation 3.6) where .

$$V = \sum_{i=1}^{n} \frac{kT}{q}\left[ln\left(\frac{J + J_{Li}}{J_{oi}} + 1\right)\right] \quad (3.6)$$

The maximum power output per unit area of a solar cell is found by differentiating the power output function of a solar cell and setting it to zero as in Equation 3.7.

$$P_{max}: \frac{d(JV)}{dJ} = 0 \quad (3.7)$$

Individual solar cells in a mechanical stack configuration are connected in parallel allowing separate load control of each cell. Therefore, the maximum power output per unit area of the stack is the sum of the maximum power output per unit area of the individual solar cells (Equation 3.7). The model considers solar cells connected in series and parallel, as required, and the photovoltaic conversion efficiency for each system is derived by finding the power output of the combined solar cells and dividing by the incident power. The photovoltaic conversion efficiency, η, is equal to P_{out}/P_{in} where the incident power of the AM1.5d spectrum is 888 W/m^2. The performance of each solar cell reported here were derived using the material properties given in Table 3.1.

Table 3.1: Semiconductor material properties at 300 K [4], [5], [6], [7], [8], [9].

	$Al_{0.3}Ga_{0.7}As$	**GaAs**	**Si**	**$In_{0.53}Ga_{0.47}As$**
N_A (cm^{-3})	$3x10^{18}$	$5x10^{18}$	$1x10^{18}$	$2x10^{18}$
N_D (cm^{-3})	$1x10^{17}$	$5x10^{17}$	$1x10^{16}$	$3x10^{17}$
n_i (cm^{-3})	$2.1x10^{3}$	$2x10^{6}$	$1x10^{10}$	$6.3x10^{11}$
μ_e ($cm^2 V^{-1}s^{-1}$)	1984	1200	1300	12000
μ_h ($cm^2 V^{-1}s^{-1}$)	135	250	90	300
τ_e (s)	$1x10^{-8}$	$2.5x10^{-9}$	$6x10^{-6}$	$7.5x10^{-9}$
τ_h (s)	$1x10^{-9}$	$7x10^{-8}$	$8x10^{-5}$	$8x10^{-8}$

3.2.1. Monolithic device structures

The bandgap of Si (1.1 eV) is close to the desired 1 eV for better spectral splitting with the lattice matched GaInP/GaAs material system. The performance of a 2-terminal device incorporating an

active Si bottom junction, as shown in Figure 3.2(a), is compared to a triple-junction solar cell with an $In_{0.53}Ga_{0.47}As$ bottom junction i.e. a device consisting of a bandgap combination close to the GaInP/GaAs/Ge material system. The benefit of inserting a fourth junction is also considered and a Si junction is placed between the high-bandgap AlGaAs/GaAs and low-bandgap InGaAs junctions to provide better current matching in a series connected 2-terminal configuration as shown in Figure 3.2(c). For all series connected cells a completely transparent and ideal ohmic contact was considered as the cell interconnect.

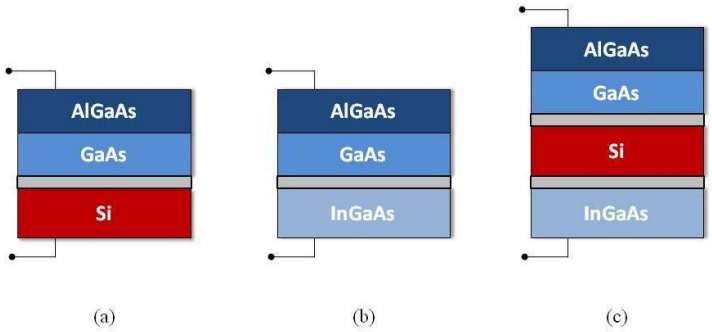


Figure 3.2: Triple-junction (a, b) and four-junction (c) series-connected multi-junction solar cell configurations modelled where the interface between Si and InGaAs and the other semiconductor materials is considered as a completely transparent and ideal ohmic contact.

3.2.2. Comparative stacked cells

Si is considered as the bottom junction under a dual junction $Al_{0.3}Ga_{0.7}As$/GaAs solar cell. The performance of an MSSC with an $In_{0.53}Ga_{0.47}As$ bottom junction is also analysed to compare the performance of the 1.1 eV and 0.75 eV devices. A four-junction MSSC is also considered which integrates both a Si and $In_{0.53}Ga_{0.47}As$ solar cell under a dual junction top cell in a 6-terminal configuration (Figure 3.3(c)). The Si cell thickness is varied to find the optimum value to split the spectrum between the two cells and give the maximum power output from these two cells combined.

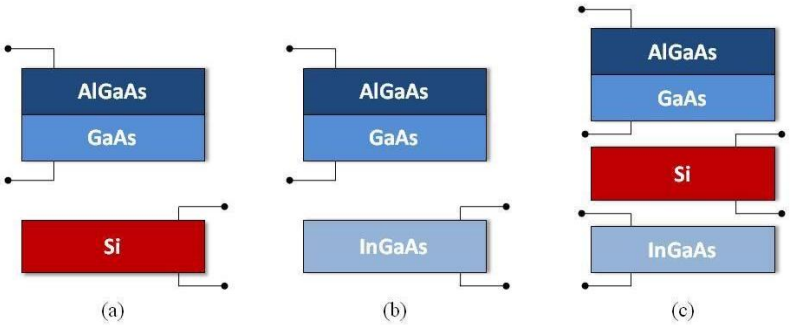


Figure 3.3: Triple-junction mechanically stacked solar cells formed using Si (a) and InGaAs (b) bottom solar cells and a four-junction configuration (c).

3.2.3. Modelling results

Monolithic devices

The first devices considered are monolithic 2- and 3-junction solar cells with only a 2 terminal connection, thus the individual subcells are connected in series and the photocurrent is limited accordingly. The photocurrent in the dual junction $Al_{0.3}Ga_{0.7}As$ /GaAs solar cell was matched and maximised at 14.4 mA/cm^2 for material thicknesses of 0.56 μm (AlGaAs) of and 3 μm (GaAs) respectively. Subsequently, an open-circuit voltage of 2.51 V and a photovoltaic conversion efficiency of 36.7% were determined for this cell combination, which was used as the top cell in a number of mechanically stacked solar cell configurations; the results of which are presented in the following sections.

A 200 μm Si substrate was considered as the bottom junction in a series connected triple-junction solar cell. The current of the device is limited by the Si junction as the 200 μm thick layer absorbs 97.1% of the transmitted photons below 1120 nm. The current matching condition for the AlGaAs, GaAs and Si junctions was found with an AlGaAs junction thickness of 0.38 μm and a GaAs junction thickness of 1.02 μm giving a light-generated current density of 13.1 mA/cm^2 in the device. This series-connected device has a relatively high open-circuit voltage of 2.89 V and an efficiency of 41.5%.

This device was compared to a triple-junction AlGaAs/GaAs/InGaAs solar cell. The lower bandgap material (~0.75 eV) absorbs a much higher portion of the spectrum transmitted by the AlGaAs and GaAs material layers (97.2% of photons below 1680 nm with an InGaAs thickness of 3.5 μm) and produces a higher current than a Si bottom junction allowing thicker top and middle junctions to be used in the device. The current through the device is limited by the

matching of the top two junctions with the limiting current being 14.4 mA/cm^2. A combined InGaAs emitter and base thickness of 0.48 μm is required to match this current. This device has an open-circuit voltage of 2.63 V under illumination and an efficiency of 41.3% which is marginally less than the Si-based series-connected triple-junction solar cell. It is clear that higher voltage Si-based triple-junction solar cells could achieve similar performance to current triple junction devices if suitable manufacturing processes can be found.

Table 3.2: Simulated performance summary for 2-terminal multi-junction configurations.

Device	J_{sc} (mA/cm^2)	V_{oc} (V)	Efficiency (%)
AlGaAs/GaAs	14.4	2.51	36.7
AlGaAs/GaAs/Si	13.1	2.89	41.5
AlGaAs/GaAs/InGaAs	14.4	2.63	41.3
AlGaAs/GaAs/Si/InGaAs	13.1	3.55	45.7

The performance of a four-junction device which utilises Si as the ~1 eV bandgap between the higher bandgap AlGaAs/GaAs materials and InGaAs was also modelled. The same current matching condition was found to exist for the 4J cell as the Si-based 3J cell since InGaAs strongly absorbs the spectrum transmitted by an AlGaAs/GaAs/Si device. The device produces a photocurrent of 13.1 mA/cm^2 with a combined InGaAs emitter and base thickness of 1.53 μm and gives a four-junction solar cell with an open-circuit voltage of 3.55 V. The overall efficiency is 45.7% or an increase of approximately 4% above both triple-junction cells simulated due to the added voltage of the 4th junction.

Mechanically stacked solar cells

Assuming no free-carrier absorption in the GaAs substrate, it was found that an AlGaAs/GaAs to Si mechanically stacked solar cell with Si thickness of 200 μm has an efficiency of 43.1% under 1-sun illumination. This is an improvement over a series connected AlGaAs/GaAs/Si triple-junction solar cell and results from complete utilisation of the current from the Si junction. The Si junction produces a short-circuit current density of 10.4 mA/cm^2. Figure 3.4 shows the performance of this stacked Si cell as a function of its thickness. It shows that mechanically

stacked thin-film Si solar cells will result in a significant efficiency boost even for thicknesses below 100 μm.

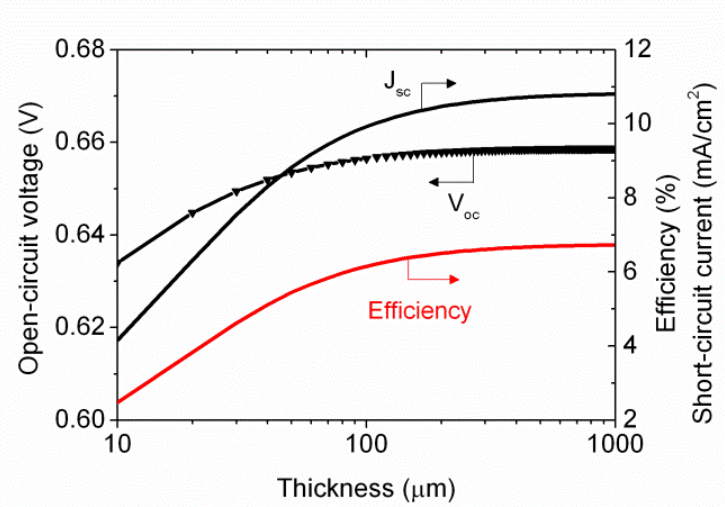


Figure 3.4: The modelled electrical performance of a Si solar cell mechanically stacked under a dual junction AlGaAs/GaAs solar cell as a function of Si thickness.

Lower bandgap materials are more suited for the bottom cell in MSSCs where the full current absorbed in this junction can be used if the solar cell is provided with parallel electrical contacts. It was found that an InGaAs solar cell with a combined emitter and base thickness of 3.5 μm resulted in a simulated short-circuit current density of 27.6 mA/cm^2 when stacked under an AlGaAs/GaAs dual junction top cell. Providing separate electrical connections to this junction as in a mechanical stack results in a simulated efficiency of 46.4%. This is approximately an absolute simulated efficiency increase of 5% over a monolithic triple-junction solar cell of the same material system.

The performance of the bottom cell in the AlGaAs/GaAs-InGaAs configuration is given in Figure 3.5 as a function of combined emitter and base thickness. Most of the benefit provided by this junction is achieved with a material thickness of 2 μm. While a higher photocurrent density can be achieved with greater thicknesses, the cost of growing the extra III-V materials would need to be considered against the performance increase. For the four-junction configuration described in the following section, an InGaAs active absorption thickness of 3.5 μm was used.

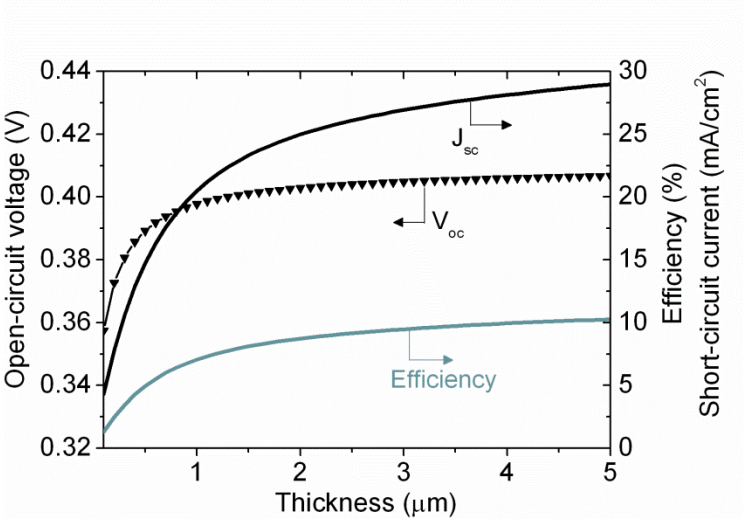


Figure 3.5: The modelled electrical performance of an InGaAs solar cell mechanically stacked under a dual junction AlGaAs/GaAs solar cell as a function of InGaAs combined emitter and base thickness.

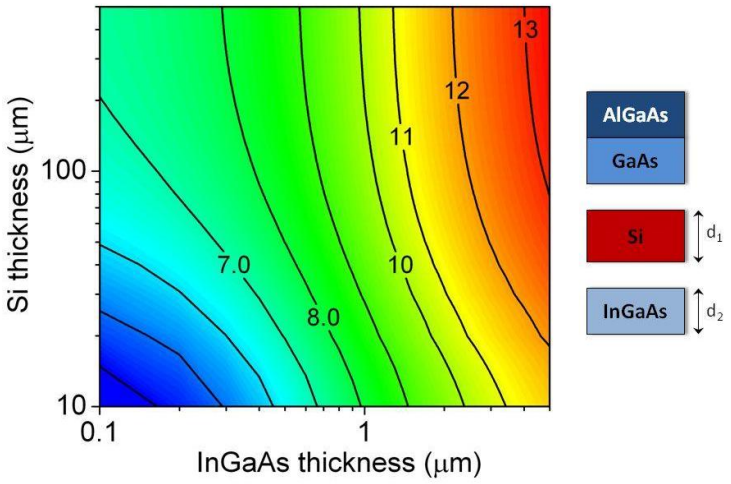


Figure 3.6: Iso-efficiency plot of the combined Si and InGaAs solar cell theoretical efficiencies (%) when stacked under an AlGaAs/GaAs dual junction solar cell as a function of Si (d_1) and InGaAs (d_2) thickness.

The final cell configuration considered is that of an AlGaAs/GaAs-Si-InGaAs structure with a 6-terminal connection. It is clear from Figure 3.6 that most of the efficiency boost provided to the stack is due to the InGaAs junction. A combined efficiency of 11.5% is found for the stacked Si and InGaAs cells using only 10 μm of Si with 5 μm of InGaAs while the same InGaAs thickness with 500 μm of Si yields a boost of 13%. The overall device efficiency using a more realistic 200 μm Si solar cell and an InGaAs active layer thickness of 3.5 μm is 49% or a boost of 12.3% to the

dual junction top cell. A summary of performance of the various multi-junction configurations is presented in Table 3.3 below, indicating that the 4-junction 6-terminal structure gives the highest overall efficiency of the devices considered.

Table 3.3: Simulated performance summary at 1-Sun illumination for each of the multi-junction technologies considered for integrating III-V and Si materials

Device	Number of Junctions	Efficiency (%)
AlGaAs/GaAs	2	36.7
AlGaAs/GaAs/Si	3	41.5
AlGaAs/GaAs/InGaAs	3	41.3
AlGaAs/GaAs/Si/InGaAs	4	45.7
AlGaAs/GaAs-Si	3	43.1
AlGaAs/GaAs-InGaAs	3	46.4
AlGaAs/GaAs-Si-InGaAs	4	49

'/' denotes current matched junctions

'-' denotes separate electrical connection

3.2.4. Efficiency versus illumination intensity

An analysis on the effect of concentration on photovoltaic conversion efficiency was carried out by increasing the illumination intensity of the AM1.5d spectrum while assuming that the junction temperature remained at 300 K. As this treatment of increased illumination intensity ignores the effect increasing temperature has on resistance, E_g narrowing and stresses and strains caused by the different thermal expansion coefficients of the materials used, the results presented are an upper limit to performance when considering the measured absorption coefficients of each material.

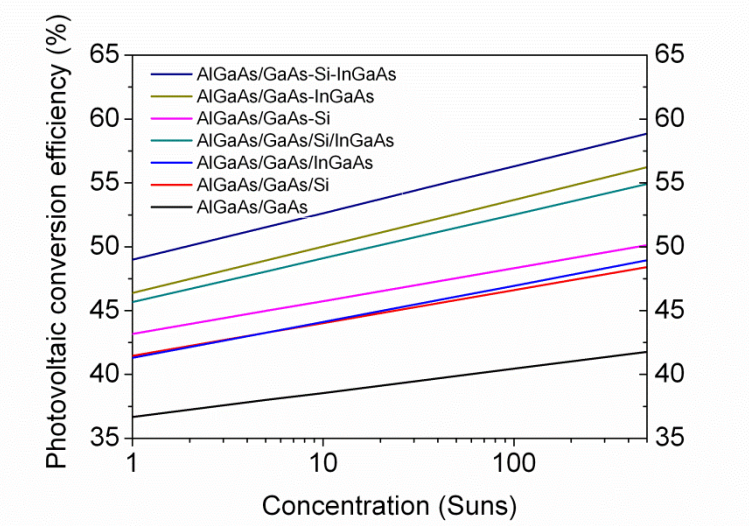


Figure 3.7: Efficiency versus solar intensity for each of the modelled solar cell configurations.

Under ideal operating conditions where reflection and thermal losses are ignored three of the solar cell configurations achieve greater than 50% efficiency under 500 suns concentration namely a 2- or 6- terminal, four-junction device or a triple-junction mechanical stack with a low *Eg* InGaAs bottom junction (Figure 3.7). The AlGaAs/GaAs-InGaAs stacked solar cell was chosen as a suitable cell design to proceed with owing to its high performance and the presence of only a single cell-to-cell interface. The rest of this chapter describes the design of an adhesively bonded GaAs-InGaAs tandem stack which acts as a prototype for a triple-junction MSSC.

3.3. Modelling the effect of an adhesive interface on a GaAs-InGaAs tandem stack

The model presented is further adapted to consider the effect of the optical and thermal interface between the solar cells under concentrated sunlight. Adhesive bonding was chosen as a fabrication route to reduce the refractive index step between the cells and provide a heat path for the thermal load in the top cell. A GaAs-InGaAs stack design is presented in Figure 3.8.

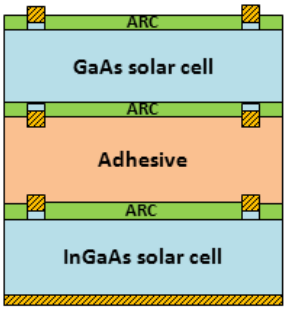


Figure 3.8: Outline of the prototype GaAs-InGaAs stacked tandem solar cell.

3.3.1. Reflection model

The transfer matrix method [10] is used to derive the reflection characteristics of multi-layered thin-film structures. Each thin film is characterised by its thickness d_j, complex refractive index $q_j = n_j(\lambda) + k_j(\lambda)$, the phase thickness of each layer $\varphi_j = 2\pi/\lambda.n_j.d_j$ and is represented by a 2 x 2 matrix of the form:

$$m = \begin{pmatrix} cos\varphi_j & \frac{i}{q_j} sin\varphi_j \\ iq_j sin\varphi_j & cos\varphi_j \end{pmatrix} \tag{3.8}$$

The complete thin-film system of N layers is associated with a matrix which is the product of all the individual layer matrices.

$$M = \prod_{j=1}^{N} \begin{pmatrix} cos\varphi_j & \frac{i}{q_j} sin\varphi_j \\ iq_j sin\varphi_j & cos\varphi_j \end{pmatrix} \tag{3.9}$$

The amplitude reflection factor is then given by Equation 3.10 where q_o and q_s are the complex refractive index of the initial and final media and the reflection amplitude is given by the square of it's absolute value as shown in Equation 3.11.

$$r = \frac{q_o M_{11} - q_s M_{22} + i(q_o q_s M_{12} - M_{21})}{q_o M_{11} + q_s M_{22} + i(q_o q_s M_{12} + M_{21})} \tag{3.10}$$

$$R = |r|^2 \tag{3.11}$$

The simulated light-generated current density is derived for a solar cell as given by Equation 3.12 where R(λ) is the reflection, A(λ) is the non-useful absorption in preceeding layers (comprised of absorption in dielectrics, adhesives, semiconductor substrates and window layers and accounted using the Beer-Lambert law.), α(λ) is the absorption co-efficient of the solar cell and x is the cell thickness.

$$J_L = q \int_{\lambda=280\ nm}^{\lambda=2500\ nm} \big(1 - R(\lambda)\big).\big(1 - A(\lambda)\big).PF(\lambda)\big(1 - e^{-\alpha(\lambda)x}\big)\Delta\lambda \tag{3.12}$$

As the spectrum considered extends from the deep UV (280 nm) to the near-infrared (1685 nm) each anti-reflection coating was optimised by maximising the current from the relevant photovoltaic junction. The dielectric layers considered for anti-reflection coating layers were SiO_2 and SiN deposited by Plasma Enhanced Chemical Vapour Deposition and ZnS deposited by e-beam evaporation. The complex refractive index of these materials was measured using spectroscopic ellipsometry and are presented in Figures 3.9 & 3.10.

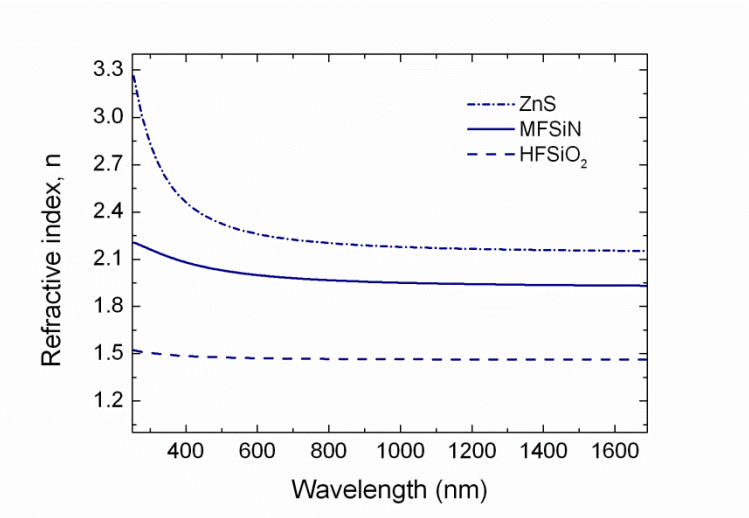


Figure 3.9: Measured refractive index (real-part) of the dielectric materials considered for anti-reflection coatings.

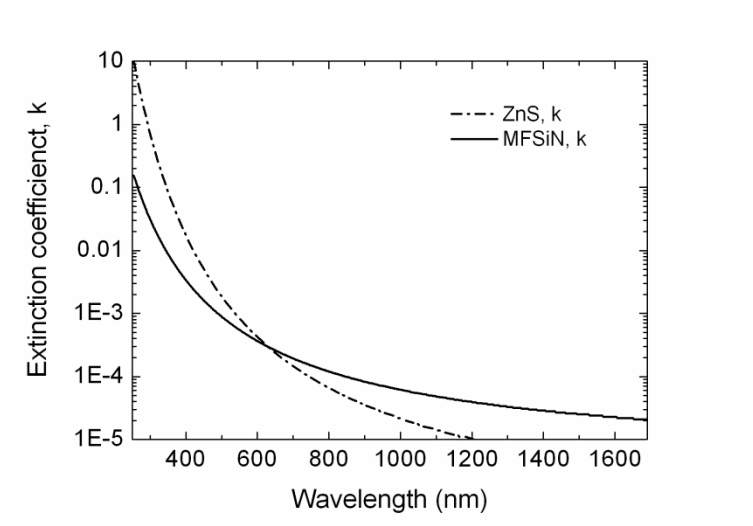


Figure 3.10: Measured extinction co-efficient of SiN_x and ZnS dielectric layers.

While absorption (Equation 3.13) was negligible in SiO_2 it was found to be significant in the UV range for SiN_x and ZnS.

$$\alpha = \frac{4\pi k}{\lambda} \tag{3.13}$$

The complex refractive index data compiled was used to model and optimise the transmission into each solar cell. Any absorption in substrates, window layers or dielectrics (i.e. not in the emitter or base layers) was considered to be outside the influence of the junction and did not contribute to the light-generated current density, $J_{L,}$ in a cell.

3.3.2. Front surface reflection

The first optical interface considered was the front-surface of the top solar cell. The anti-reflection coating for this surface was optimised by considering the photocurrent produced by the top cell only as it is the most significant contributor to the overall stack efficiency. The thin-film structure consists of an anti-reflection coating, for which single-layers of SiO_2, SiN, ZnS and a double layer SiO_2/ZnS were considered; a 40 nm $Al_{0.8}Ga_{0.2}As$ window layer and a final GaAs layer. The optimised anti-reflection coatings found for a single-junction GaAs solar cell are presented in Table 3.4.

Table 3.4: Optimised anti-reflection coating layers (ARC) for the front surface of a single-junction GaAs solar cell.

ARC	***Optimum thickness***	J_L
	nm	mA/cm^2
SiO_2	102	25.7
SiN_x	71	25.9
ZnS	65	24.85
SiO_2/ZnS	74/48	26.8

The double-layer system was found to have the highest transmission despite UV absorption in the ZnS layer. The reflection characteristics of the ARCs are shown in Figure 3.11. It can be seen the DLARC has the lowest reflection beyond the bandgap of GaAs although the light transmitted to a stacked InGaAs bottom cell suffers a significant reflection loss of 5 - 15% at the front surface.

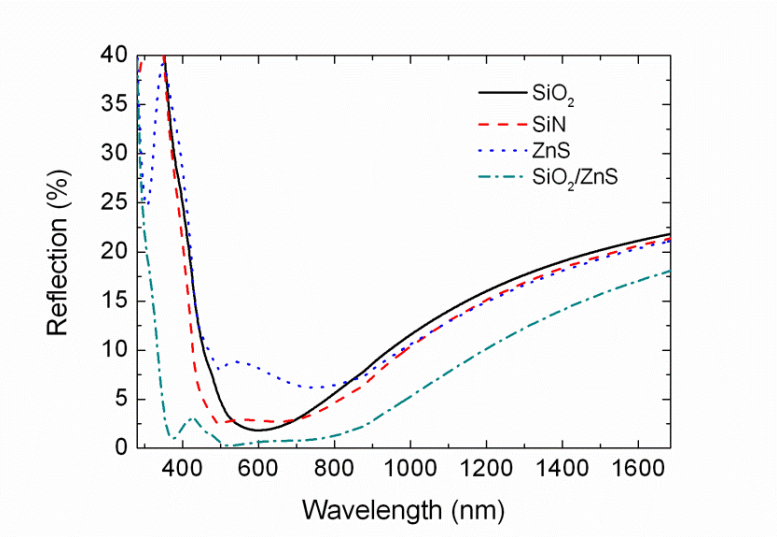


Figure 3.11: Simulated reflection from the front surface of a single-junction GaAs solar cell for each of the optimised ARC designs.

3.3.3. Adhesive Interface

In order to reduce reflection at the semiconductor interface index-matching adhesives were considered as bonding agents for the solar cells as well as the optimistaion of anti-reflection coatings for all optical interfaces in the between the cells. Three adhesives were chosen to

investigate their suitability for optical matching layers in mechanically stacked solar sells: benzocyclobutene, polyimide and polydimethylsiloxane. Their potential to increase transmission at the semiconductor interface was modelled. A brief discussion on their suitability for use in cell bonding and concentrating photovoltaic systems follows.

Benzocyclobutene (BCB)

BCB is used for low-temperature full wafer bonding in MEMS [11] and has the highest thermal conductivity of the adhesives investigated. Spin-coated BCB acts as a planarising layer in semiconductor fabrication and could be used to provide planar surfaces on each solar cell to improve bond adhesion. Void free bonds have been produced between 4" Si wafer pairs at a curing temperature of 180^{o}C using 4 μm of BCB [12]. BCB has a refractive index of 1.54 [13].

Polyimide

Polyimides are high refractive index polymers which are of interest for use in MEMS and adhesive wafer bonding [11]. Photodefinable polyimides are available which work with standard developers allowing patterning to provide access to metal contacts. While polyimide is highly absorbing at wavelengths below 500 nm it is suitable for use in a GaAs-InGaAs tandem stack as absorption between the relevant wavelength range of 880 – 1685 nm is weak. 90% void free bond areas have been achieved for 4" Si wafer pairs at a curing temperature of 300^{o}C [12]. Polyimide has already been used to a form a Si to a-Si tandem solar cell [14]. It has the highest refractive index of the adhesives considered at 1.78 [15].

Polydimethylsiloxane (PDMS)

PDMS is commonly used as a bonding agent in microfluidics [16]. It is investigated here as it is a low cost polymeric compound which can be cured at temperatures as low as 25^{o}C which would result in minimal stress if used with thinned solar cells. Furthermore patternable PDMS is available where it can be etched using dry etching techniques. It does, however, have the lowest refractive index at 1.41 [17].

3.3.4. Absorption of Adhesives

The absorption of each adhesive in the 880 – 1685 nm wavelength range is of critical importance for use in the stack and was measured by spin coating BCB (1.8 μm) and Polyimide (2.6 μm) and dispersing PDMS (50 μm) samples on a quartz substrate and measuring the reflection and transmission of the samples using a spectrophotometer. While absorption in polyimide and BCB is minimal, absorption peaks were measured in PDMS at the bandgap of InGaAs as shown in Figure 3.12. Optically, polyimide is the most suitable adhesive owing to its low absorption and high refractive index in the required wavelength range.

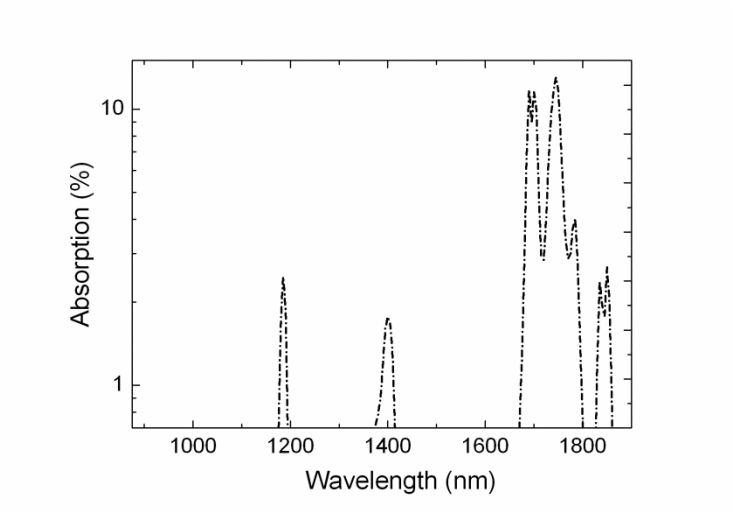


Figure 3.12: The measured absorption in PDMS.

The light-generated current density of an InGaAs solar cell stacked under a GaAs solar cell was modelled using the optical properties of the bonding adhesives. The broadband absorption co-efficient of an $In_{0.53}Ga_{0.47}As$ solar cell was used to integrate the photocurrent from the bottom cell post transmission through a GaAs top cell and the semiconductor/adhesive interface for the AM1.5d spectrum. Optimum single layer anti-reflection coatings were designed for between the semiconductor and adhesive by setting $n_{ARC} = (n_1 \times n_2)^{1/2}$ where n_1 was set to 3.5 to represent a semiconductor and n_2 is the refractive index of the adhesive and are given in Table 3.5. The transmission model could then be used to optimise the thickness of this ARC layer by setting the thickness of the adhesive layer to a value where it is optically thick and Fabry-Perot fringes will not occur (100 μm was used) and varying the thickness of the ARC layer. As a top cell a 4000 nm thick GaAs layer was considered with double layer anti-reflection SiO_2/ZnS (74/48 nm) coating

as was previously optimised. A 350 μm semi-insulating (no free-carrier absorption) GaAs substrate is considered which is optically thick and Fabry-Perot fringes within are not considered.

Table 3.5: Optimum ARC refractive index and thickness as a function of adhesive refractive index.

Interface refractive index	Optimum ARC refractive index	Optimised thickness
		nm
1.41	2.22	125
1.54	2.32	120
1.78	2.5	110

3.3.5. Adhesive thickness

The thickness of the adhesive is an important parameter in the performance of the optical coupling layers as it determines the magnitude of Fabry-Perot fringes created in the cavity. The light-generated current density generated by the InGaAs bottom cell was modelled as a function of the thickness of the adhesive layer. As adhesive layers are thermally resistive, a practical limit of 10 μm was chosen which was deemed achievable through spin-coating.

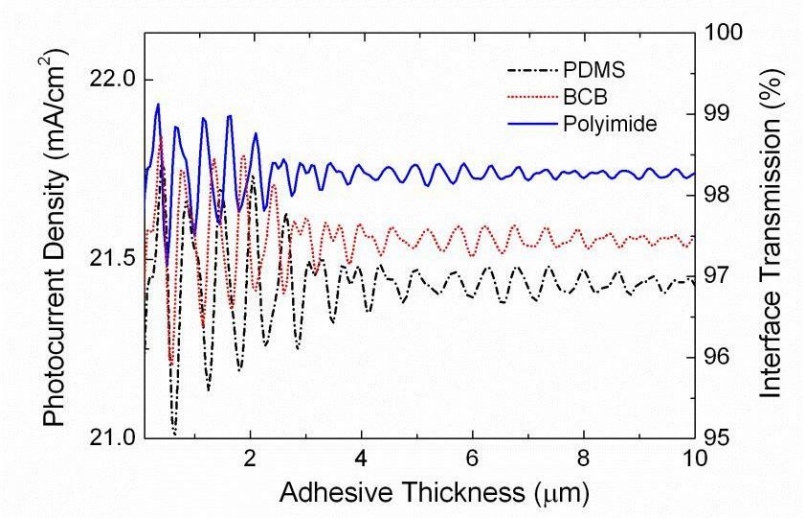


Figure 3.13: The simulated light-generated photocurrent density of an InGaAs cell stacked under a GaAs top cell as a function of adhesive and its thickness.

As shown in Figure 3.13, while the adhesive thickness does alter the transmission characteristics of the interface the maximum value of 99% transmission and minimum of 97.5% for a polyimide bond is only a difference of 1.5%. This is a much smaller optical loss than is expected for reflection at the front surface of the top cell or the absorption in any GaAs substrate. This small difference is likely due to the broad wavelength range under consideration where the increased reflection at certain wavelengths is mostly offset by decreases at alternative wavelengths as the thickness is adjusted. A high tolerance to adhesive layers thickness is seen for thicknesses of > 4 μm as any Fabry-Perot effects minimise.

3.3.6. Thermal modelling

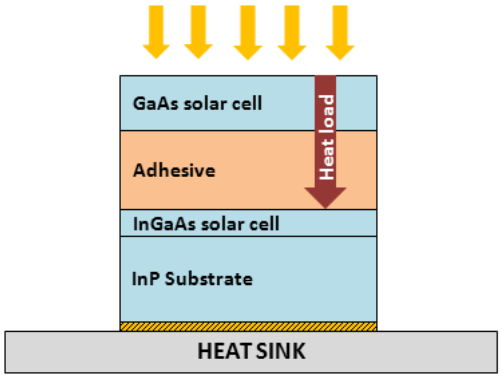


Figure 3.14: Outline of the thermal heat load and path for the tandem stack.

The use of adhesives to bond solar cells leads to an increased thermal resistance in the cell structure owing to the lower conductivities of adhesives when compared to semiconductors (Table 3.6). This is of critical importance in concentrating photovoltaic systems where the increased irradiance leads to a high thermal load on the cells which must be dissipated into a heat sink. A 2-dimensional analysis of the effect of the adhesive used and its thickness on the operating temperature of the GaAs top cell in the mechanical stack was carried out.

Table 3.6: The thermal properties of the materials considered for use in the GaAs-InGaAs tandem stack.

Material	Thermal conductivity (W/mK)	Linear Co-efficient of Thermal Expansion (ppm)
Polydimethlysiloxane	0.2	310
Benzocyclobutene	0.29	42
Polyimide	0.146	13
GaAs	55	5.73
$In_{0.53}Ga_{0.47}As$	5	5.66
InP	68	4.6

A thermal efficiency co-efficient of -0.04 %/K for a GaAs solar cells has been established and is used to determine the efficiency drop under concentration as a result of the thermal resistance of the adhesive layer [18]. The efficiency loss due to the adhesive thermal properties was calculated using Equation. 3.14 where, *t (μm)*, is the thickness of the adhesive layer, *Q (W/cm²)*, is the heat load from the cell and, *k (W/mK)*, the thermal conductivity of the adhesive.

$$\Delta\% = -0.04\left(\frac{t.Q}{k}\right) \tag{3.14}$$

The heat load in the cell was found for the AM1.5d spectrum by using the expected efficiency of a GaAs top cell and assuming all photons with energy greater than the *Eg* of GaAs are absorbed. Therefore the thermal load in the top cell is caused by the thermalisation of carriers with $E > Eg$. The incident power density of the AM1.5d spectrum is 888 W/m^2 with 69% of this absorbed in the top cell. Assuming a top cell efficiency of 28% under 500 suns [19] the portion of incident spectrum converted to heat load is 41% or 18.2 W/cm^2. The GaAs cell efficiency decrease due to the thermal resistance of the adhesive only is simulated. Additional thermal bridges are caused by the use of die attach to package the cell and the thermal resistance of the heat sink itself but these are ignored.

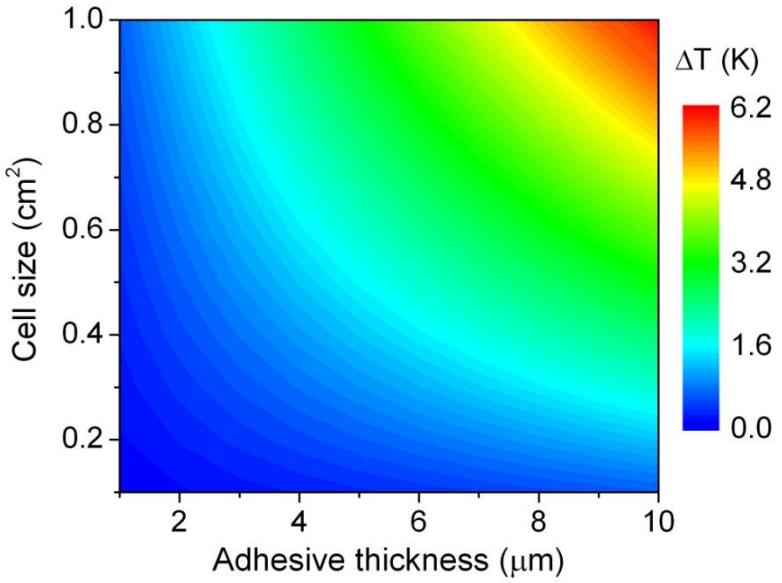


Figure 3.15: Temperature increase in a GaAs top cell as a function of BCB bond thickness and cell size under AM1.5d x500 Suns.

Figure 3.15 shows the temperature increase in the top cell as a function of adhesive thickness and the cell size for a BCB interface. An increase of 6.3 K is expected for a 10 μm adhesive layer bonding 1 cm^2 cells leading to an absolute cell efficiency loss of 0.25%. A similar analysis for Polyimide and PDMS led to temperature increases of 12.4 K and 9.1 K and absolute cell efficiency losses of 0.5% and 0.36% respectively.

A further consideration for cells bonded using adhesive is the different thermal expansion co-efficients of the various layers. Table 3.6 summaries the linear co-efficient of thermal expansion values (CTE) of the semiconductors as well as the proposed adhesives. Ideally an adhesive would have the same CTE as the semiconductors to which it is bonded as any difference will cause stress and strain in the layers during temperature changes. The difference in CTE could cause problems if the cells are bonded at elevated temperatures as any bond may weaken or fail during cooling. Polyimide has the closest CTE to the semiconductors with an approximate factor of two difference in CTE, compared with a x6 and x55 difference for BCB and PDMS, respectively.

3.3.7. Combined interface properties

The absolute efficiency loss in the bottom InGaAs cell due to reflection at the cell interface and the loss in the top GaAs cell due to the increased operating temperature caused by the low

thermal conductivity of the epoxy layer were combined in order to compare adhesive type and thickness. As both losses are independent they were added and the results shown in Figure 3.16 for a 1 cm^2 GaAs cell stacked on an InGaAs bottom cell under 500 suns operation. The analysis shows that for adhesive layer thicknesses of < 4 μm adhesive bonds using BCB or Polyimide perform similarly. At greater thicknesses the higher thermal conductivity of BCB results in lower losses as heat is removed more efficiently from the top cell. Given the results of the thermal and optical simulations, and the practical issues associated with obtaining void free layers, BCB was selected to be used in this study. Suitable layer thicknesses in the (6 – 10) μm range are achievable through spin-coating. While thinner layers would result in higher performance, electroplating of metal contacts is required for cells used in CPV systems in order to reduce series resistance. Therefore, thicker adhesive layers facilitate thicker metal contacts.

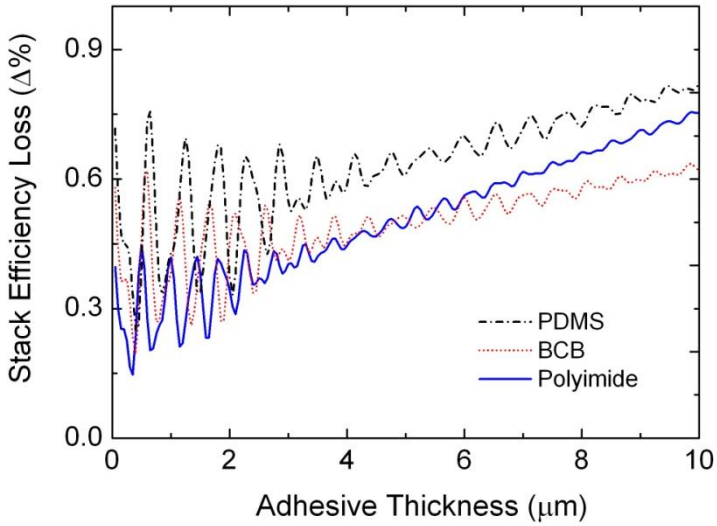


Figure 3.16: The overall stack efficiency losses due to the combined optical and thermal losses as a function of adhesive bonding layer material and thickness.

3.4. Final design and specifications

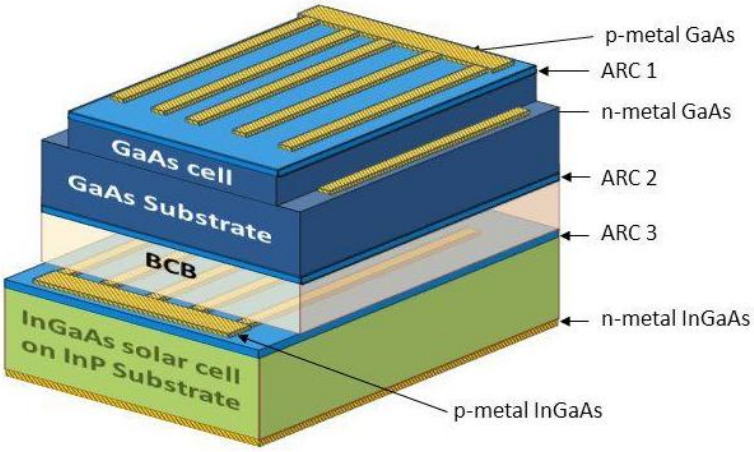


Figure 3.17: Schematic outline of the as designed MSSC.

Layer	Material	Thick.	Function	Fabrication	Performance Indicator
p-metal-GaAs	Ti/Pt/Au	30/50/200 nm	Ohmic contact to emitter layer	lithography, e-beam evap.	Top cell series resistance
n-metal-GaAs	Au/Ge/Au/Ni/Au	14/14/14/14/11/250 nm	Ohmic contact to n-substrate	mesa etch – lithography, e-beam evap.	Top cell series resistance
ARC 1	SiO_2/ZnS	74/48 nm	Broadband ARC	SiO_2: PECVD ZnS: e-beam evap.	Reflection measurement
Top cell	GaAs	Chapter 5	PV conversion	MOVPE	Cell efficiency
GaAs substrate	n-GaAs	Thin to 150 µm	Lateral current spreading, mechanical support of top cell	Double-side polished	Top cell series resistance, NIR absorption
ARC 2	ZnS	120 nm	Reduce reflection	e-beam evap.	InGaAs EQE (in stack)
Adhesive Bond	BCB	6 µm	Reduce reflection, securely bond cells	Flip-chip	InGaAs EQE (in stack)
ARC 3	SiN (Chapter 4)	140 nm	Passivate InGaAs sidewalls, reduce reflection	PECVD	InGaAs EQE (in stack), J_o of InGaAs cell
p-metal-InGaAs	Ti/Pt/Au	30/50/200 nm	Ohmic contact to emitter layer	lithography, e-beam evaporation	Bottom cell series resistance
Bottom cell	InGaAs	Chapter 4	PV conversion of NIR photons	MOVPE	Cell efficiency
InP substrate	InP	350 µm	Mechanical support of bottom cell		Bottom cell series resistance
n-metal-InGaAs	Au/Ge/Au/Ni/Au	14/14/14/14/11/250 nm	Ohmic contact to n-substrate	e-beam evaporation	Bottom cell series resistance

3.5. Summary

An electrical and optical modelling approach was developed to design the optimum cell and terminal configurations of readily available solar cells for a mechanical stack. It was shown that, when resistive and optical losses are ignored, an AlGaAs/GaAs-InGaAs mechanically stacked solar cell had the highest performance of the triple-junction cell combinations considered. Furthermore this design requires the optimisation of only one cell-to-cell interface. While the assumptions used in this analysis result in an overestimation of MSSC performance, an AlGaAs/GaAs-InGaAs design was chosen as optimum for this study.

A comparative study of adhesives for bonding component cells in a mechanically stacked configuration was undertaken between PDMS, Polyimide and BCB. Polyimide has the highest refractive index and led to the highest modelled interface transmission with a PDMS interface resulting in the lowest interface transmission owing to its lower refractive index and absorption properties. BCB has the highest thermal conductivity of the adhesives considered and, when combined with the transmission losses, was found to be the most suitable adhesive for bonding cells for layer thicknesses of > 4 μm.

A 130 nm refractive index of 2.32 was found to be optimum for an anti-reflection coating between the cells and BCB layer and is to be provided by ZnS. A final GaAs-InGaAs mechanically stacked solar cell design specification was presented which is fabricated in later chapters.

3.6. References

[1] NREL, 'ASTM (G-173-03)', *http://rredc.nrel.gov/solar/spectra/am1.5/*. .

[2] S. Adachi, *Physical Properties of III–V Semiconductor Compounds*. John Wiley and Sons, 1992.

[3] S. M. Sze, *Physics of Semiconductor Devices*. John Wiley and Sons, 1981.

[4] M. R. Brozel and G. E. Stillman, *Properties of Gallium Arsenide*. INSPEC, 1996.

[5] P. Bhattacharya, *Properties of lattice-matched and strained Indium Gallium Arsenide*. INSPEC, 1993.

[6] C. Jacoboni, C. Canali, G. Ottaviani, and A. Alberigi Quaranta, 'A review of some charge transport properties of silicon', *Solid-State Electron.*, vol. 20, no. 2, pp. 77–89, Feb. 1977.

[7] R. J. Van Overstraeten and R. P. Mertens, 'Heavy doping effects in silicon', *Solid-State Electron.*, vol. 30, no. 11, pp. 1077–1087, Nov. 1987.

[8] M. S. Tyagi and R. Van Overstreten, 'Minority carrier recombination in heavily doped, *Solid-State Electron.*, vol. 26, pp. 557, 1983.

[9] H. A. Zarem, J. A. Lebens, K. B. Nordstrom, P. C. Sercel, S. Sanders, L. E. Eng, A. Yariv, and K. J. Vahala, 'Effect of Al mole fraction on carrier diffusion lengths and lifetimes in AlxGa1−xAs', *Appl. Phys. Lett.*, vol. 55, no. 25, pp. 2622–2624, Dec. 1989.

[10] J. Mouchart, 'Thin film optical coatings. 1. Optical coating stabilities', *Appl. Opt.*, vol. 16, no. 9, pp. 2486–2490, Sep. 1977.

[11] F. Niklaus, G. Stemme, J.-Q. Lu, and R. J. Gutmann, 'Adhesive wafer bonding', *J. Appl. Phys.*, vol. 99, no. 3, p. 031101, 2006.

[12] F. Niklaus, P. Enoksson, E. Kälvesten, and G. Stemme, 'Low-temperature full wafer adhesive bonding', *J. Micromechanics Microengineering*, vol. 11, no. 2, pp. 100–107, Mar. 2001.

[13] Dow Corning, 'BCB Optical Properties and Spectra', Dow Corning, 2012.

[14] T. Sameshima, J. Takenezawa, M. Hasumi, T. Koida, T. Kaneko, M. Karasawa, and M. Kondo, 'Multi Junction Solar Cells Stacked with Transparent and Conductive Adhesive', *Jpn. J. Appl. Phys.*, vol. 50, no. 5, p. 052301, 2011.

[15] 'Product Bulletin - PI2545 - Wet etch applications', HD Microsystems, Sep. 2009.

[16] J. Friend and L. Yeo, 'Fabrication of microfluidic devices using polydimethylsiloxane', *Biomicrofluidics*, vol. 4, no. 2, p. 026502, 2010.

[17] 'Dow Corning 184 Silicone Elastomer', Dow Corning, Product Information, Jan. 2010.

[18] S. P. Philipps, R. Hoheisel, T. Gandy, D. Stetter, M. Hermle, F. Dimroth, and A. W. Bett, 'An experimental and theoretical study on the temperature dependence of GaAs solar cells', in *2011 37th IEEE Photovoltaic Specialists Conference (PVSC)*, 2011, pp. 001610–001614.

[19] M. A. Green, K. Emery, Y. Hishikawa, W. Warta, and E. D. Dunlop, 'Solar cell efficiency tables (version 41)', *Prog. Photovoltaics Res. Appl.*, vol. 21, no. 1, pp. 1–11, 2013.

Chapter 4

InGaAs and InAlAs solar cell development

4.1. Introduction

Ternary and quaternary materials comprising alloys of In, Al, Ga, As and P grown lattice matched to InP provide access to bandgaps within 0.74 – 1.47 eV which can be used in multi-junction devices. Chapter 3 outlined the design of a III-V mechanically stacked solar cell featuring a narrow bandgap (0.74 eV at 300 K) $In_{0.53}Ga_{0.47}As$ bottom cell. This chapter uses the well understood optical and electrical properties of $In_{0.53}Ga_{0.47}As$ to design a cell that has an optimum spectral response in the 880 – 1700 nm wavelength range for sunlight transmitted through the GaAs. Subsequently the growth of a single-junction (1J) InGaAs cell structure, lattice matched to InP, and fabrication of devices is presented. Photovoltaic characterisation of these cells reveals a PV efficiency of 9.3% under 1-Sun conditions with a peak in EQE response of 93.8% at 1030 nm.

The second section of this chapter describes the design, growth and fabrication of single-junction $In_{0.52}Al_{0.48}As$ solar cells. $In_{0.52}Al_{0.48}As$ absorber layers can be used in solar cells lattice-matched to InP with a bandgap of 1.47 eV (at 300 K). This bandgap is similar to that of GaAs. The use of $In_xAl_{1-x}As$ as a photovoltaic material, however, has not been studied in detail. Electrical and photovoltaic characterization was carried out on these cells in order to better understand the material's properties and evaluate whether InAlAs is suitable for multi-junction cell use. Minority carrier diffusion lengths in the order of a few micrometres are extracted for InAlAs suggesting it is suitable for a wide bandgap cell in InP based multi-junction solar cells.

Given the cost and small diameter of commercially available InP wafers, the third section of this chapter trials the fabrication of $In_{0.53}Ga_{0.47}As$ and $In_{0.52}Al_{0.48}As$ solar cells on alternative substrates, namely GaAs. As a first demonstration the lattice constant of a GaAs substrate was graded to InP using an $In_xGa_{1-x}As$ metamorphic buffer layer onto which cells were grown. While GaAs substrates are also relatively costly this is the first demonstration of InAlAs cells on alternative substrates and the initial step towards realising InP based solar cells on Ge or Si substrates. The photovoltaic performance of these cells is compared with those on InP substrates in order to analyse the effectiveness of the grading layer. The solar cells on GaAs substrates were

found to have significantly reduced minority carrier diffusion lengths as compared to those on InP substrates attributed to defects generated in the grading layer which extend through to the junction region.

4.2. Cell 1: $In_{0.53}Ga_{0.47}As$ 1J solar cells

$In_{0.53}Ga_{0.47}As$ solar cells lattice matched to InP substrates are suitable as the lowest bandgap solar cells in a mechanical stack fabricated with GaAs or GaInP/GaAs top cells. An electrical and optical design was carried out to provide an optimum InGaAs cell response in the 880 – 1700 nm wavelength range for sunlight transmitted through GaAs. This section begins by describing the simulation and design of the emitter and base layers of an InGaAs solar cell. An optimum cell structure is detailed which was grown by MOVPE and fabricated into individual cells. Photovoltaic characterisation of these cells was carried out using a solar simulator and spectral response kit and the results of this analysis are presented.

4.2.1. Emitter and Base region design

The emitter and base regions are to be designed to provide optimum photocurrent and voltage responses for cells illuminated through a GaAs top cell i.e. for wavelengths > 880 nm. Lattice matched InP (*Eg* = 1.35 eV at 300 K) carrier blocking window and back surface field layers are to be included in the layer structure to reduce front and rear-surface recombination. As the bandgap of InP and GaAs are similar (1.35 and 1.41 eV respectively) the thickness of the InP window layer in the device has a minimal effect on the current generated by an $In_{0.53}Ga_{0.47}As$ cell stacked under a GaAs cell as it is only absorbing over a narrow wavelength range (880 - 920 nm). Figure 4.1 is a plot of the simulated light-generated photocurrent density for an InGaAs cell, as a function of InGaAs layer thickness, for the AM1.5d spectrum (888 W/m^2) as attenuated by a 5 μm thick GaAs layer (no reflection is considered). The expected photocurrent density is found using the Beer-Lambert law using the wavelength dependent absorption co-efficient of $In_{0.53}Ga_{0.47}As$ [1]. The attenuation of the incident spectrum by InP window layers of various thicknesses was also modelled where any absorption in the InP layer was considered a loss. The simulated photocurrent density in the cell drops by 0.35%, 0.8% and 3.4% for 40, 100 and 500 nm window layers respectively with an InGaAs absorbing layer thickness of 3 μm. As the window layer contributes to current spreading in the cell and reduces resistance, which increases

the Fill Factor of the cell, it was decided to use a relatively thick 100 nm InP window as the absorption losses are not substantial. An InGaAs base thickness of 3 μm was chosen as a suitable balance between absorption and MOCVD growth cost/time.

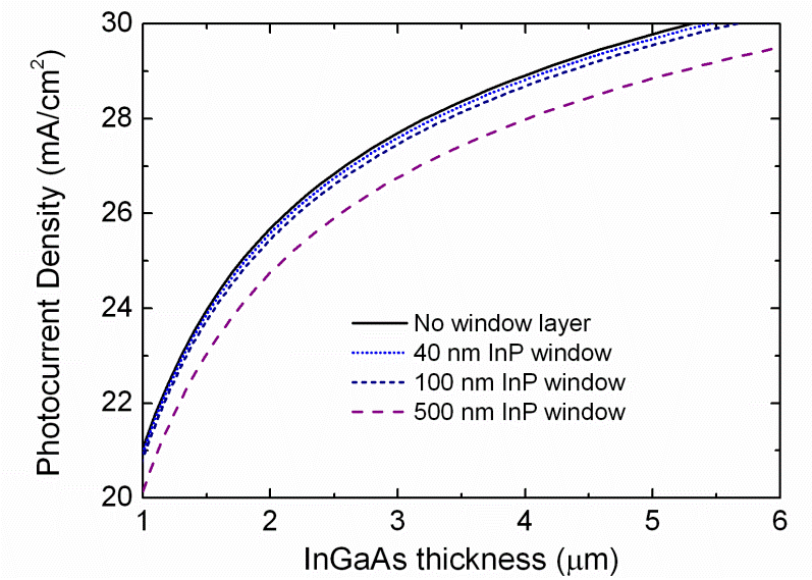


Figure 4.1: Simulated light-generated photocurrent density from an InGaAs solar cell under a GaAs based top cell as a function of InGaAs absorber layer and InP window thickness. Reflection was not considered at any interface.

The 1D solar cell modelling program PC1D (Appendix C) was used to simulate the electrical and photovoltaic characteristics of an InGaAs solar cell with a 3 μm base layer considering a p-type emitter layer and n-type base layer. The incident spectrum considered was AM1.5d with the power from any incident wavelength below 880 nm set to zero to replicate the solar spectrum transmitted through a GaAs-based top cell. This gives an available incident power density of 293 W/m^2. An overview of the typical simulation parameters used is given in Table 4.1.

Firstly the effect of emitter thickness and doping on device performance was simulated. Three emitter layer thicknesses were considered namely 50, 100 and 150 nm while the base doping level and thickness were fixed at $3x10^{17}$ cm^{-3} and 3 μm respectively. The highest simulated open-circuit voltage was achieved using a 50 nm emitter layer with a maximum of 381 mV for a doping level of $1.5x10^{18}$ cm^{-3} (Figure 4.2). A 100 nm emitter layer results in similar open-circuit voltages to a 50 nm layer for doping levels less than $1.5x10^{18}$ cm^{-3}.

Table 4.1: Overview of parameters of InGaAs cell used for simulation in PC1D.

Parameter	Value
Band gap (E_g)	0.74 eV
Intrinsic carrier concentration (300K)	6.3×10^{11} cm^{-3}
Dielectric constant	13.9
Max electron/hole mobility	12000/300 cm^2/Vs
Window doping, depth	1×10^{18} cm^{-3}, 100 nm
BSF doping, depth	1×10^{18} cm^{-3}, 40 nm
Front/Rear surface reflection	0%
Front-surface recomb.	100 cm/s
Rear-surface recomb.	100 cm/s
InP substrate doping	2×10^{17} cm^{-3} (n-type)

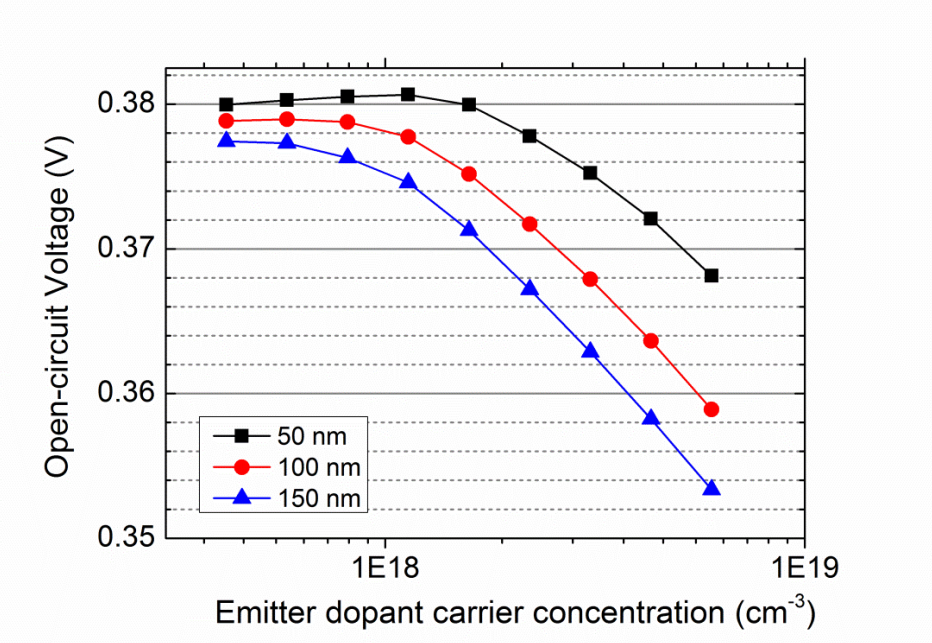


Figure 4.2: Simulated open-circuit voltage of a p-on-n InGaAs solar cell as a function of emitter doping level.

The open-circuit voltage of a p-on-n InGaAs solar cell as a function of the base doping level was simulated (Figure 4.3). As the doping level in the base is increased the open-circuit voltage decreases due to the reduction in diffusion length from 7.9 μm ($3x10^{17}$ cm^{-3}) to 5.9 μm ($9x10^{17}$ cm^{-3}). The effect of emitter thickness (p-type, $2x10^{18}$ cm^{-3}) on the open-circuit voltage is also shown. For the highly doped emitter it was found thinner layers are more suitable with a practical limit of 100 nm chosen for the InGaAs cell.

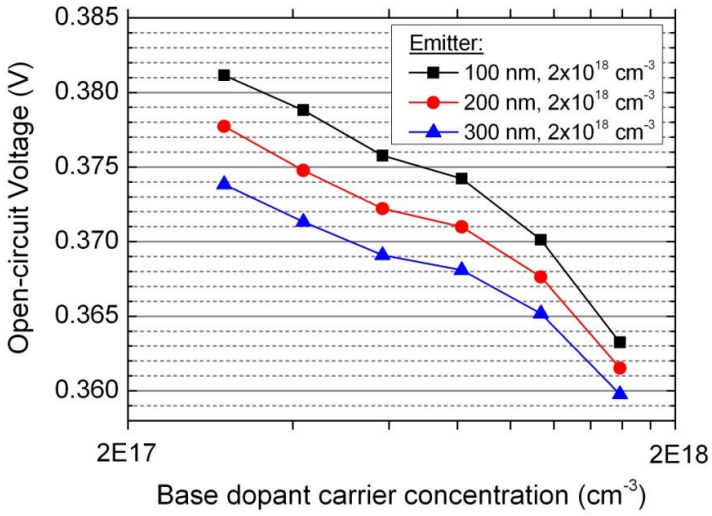


Figure 4.3: Simulated open-circuit voltage of a p-on-n InGaAs solar cell as a function of base doping level.

4.2.2. Optimised cell structure

The final cell design used in this thesis is summarised in Table 4.2. Firstly a highly doped n-type InP buffer layer is grown that also acts as the back-surface field. A 3100 nm thick $In_{0.53}Ga_{0.47}As$ absorbing region employing a 3000 nm thick n-type ($3x10^{17}$ cm^{-3}) base and a 100 nm thick p-type ($2x10^{18}$ cm^{-3}) emitter layer is provided. The 100 nm window layer is grown before a final layer of highly p-doped ($1x10^{19}$ cm^{-3}) $In_{0.53}Ga_{0.47}As$ cap layer to reduce the resistance of the front p-contact. This cell structure was grown using MOVPE by colleagues in the Tyndall National Institute.

Table 4.2: Nominal layer structure of the single-junction InGaAs cell grown by MOVPE.

Layer	Material	Doping cm^{-3}	Thickness μm
Cap	p^{++} $In_{0.53}Ga_{0.47}As$	$1x10^{19}$	0.25
Window	p^{+} InP	$2x10^{18}$	0.1
Emitter	p^{+} $In_{0.53}Ga_{0.47}As$	$2x10^{18}$	0.1
Base	n^{+} $In_{0.53}Ga_{0.47}As$	$3x10^{17}$	3
BSF/Buffer	n^{++} InP	$1x10^{19}$	0.5
Substrate	n-InP	$1\text{-}4x10^{18}$	350

4.2.3. Cell Processing

5 mm x 5 mm InGaAs solar cells (Metal grid coverage = 9.8%) were fabricated using standard photolithographic techniques (Figure 4.4). A p-contact (Ti/Pt/Au, 30/50/200 nm) front surface grid pattern and back-side blanket metalisation n-contact (Au/Ge/Au/Ni/Au, 14/14/14/11/250 nm) were deposited by e-beam evaporation. The metals were annealed in forming gas (1.5 sccm - 5% H_2:95% N_2) at 420°C for 5 minutes to reduce contact resistivity. A H_3PO_4:H_2O_2:H_2O wet etch, selective over InP, was used to remove the absorbing $In_{0.53}Ga_{0.47}As$ cap layer in the window region. Inductively Coupled Plasma (ICP) etching with $Cl_2/CH_4/H_2$ was used to isolate the devices [2]. A 140 nm thick film of SiN was deposited on the front surface of the cells to provide a single-layer anti-reflection coating and to passivate the mesa sidewalls. The SiN layer was opened over the contact busbars by CF_4 plasma etching to allow electrical probing of the cells.

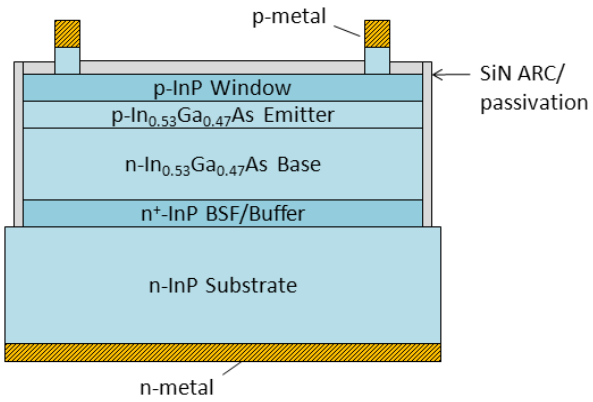


Figure 4.4: Outline of the as processed InGaAs solar cell with the SiN ARC/passivation layer highlighted.

4.2.4. Photovoltaic characterisation

Following design and fabrication of individual cells, the PV characteristics of the cells were analysed. The *photocurrent density-voltage* of an InGaAs cell measured in a solar simulator (Appendix A) for 1-Sun conditions (AM1.5G, 0.1 W/cm^2) is given in Figure 4.5 and summarised in Table 4.3. The measured open-circuit voltage of the solar cells under 1-Sun conditions was 0.352 V. The low short-circuit current density of 38.2 mA/cm^2 is due to parasitic absorption in the 100 nm thick InP window layer and the design of the anti-reflection coating for IR photon transmission. Nevertheless a 1-sun efficiency of 9.3% was achieved with a 69% Fill Factor.

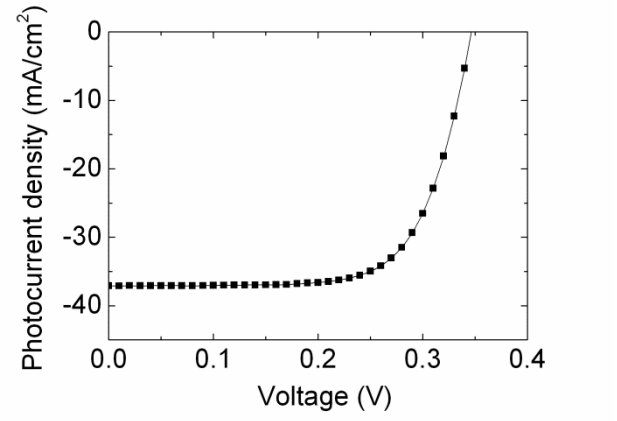


Figure 4.5: Measured *photocurrent density-voltage* characteristics of InGaAs solar cells under 1-Sun conditions.

This result compares well to the state of the art [3] on p-on-n InGaAs solar cells where the maximum efficiency they achieved was 9.4% under the AM1.5G spectrum (0.1 W/cm^2). Their cell structure achieved a lower open-circuit voltage of 330 mV but a higher short-circuit current density of 44 mA/cm^2 due to the use of a 50 nm InP window layer. The same group's work with n-on-p structures has led to efficiencies of 12.1% under 1-Sun conditions as measured by the Japanese Quality Assurance Organisation (JQA) owing to the open-circuit voltage of 0.4002 V achieved by the cell design [4].

Table 4.3: Measured PV performance of single-junction InGaAs solar cells under 1-Sun (AM1.5G) conditions.

	Polarity	**InGaAs absorbing layer thick.**	**Voc**	**Jsc**	**FF**	**Efficiency**
		μm	mV	mA/cm^2	%	%
This work	p-on-n	3.1	352	38.2	69	9.3
Matsubaru *et al.* ('98)	p-on-n	3.5	330	44	66	9.4
Yamada *et al.* ('05)	n-on-p	3.4	400	45.14	66.9	12.1

The measured EQE of the cells (Figure 4.6) shows the low short-circuit current density value is due to the design of the cell to give a large response in the 880 – 1700 nm range. The single-layer SiN_x (140 nm) anti-reflection coating was optimised for IR photon transmission with a design minimum at 1000 nm. The reflection from the front surface of the cell was measured as less than 10% between 890 – 1700 nm but up to 30% between 460 and 700 nm. Furthermore the expected absorption in the thick 100 nm InP window layer is shown. The expected EQE of the InGaAs cell design was simulated using the theory described in Chapter 1. The expected diffusion lengths of 15.3 and 7.9 μm in the emitter and base regions respectively gave good agreement with the measured data (Figure 4.6) when combined with a front and rear surface recombination value of 1x10^4 cm/s.

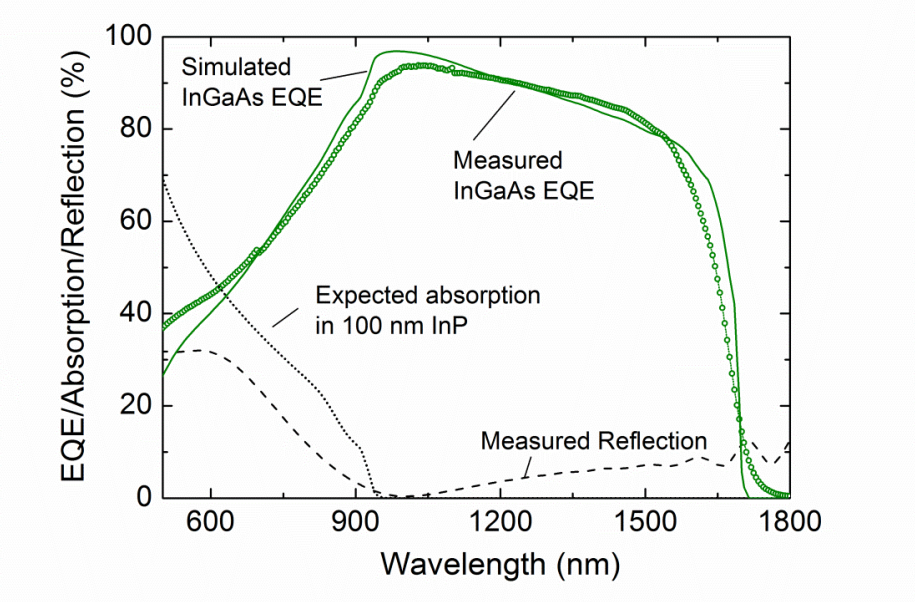


Figure 4.6: Measured EQE of the stand-alone InGaAs solar cell as well as the measured reflection from the front surface and the simulated absorption of the AM1.5G spectrum in a 100 nm InP layer.

4.3. Cell 2: $In_{0.52}Al_{0.48}As$ 1J solar cell

$In_{0.52}Al_{0.48}As$ grown lattice matched to InP is a direct bandgap material of 1.47 eV at 300 K and is the widest direct bandgap binary or ternary III-V material that can be grown lattice matched to InP. It is of interest to the photovoltaic community as it provides an alternative to the well established GaAs solar cell but at an alternative lattice constant, although InAlAs is not well understood as a photovoltaic material. As material properties such as minority carrier diffusion length, expected surface recombination and minority carrier mobility are not readily available for this material, the following section outlines the fabrication of single-junction $In_{0.52}Al_{0.48}As$ solar cells which were analysed to probe the material's photovoltaic characteristics and gauge its suitability for use in multi-junction cells based on alternative lattice parameters to that of GaAs. The following section describes the cell structure and fabrication followed by PV, electrical and material characterisation used to draw conclusions on the suitability of InAlAs for multi-junction solar cells.

4.3.1. InAlAs cell structure

An $In_{0.52}Al_{0.48}As$ single-junction solar cell was grown by MOCVD with a layer structure as outlined in Table 4.4 and as follows: firstly, an InP buffer layer was grown and this was followed by an 800 nm thick absorbing region employing a 500 nm $In_{0.52}Al_{0.48}As$ n-type ($4x10^{17}$ cm^{-3}) base layer and 300 nm p-type ($3x10^{18}$ cm^{-3}) emitter layer. The emitter and base doping levels were chosen as typical for p-on-n III-V solar cells. A thin (20 nm) p-type ($1x10^{18}$ cm^{-3}) wide-bandgap (1.85 eV) $In_{0.35}Al_{0.65}As$ window layer was then grown as an electron blocking front-surface field window layer which also introduces strain into the device owing to this materials smaller lattice constant than the rest of the III-V materials used. This has been previously shown to reduce surface recombination velocity in single-junction $In_{0.52}Al_{0.48}As$ solar cells while maintaining high photocurrents as the thin layer of wider bandgap material results in low parasitic absorption [5]. Figure 4.7 is a TEM image of this 20 nm layer and shows no defects. Finally a highly p-doped ($2x10^{19}$ cm^{-3}) lattice-matched $In_{0.53}Ga_{0.47}As$ cap layer was grown to reduce the resistance of the front p-contact.

Table 4.4: Layer structure of the single-junction InGaAs cell grown by MOVPE.

Layer	Material	Doping cm^{-3}	Thickness µm
Cap	p^{++} $In_{0.53}Ga_{0.47}As$	$1x10^{19}$	0.2
Window	p^{+} $In_{0.35}Al_{0.65}As$	$1x10^{18}$	0.02
Emitter	p^{+} $In_{0.52}Al_{0.48}As$	$3x10^{18}$	0.3
Base	n^{+} $In_{0.52Al0.48}As$	$4x10^{17}$	0.5
BSF/Buffer	n^{+} InP	$5x10^{18}$	2
Substrate	n-InP	$1\text{-}4x10^{18}$	350

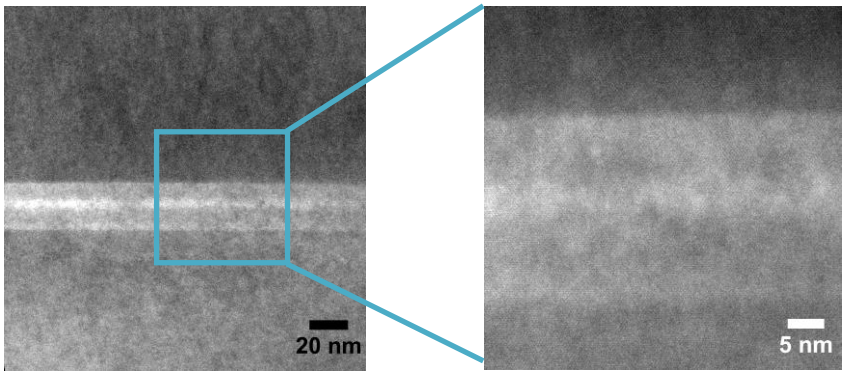


Figure 4.7: Cross-sectional TEM image of the strained $In_{0.35}Al_{0.65}As$ window layer. No defects are visible.

4.3.2. Cell Processing

Circular mesa diodes (Diameter = 1 mm, Metal grid coverage = 48%) were fabricated with Ti/Pt/Au (30/50/300 nm) p-metal front contacts and Au/Ge/Au/Ni/Au (14/14/14/50/250 nm) blanket n-metalisation on the back surface both deposited by e-beam evaporation (Figure 4.8). The metal contacts were annealed simultaneously in a furnace at 420°C for 5 minutes in 5% H_2/N_2 (1.5 sccm) forming gas. A H_3PO_4:H_2O_2:H_2O (1:1:38, etch rate: 110 nm/min) InGaAs and InAlAs wet etch was used to isolate the mesa devices, stopping selectively on the InP buffer

layer. (Note: Solar cells were also fabricated using Inductively Couple Plasma (ICP) etching with the same $Cl_2/CH_4/H_2$ recipe previously used to isolate InGaAs cells. These devices, however, had much poorer electrical characteristics than those isolated by wet etching. This fabrication method, however, should not be discounted as an optimisation of the etch recipe may lead to comparable or better electrical characteristics). A $C_6H_8O_7$:H_2O_2 (2:1, etch rate: 200 nm/min) wet etch which selectively etches $In_{0.53}Ga_{0.47}As$ over $In_{0.35}Al_{0.65}As$ was used to remove the absorbing cap layer in the open regions of the diodes. A 70 nm thick film of SiN_x was deposited by Plasma Enhanced Chemical Vapour Deposition on the front surface of the cells to provide a single-layer anti-reflection coating. The SiN_x layer was opened over the contact busbars using a CF_4 dry etch to allow electrical probing of the cells.

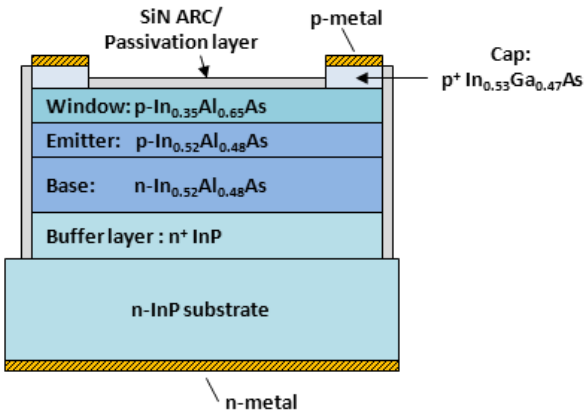


Figure 4.8: Outline of the as processed InAlAs single-junction solar cells.

4.3.3. Photovoltaic characterisation

The *photocurrent density-voltage* characteristics of the cells under 1-Sun conditions were measured (Figure 4.9) in a solar simulator (Appendix A) in order to derive the photovoltaic properties of the cells. The cells achieved an open-circuit voltage of 925 mV, a Fill Factor of 79%, a short-circuit current density of 9.1 mA/cm^2, leading to a photovoltaic conversion efficiency of 6.6%. The low photocurrent response is due to the 48% shading loss but this suggests that with no shading, 18 mA/cm^2 is possible with only 800 nm thick absorber layers leading to a potential cell efficiency of ~ 13%. Furthermore the measured open-circuit voltage is indicative of a high quality solar cell and proves the suitability of the material for photovoltaics. Despite this being only the second InAlAs cell reported worldwide the difference between the

measured open-circuit voltage and the materials bandgap is 545 mV where a difference of 400 mV is indicative of a very high quality solar cell [6].

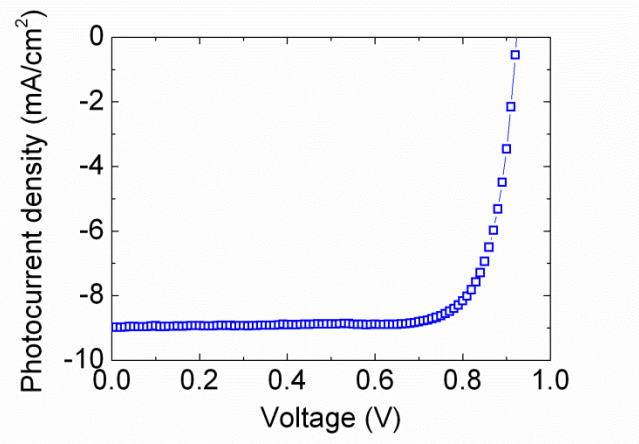


Figure 4.9: Measured photocurrent density-voltage characteristics of InAlAs solar cells under 1-Sun (AM1.5G) conditions.

4.3.4. Electrical and material characterisation

A key motivation for InAlAs cell fabrication is to derive material properties of these cells relevant to photovoltaic operation so that an optimisation process can be completed and cell performance improved. Three methods were utilised to estimate minority carrier mobility, diffusivity, lifetime and diffusion length values for the cells. Firstly, Hall majority carrier mobility values were measured and a conversion process used to extract minority carrier values. Secondly, the forward biased *dark current density – voltage* (DJV) characteristics of the diodes were measured in order to investigate the recombination characteristics of the cells and estimate carrier lifetime values. Finally, the measured EQE was fitted in order to derive carrier transport properties i.e. the diffusion lengths in p-type and n-type $In_{0.52}Al_{0.48}As$.

Carrier mobility

The Hall majority carrier mobility of n-doped ($3.7x10^{17}$ cm^{-3}) and p-doped ($2.4x10^{18}$ cm^{-3}) $In_{0.52}Al_{0.48}As$ layers (grown separately as single layers on semi-insulating InP substrates) were measured at 300 K as 1410 cm^2/Vs and 39 cm^2/Vs respectively in a Hall measurement set-up. From this data, majority carrier diffusion co-efficients, $D = \mu kT/q$, of 36 and 1 cm^2/s were obtained for the n-type and p-type layers respectively. In order to calculate the diffusion constant

of minority carriers in each layer an assumption must be made for the ratio of effective masses for electrons and holes in $In_{0.52}Al_{0.48}As$. We then note that the diffusion coefficient is proportional to *1/m, m* being the effective mass of the relevant carrier. This comes because $D = v.L$ (v = thermal velocity, L = diffusion length) and $L = v\tau$, τ being the carrier lifetime and thus $D = v^2\tau$. As the thermal *energy* = $mv^2/2$ results in $D \propto 1/m$. An estimate of the ratio of the effective mass of the electrons to holes is 0.1 based on the literature for $In_{0.52}Al_{0.48}As$ [7]. We note that a similar ratio of diffusion coefficients is used for GaAs materials [8]. Therefore the minority electron and hole diffusion coefficients are estimated to be 10.1 cm^2/s and 3.6 cm^2/s at these doping levels.

Minority carrier lifetime

The *DJV* characteristics of the cells were measured and the ideality as a function of voltage extracted (Figure 4.10). Chapter 1 outlined the double-diode equation used to describe solar cells in the dark. As discussed previously the reverse saturation current of a p-n junction consists of two components, a diffusion and quasi-neutral region component, J_{01}, which dominates at high biases and a depletion region recombination component, J_{02}, which dominates at low biases with an ideality, n, of ~2 . Two lines were fitted to the measured data to extract J_{o1} and J_{o2} (Figure 4.10) which were found to be $2x10^{-12}$ A/cm^2 and $1x10^{-10}$ A/cm^2 respectively.

From the measured data, at higher current levels, a stronger contribution is seen from the J_{o1} term as the slope of the measured DJV increases i.e. the ideality decreases. As the ideality is ~2 at higher biases, an upper bound to the open-circuit voltage achievable in this cell is found by calculating V_{oc} assuming recombination is dependent only on the J_{o2} component and neglecting the diffusion current (Equation 4.1). For $J_{o2} = 1x10^{-10}$ A/cm^{-2}, V_{oc} is calculated as 948 mV and is only 23 mV greater than the measured V_{oc} confirming the small contribution seen from the additional current components. As the photocurrent density of the cell is increased through using thicker layers the V_{oc} should increase significantly and compare well to those found in GaAs cells.

$$V_{oc} = \frac{2kT}{q} \ln\left(\frac{J_{sc}}{J_{o2}}\right) \qquad (4.1)$$

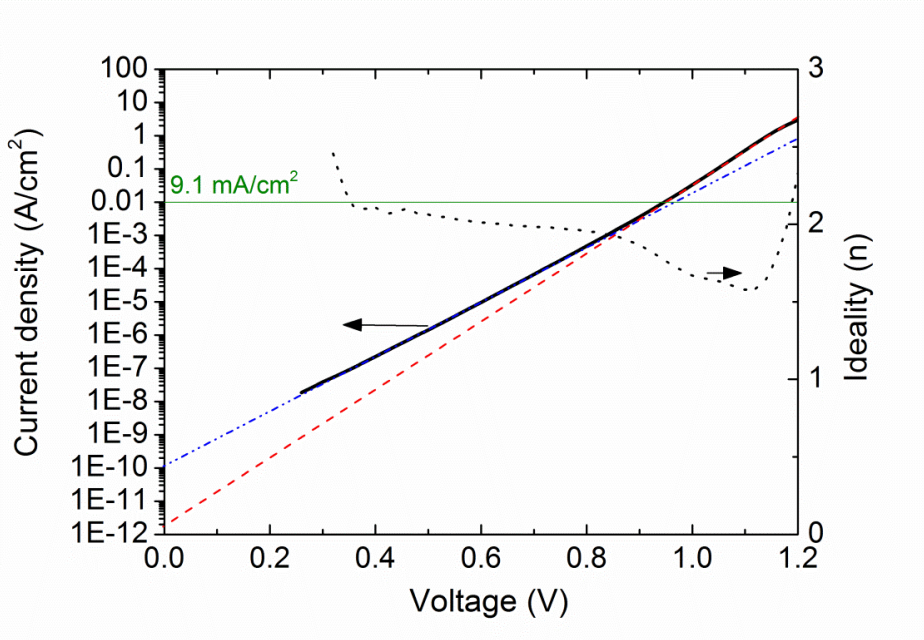


Figure 4.10: Measured *dark current density-voltage* of InAlAs solar cells at 20 ^{o}C (black line) and the extracted ideality (black dashed line) as a function of voltage. The straight lines fitted to the J_{o1} and J_{o2} dominated regions are shown as red and blue dashed lines respectively.

The value of J_{o2} allows an estimation to be made for the carrier lifetime in the junction region. The depletion region recombination is described using Equation 4.2 [9], where, $n_i(T)$, is the temperature dependent intrinsic carrier concentration, W_d, is the depletion width at zero bias (Equation 4.3) and, $\tau(T)$, is the carrier lifetime in the depletion region i.e. $\tau(T)$ is the only unknown.

$$J_{o2} = \frac{qn_i(T)W_d}{2\tau(T)} \tag{4.2}$$

$$W_d = \sqrt{\frac{2\varepsilon}{q}V_o\left(\frac{1}{N_A}+\frac{1}{N_d}\right)} \qquad where\ V_o = \frac{kT}{q}ln\left(\frac{N_A N_D}{n_i^2}\right) \tag{4.3}$$

As the effective masses of electrons and holes [7] and the bandgap of $In_{0.52}Al_{0.48}As$ are similar to GaAs, an intrinsic carrier concentration, n_i, of $2x10^6$ cm^{-3} at 300 K was assumed. A static depletion region width, W_d, of 76 nm was found using Equation 4.3 (assuming uniform doping

with: p-type doping, N_A, of $2x10^{18}$ cm^{-3} and n-type doping, N_D, of $3x10^{17}$ cm^{-}) assuming the static dielectric constant value, ε, of 11.48 calculated by Bouarissa and Boucenna [10]. Using this value calculated for W_d and the measured value for J_{o2} at 300K (the point where the dashed blue line of Figure 4.10 crosses the y-axis), Equation 4.2 was used to calculate a τ value of 12 ns for the carrier lifetime in the InAlAs diodes. It should be noted that carrier lifetime is typically given as a function of doping level in a semiconductor material. As this analysis used measured data from a p-n junction, the exact lifetime as a function of doping level is not possible. The value derived represents the lifetime in the depletion region where the carrier concentration is typically assumed zero. A more systematic approach to determining the lifetime in InAlAs materials would involve the growth of numerous samples of single layers of p or n doped InAlAs on semi-insulating InP substrates. Hall mobility measurements could be used to determine the carrier concentration in the layers and time-resolved photoluminescence could be used to measure lifetime. Nevertheless the value of 12 ns measured is a significant result indicating the quality of the material which compares well to values expected for p-type and n-type GaAs of similar doping levels [11].

Carrier transport properties

The measured cell EQE is presented in Figure 4.11 as well as the measured front surface reflection. The derived minority hole and electron diffusion co-efficients, *D*, the expected $In_{0.52}Al_{0.48}As$ absorption taken from an ellipsometric database and the measured reflection were used to simulate the EQE response. The remaining parameters required to complete the EQE simulation were the diffusion length and carrier lifetime in the emitter region as well as the front and rear surface recombination velocities which are summarised in Table 4.5.

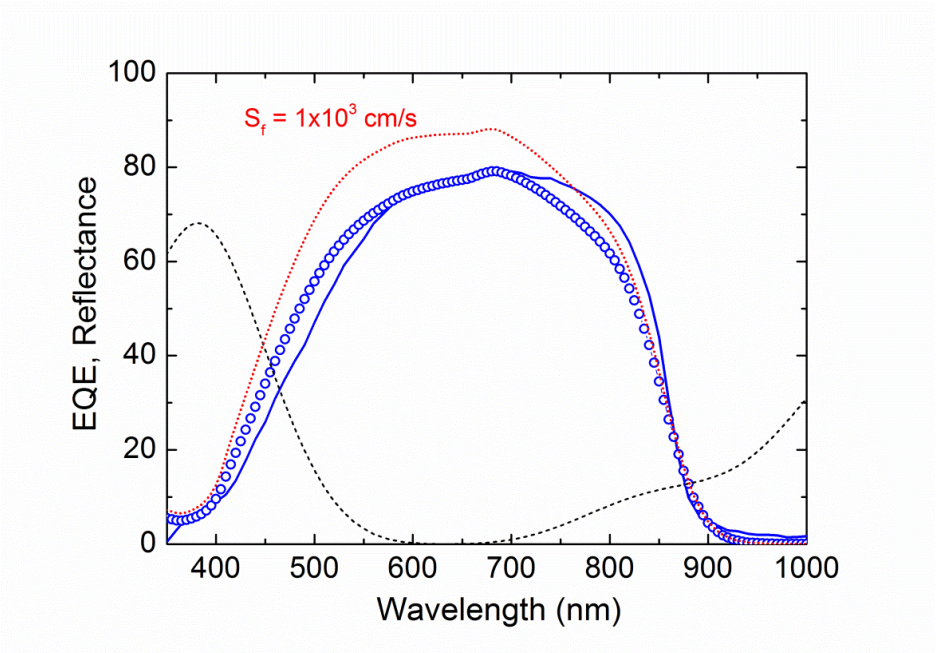


Figure 4.11: Measured External Quantum Efficiency (blue circles) and front-surface reflection (dashed black line) as measured for the InAlAs solar cells. The *best-fit* and *low front-surface recombination* simulated responses are given as a blue line and dotted red line respectively.

The fitted emitter and base region diffusion lengths in the simulated EQE (Figure 4.11) are 0.71 μm and 2.08 μm. While the surface recombination velocity of the rear surface was simulated as $1x10^3$ cm/s, a greater recombination velocity at the front surface of the device, $2x10^4$ cm/s, was simulated despite the use of the wide-bandgap window blocking layer. This may be due to the window layer not being thick enough to provide adequate carrier blocking or the Al in the window layer may have oxidised before the deposition of the passivating SiN layer or additionally the layer may have been partially etched during the cap etch process. Also shown is the simulated EQE if the front surface recombination was decreased to $1x10^3$ cm/s where the maximum EQE of the cell would increase to 90%. There are many unknowns with the use of a thin, strained and high Al content layer for the front surface field. Further analysis and characterisation of window layers for InAlAs cells is recommended to reduce the front surface recombination.

It is worth noting the minority carrier diffusion lengths extracted for the emitter (p-type, $3x10^{18}$ cm^{-2}) and base (n-type, $4x10^{17}$ cm^{-2}) regions of the InAlAs cells of 0.71 μm and 2.08 μm respectively are shorter than those for GaAs of 14 μm and 5 μm respectively for the same doping levels. [11].

Table 4.5: Carrier transport parameters derived and fitted for the InAlAs solar cells.

Parameters extracted from hall measurements	**Units**	**p-emitter**	**n-base**
Minority carrier diffusion coefficient	cm^2/s	10.1	3.6
Parameters extracted from EQE fit			
Diffusion length	nm	710	2080
Minority carrier lifetime	ns	0.5	12
Surface recombination	cm/s	$2x10^4$	$1x10^3$

InAlAs cell recommendations

InAlAs solar cells provide an alternative to the well established GaAs solar cells although additional research is recommended on the following topics. The V_{oc} measured for these first cells was 925 mV under 1-sun conditions which indicates the high quality of the material. It is recommended to measure the transport properties such as minority carrier diffusion length, mobility and carrier lifetime as a function of doping level and polarity in order to enable a comprehensive cell optimisation. Furthermore, a significant loss in carrier extraction is caused by recombination at the front surface of the cell, as indicated by the EQE measurements at shorter wavelengths. This recombination may be reduced by ensuring adequate carrier blocking by the high Al content window layer. SIMS analysis is recommended to measure the actual Al content of this layer as grown. Furthermore simulations on the bandgap difference between the emitter and window layer would provide some insight into the recombination rates possible as a function of Al content. While these recommendations may improve the performance of single-junction InAlAs solar cells it is clear the material provides an alternative to GaAs cells with a 1-sun efficiency of 6.6% measured with 800 nm absorbing layers and 48% cell shading. The next iteration on the current cell design should utilise thicker absorbing layers and reduced cell shading to improve the photocurrent extracted from the device.

4.4. Advanced substrate engineering

The use of InP based solar cells provides access to a wide direct bandgap range between 0.74 – 1.47 eV for multi-junction solar cells. InP substrates, however, are more expensive and brittle than other semiconductor substrates such as GaAs, Ge or Si. Furthermore large substrate diameters, of high quality semiconductor material, are more readily available for the other material types. The integration of InP based solar cells on alternative substrates is desirable to combine the advantages of solar cells at this lattice parameter with a more commercially viable substrate material. As a first step towards realising these cells on alternative substrates to InP, $In_{0.53}Ga_{0.47}As$ and $In_{0.52}Al_{0.48}As$ solar cells were grown and fabricated on GaAs substrates. An $In_xGa_{1-x}As$/InP metamorphic grading layer was used to alter the lattice constant of the host substrate from 5.65 Å to 5.87 Å. Cells were fabricated on this buffer layer with the same structure as used previously in this chapter to allow direct performance comparison. While GaAs substrates are also relatively costly this is the first demonstration of InAlAs cells on alternative substrates and the initial step towards realising InP based solar cells on Ge or Si substrates

4.4.1. MOVPE growth of metamorphic buffer layers

The development and growth of the metamorphic buffer layer (MBL) was carried out by colleagues in the Epitaxy and Physics of Nanostructures group at the Tyndall National Institute. The $In_xGa_{1-x}As$-InP MBL was grown on a perfectly oriented (100) GaAs wafer by Metal Organic Vapour Phase Epitaxy (MOVPE) in an Aixtron 200 MOVPE reactor. The growth was performed with standard hydride and metalorganic trimethyl-III sources, at 80 mbar, with nitrogen as carrier gas, disilane and di-ethyl zinc as doping sources. The substrate temperature, as confirmed by an optical pyrometer, was set at 650 °C during the growth of GaAs and decreased with increasing In inclusion in the graded structure to 620 °C for the InP cap layer. The grading of the GaAs lattice constant to that of InP was performed over a thickness of 1 μm, by growing $In_xGa_{1-x}As$ up to a value of x=53% indium using one parabolic [12] and two linear grading regions, as illustrated in Figure 4.12, in a similar way to that reported for grading from InP to InAs [13], although without employing surfactants effects.

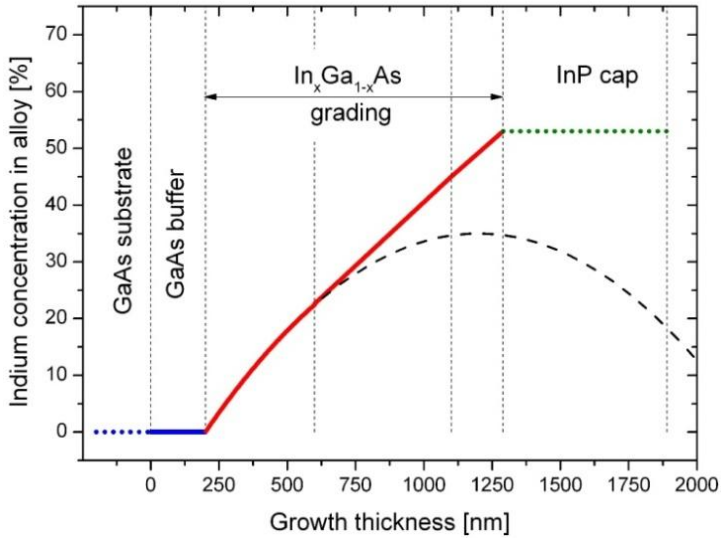


Figure 4.12: Overview of the metamorphic buffer layer growth profile. The homoepitaxial buffer GaAs layer is followed by alloys of a continuous convex compositional gradient of the In content from x = 0 % to 53 %. The grading comprises of three sections: first 400 nm along a parabolic curve, then linearly, with the slope of the curve reduced for the final 190 nm. The structure is capped with an InP layer, grown under the best growth conditions as established in [14].

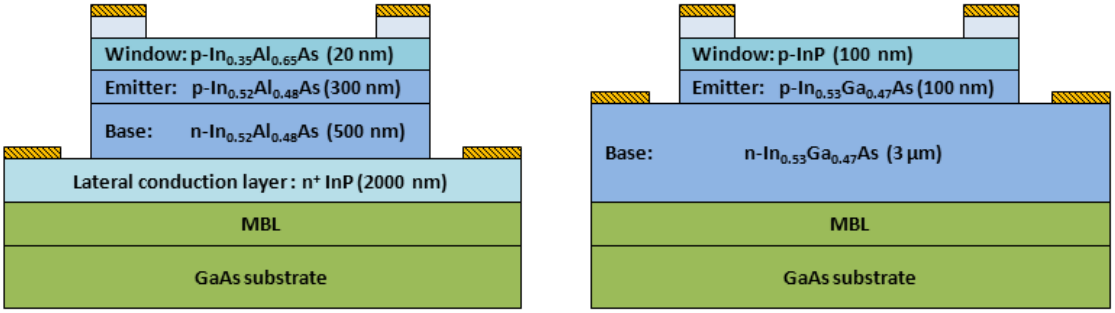
4.4.2. Fabrication of $In_{0.52}Al_{0.48}As$ and $In_{0.53}Ga_{0.47}As$ solar cells on GaAs substrates

The growth of the photovoltaic layers was carried out in a second stage on the MBL. The structures follow those previously outlined in Tables 4.2 & 4.4. Cell fabrication is described below.

InAlAs cell fabrication on GaAs substrates

InAlAs solar cells were grown on the MBL using thick absorbing layers where the 2 μm highly doped InP buffer layer acts as a lateral conductor and n-contact as the MBL is nominally un-doped. InAlAs Solar cells (Area = 0.63 mm^2, Metal grid coverage = 24%) were fabricated with Ti/Pt/Au (30/50/200 nm) p-metal front contacts. A H_3PO_4:H_2O_2:H_2O (1:1:38, etch rate: 110 nm/min) InGaAs (cap) and InAlAs (absorbing layers) wet etch was used to make a mesa and open regions for n-type contacting as the wet etch stopped selectively on the InP lateral conduction layer. n-type contacts (Au/Ge/Au/Ni/Au, 14/14/14/11/250 nm) were deposited in the open

regions using standard lift-off lithography as outlined in Figure 4.13 (a). The remaining InAlAs processing followed that outlined previously.



(a) (b)

Figure 4.13: Outline of the (a) InAlAs and (b) InGaAs solar cells structures grown by MOVPE on MBL-GaAs substrates.

InGaAs cell fabrication on GaAs substrates

n-type contacts to the InGaAs cells were formed by dry etching (Cl_2:CH_4:H_2) to the base region of the device and depositing Au/Ge/Au/Ni/Au (14/14/14/11/250 nm) in the exposed regions using standard lift-off lithography (Figure 4.13 (b)). As the exposed InGaAs sidewall is sensitive to high temperature processing steps it was decided to contact the base region of the device, as opposed to the InP back surface field layer, in order to reduce the sidewall area exposed to the 420^{o}C thermal anneal carried out post metal deposition. By contacting the base region of the device it was not possible to provide a back surface field which may result in reduced collection of carriers near the back surface of the device. The cell area was 7.84 mm^2 with a p- and n-metal coverage on the front surface of 10.8%. The remaining InGaAs processing followed that outlined in Section 4.2.3.

4.4.3. Material characterisation

The first characteristaion step undertaken on these cells was high resolution imaging of the cell and MBL structures to investigate the presence of defects. TEM images were taken on an InAlAs/MBL/GaAs sample using Tyndall National Institute facilities where micro-structural

analysis was performed using HR-TEM (Jeol 2100 transmission electron microscope; 200 kV; double tilt holder) in conjunction with selected area electron diffraction (SAED) analysis [Note that normally ~10% error should be accounted for due to the electron optics of the instrumentation]. Images were taken on a single sample and therefore a statistical analysis of the defects present was not possible.

Figure 4.14 shows a cross-sectional TEM image of the MBL structure illustrating the initially highly defective region near the GaAs surface (A1). The various grading layers are visible in the image and the defective region appears to be mostly limited to the first (parabolic grading) layer, labelled A2, where strain effects are greatest. In general, defects are seen to propagate laterally in this first graded layer rather than threading vertically towards the upper layers of the MBL where they would impact on the quality of the solar cell structure. Nevertheless, some defects are still visible in the InP capping layer (A5) at the surface of the MBL, which may lead to structural defects in the solar cell layers.

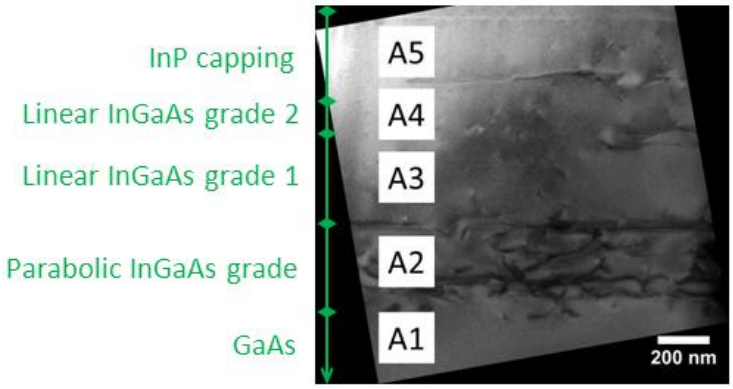


Figure 4.14: Cross-sectional bright field TEM image of the MBL of the solar cell structure.

Figure 4.15 is a lower magnification TEM image of the complete InAlAs solar cell and MBL epitaxial structure grown by MOVPE. High resolution images are not possible at this magnification so the grain structure visible is not real; the image was, however, used to confirm layer thicknesses. High resolution images of each region of the structure were taken and are given as a 'stitched image'. The defects visible in the MBL structure (B1) are seen to not be confined to the graded layers. Defects extend through the 2 μm InP capping and buffer layers (B2 & B3) to the active InAlAs photovoltaic region (B4).

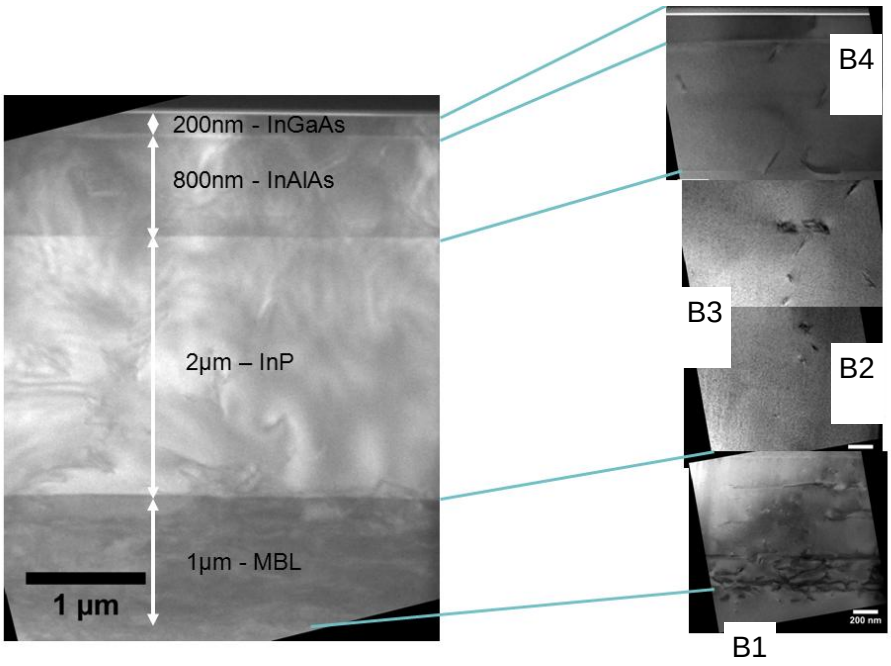


Figure 4.15: Cross-sectional bright field TEM image of the complete MBL and InAlAs photoactive region. Only partial focus was achieved at low magnification with the 'grain' structure visible not real; but a clear delineation of each material layer obvious. Higher magnification stitched-images show the permeation of defects through the complete epitaxially grown structure.

4.4.4. Photovoltaic characterisation of cells on the MBL

To characterize the effect of the defects revealed by TEM imaging; the photovoltaic performance and spectral response of the cells were measured. The InAlAs cells on the MBL substrate, with a metal shading of 24%, produced a short-circuit current density of 9.3 mA/cm^2, an open-circuit voltage of 724 mV and a 1-Sun efficiency of 5% while maintaining a high Fill Factor of 75% (Figure 4.16).

The lower bandgap InGaAs cells had a higher short-circuit current density of 28.3 mA/cm^2 (10% metal shading). An open-circuit voltage of 284 mV was achieved which with a Fill Factor of 56.1% gave a 1-Sun PV conversion efficiency of 4.5% (Figure 4.17).

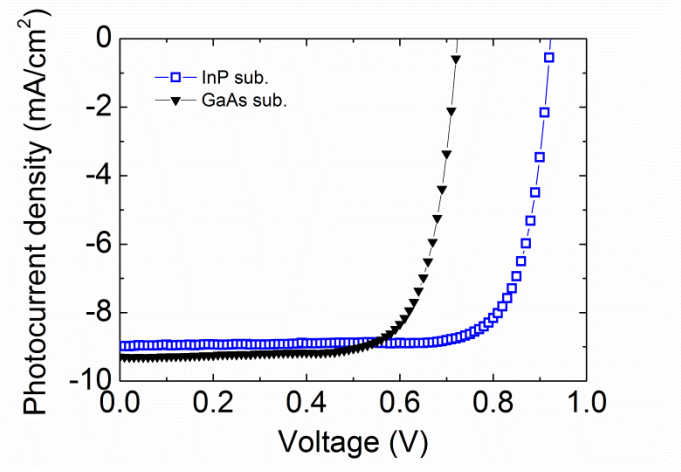


Figure 4.16: Measured photocurrent density-voltage characteristics of InAlAs solar cells on InP and GaAs substrates under 1-Sun conditions.

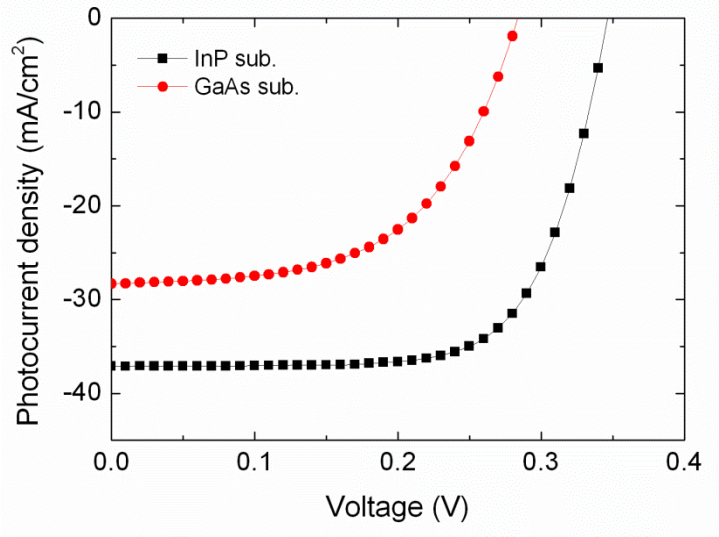


Figure 4.17: Measured photocurrent density-voltage characteristics of InGaAs solar cells on InP and GaAs substrates under 1-Sun conditions.

4.4.5. Spectral response of cells on the MBL

The defects in the photoactive region of the devices on the MBL substrate, identified by TEM images, reduce the open-circuit voltages and photocurrent densities as compared to cells grown lattice-matched to InP (Table 4.6). This implies increased recombination rates and reduced diffusion lengths. In order to analyse the drop in performance of InAlAs and InGaAs solar cells due to the MBL; the EQE of these cells was measured and fitted (Figure 4.18). During the fitting

process the diffusion length, carrier lifetime and front and rear surface recombination were changed with the diffusion constant, the intrinsic carrier concentration and the dielectric constant assumed unaltered by the increase in defects.

InAlAs cells

Significantly decreased diffusion lengths of 180 nm and 210 nm were fitted for the emitter and base regions of the devices respectively as compared to cells on an n-InP substrate where values of 710 nm and 2080 nm were fitted. The modelled front surface recombination velocity increased on MBL substrates from $2x10^4$ cm/s to $8x10^4$ cm/s with the relatively low rear-surface value of $1x10^3$ cm/s unchanged. The defects cause significantly reduced diffusion lengths through increased recombination rates while the increase in the front surface recombination signifies these defects extend completely through the device only terminating at the front surface.

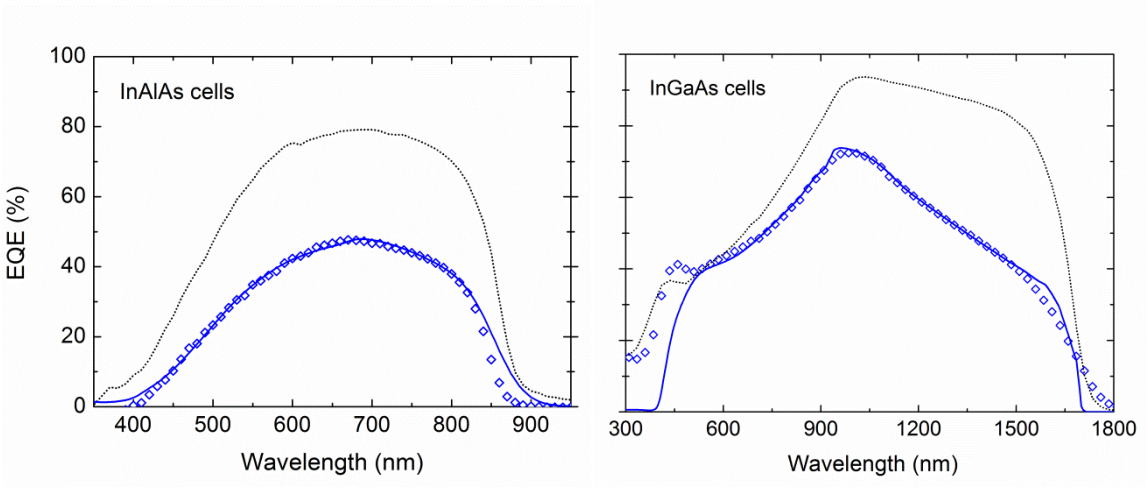


Figure 4.18: External Quantum Efficiency as measured for both the InAlAs and InGaAs solar cells grown on GaAs (blue diamonds) and InP substrates (dotted line). The simulated response for cells on a GaAs substrate is given as a solid blue line.

InGaAs cells

As shown in Figure 4.18 the measured EQE of InGaAs cells on the MBL are significantly reduced when compared to those lattice-matched to an InP substrate. An emitter diffusion length of 800 nm was fitted versus 15.3 μm for InGaAs grown on n-InP. This value can be considered a minimum as longer diffusion lengths do not significantly increase the short wavelength response but shorter ones do lead to a decrease. The diffusion length in the InGaAs base layer reduces to

550 nm on the MBL versus 7.9 μm on n-InP. For the rear surface recombination a relatively low value of $1x10^4$ cm^{-2} is maintained on both substrate types while the front surface recombination rate is also $1x10^4$ cm^{-2} on both substrates. The best fit to the measured data is found by considering the thickness of the InP window layer as a variable. By reducing the thickness below the expected 100 nm to 70 nm a better fit is obtained for the EQE. The InP window layer thickness was confirmed at 100 nm by SEM (not shown) suggesting the optical absorption of this layer may be affected by the defects in the material.

Table 4.6: Summary of the 1-Sun PV performance of InAlAs and InGaAs solar cells on InP and GaAs substrates. The fitted emitter and base region minority carrier diffusion lengths are also given.

Solar Cell	**Substrate**	**Metal shading**	**V_{oc}**	**J_{sc}**	**Fill Factor**	**Efficiency**	**Fitted diffusion length**	
		%	*mV*	*mA/cm²*	*%*	*%*	***Emitter*** *nm*	***Base*** *nm*
InAlAs	InP	48	925	9.1	79	6.6	710	2078
InAlAs	GaAs	24	724	9.3	75	5	180	210
InGaAs	InP	9.8	357	38.2	69	9.3	15300	7880
InGaAs	GaAs	10.8	272	28.6	56.5	4.4	800	550

4.4.6. Analysis on the effect of defects on InAlAs solar cell electrical properties

Although the exact nature of the defects in the MBL is not understood, and outside the scope of this thesis, the reduced photovoltaic performance in InAlAs cells on the MBL was simulated by assuming that they act as threading defects as seen in other lattice mismatched solar cells. It has been shown previously that non-radiative recombination currents in III-V solar cells, characterised by n ~2 electrical behaviour, can be correlated with the threading dislocation density (TDD) in the junction [15]. A shorter minority carrier lifetime increases the reverse saturation current and reduces the open circuit voltage of a solar cell. An estimate of the TDD in the MBL structure can be found by analysing the measured DJV characteristics of InAlAs cells

on InP and GaAs substrates to reveal the drop in carrier lifetime caused by the integration on a lattice-mismatched substrate.

Method

The influence of threading defects in lattice-mismatched materials on the total lifetime of carriers in the junction, τ_{total}, is given by Equation 4.4 [15]. A contribution is seen from the defect free dopant dependent minority carrier lifetime, τ_{max}. A second contribution is seen from recombination at threading defects, τ_{TDD}, which reduces with increased defect density (Equation 4.5). It should be noted that it was assumed the threading defects are the dominant non-radiative recombination mechanism and that there is no other point defect related route for recombination. To find τ_{TDD}; firstly the total carrier lifetime, τ_{Total}, in InAlAs solar cells grown on GaAs substrates must be found. To do this the reverse saturation current density (in the dark) is assumed to be due to recombination in the depletion region only which is a reasonable assumption if n ~2. By neglecting any additional recombination components, an estimation can be made for the lifetime in the junction region (Equation 4.6) and a value for τ_{Total} found. τ_{max} is taken as the lifetime in a cell on a lattice matched substrate. With estimated values for τ_{total} and τ_{max}, a value for τ_{TDD} can be derived (Equation 4.4) and TDD estimated (Equation 4.5).

$$\frac{1}{\tau_{\mathrm{Total}}} = \frac{1}{\tau_{\mathrm{max}}} + \frac{1}{\tau_{\mathrm{TDD}}} \tag{4.4}$$

$$\tau_{\mathrm{TDD}} = \frac{4}{\pi^3(\mathrm{D})(\mathrm{TDD})} \tag{4.5}$$

$$J_{o2} = \frac{qn_i(T)W_d}{2\tau_{Total}(T)} \tag{4.6}$$

Data extraction and analysis

Figure 4.19 compares the forward DJV characteristics of InAlAs cells on GaAs (MBL) and InP substrates measured at 20^{o}C. For both cell types the ideality was found to be ~2 in the expected operating voltage of 0.7 – 1 V which indicates recombination in the depletion region and allows the assumption that recombination is described by Equation 4.6. A linear fit to this voltage range

for both cell types gave J_{o2} values of $2x10^{-8}$ A/cm^2 (MBL) and $1x10^{-10}$ A/cm^2 (InP) i.e. a factor of 50 difference.

With J_{o2} found, Equation 4.12 was used to solve for τ_{total}. For InAlAs cells the maximum carrier lifetime, τ_{max}, i.e. with no threading defects present, is 12 ns. For InAlAs on GaAs substrates; at 20^{o}C, a J_{o2} value of $2x10^{-8}$ A/cm^2 was gives a total carrier lifetime, τ_{total}, of 0.061 ns. Using these total and maximum carrier lifetime values a τ_{TDD} value of 0.062 ns was extracted. It can reasonably be assumed that the Hall mobility measured for InAlAs cells on InP substrates does not vary with TDD for values less than $1x10^8$ cm^{-2} [8]. Therefore, a D value of 3.6 cm^2/s was used to estimate the threading dislocation density in the cells with a value of $5x10^8$ cm^{-2} extracted.

Equation 4.1 was used to estimate the open-circuit voltage in the cells using the value extracted for J_{o2}. The value was found to be 675 mV which is 49 mV less than that measured.

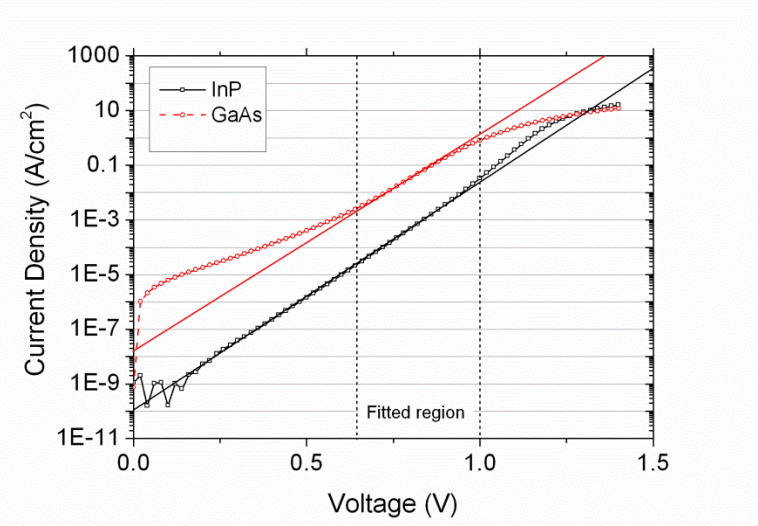


Figure 4.19: Comparison of the current density-voltage measurements for InAlAs cells grown on InP and GaAs substrates taken in the dark at 20 ^{o}C. A straight line is fitted in the 0.7 – 1.0 V region to extract J_{o2}.

Conclusion on TDD analysis

The analysis proposed by Andre et al. [8] was applied here to InAlAs cells in order to gauge the effectiveness of the MBL and estimate TDD and lifetime values in the cells. J_{o2} decreased by a factor of 50 for InAlAs cells on the MBL versus InP which corresponded to a measured V_{oc} of 724 mV or a reduction from the value on an InP substrate of 201 mV. The conclusion derived from this analysis is that defects from the MBL extend into the photovoltaic layers and are of too high a density to enable similar efficiencies to be achieved as those on lattice matched substrates.

While electrical analysis can indicate the range in which the density is, and an estimation of $5x10^8$ cm^{-2} derived, a more direct method is required to extract the exact carrier lifetimes and defect densities on the MBL. It is recommended to review the MBL structure to reduce the number of defects present and furthermore to concurrently investigate alternative methods to estimate the defect density in the MBLs with a discussion on the latter in the next section.

4.4.7. Alternative TDD analysis

In order to validate the extracted values for the lifetime of carriers in $In_{0.52}Al_{0.48}As$ on InP and GaAs substrates, Time-resolved Photoluminescence (TRPL) measurements were trialled. For accurate TRPL measurements a double heterostructure should be used where the material whose lifetime is to be measured is sandwiched between two wider bandgap regions [16]. These wide bandgap regions confine carriers excited by the incident laser beam to the InAlAs region by providing a barrier to transport into the substrate and to the front surface where surface recombination will occur. Without these wide bandgap layers the PL decay measured cannot be definitely described as characteristic of the InAlAs layer only. As $In_{0.52}Al_{0.48}As$ is the widest bandgap binary or ternary material, that is also lattice matched to InP, the growth of wide bandgap layers on either side of an InAlAs layer is not possible (A suitable quaternary material was not available in the Tyndall National Institute). Single layers of InAlAs were grown on InP substrates and TRPL measurements taken but significant responses were measured for the substrate regions which led to difficulties in extracting accurate lifetime measurements for InAlAs only. Quasi-steady-state photoconductance [17] offers an alternative measurement technique which may be applicable. Samples are irradiated by a quasi-steady-state source and photoconductance measured for the sample. As the creation and recombination of carriers must balance in steady state an analysis is completed to extract the lifetime of the carriers where this technique has been applied successfully to GaAs and GaN wafers [18].

A direct physical method of quantifying the TDD in a semiconductor layer is by direct observation. Etch pit density measurements involve the selective removal of epitaxial layers from a semiconductor structure to the layer of the device where the defect density is to be measured. A plan image of the layer is taken using SEM and the number of defects counted for a given area. This number is then extracted to give a cm^{-2} value. For InAlAs layers a H_3PO_4:H_2O_2:H_2O (1:1:38, 100 nm/min) wet etch was used to completely remove the InAlAs layers to the expose the MBL (Figure 4.20).

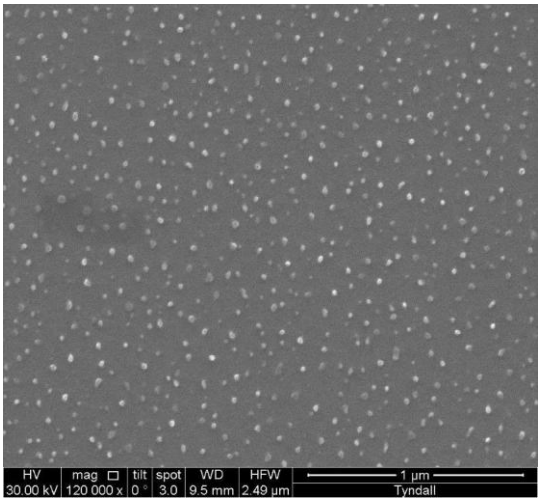


Figure 4.20: SEM image of the InGaAs MBL layer after InAlAs removal by wet etching. The 'defects' are directly visible and were used to estimate the defect density in the MBL.

A large number of 'defects' appear as dots in SEM images taken on these samples. The number of defects was counted in a series of 1 μm x 1 μm areas for a number of images with a value close to 100 consistently counted. This gives a density of $1x10^{10}$ cm^{-2}. If what is directly observed is threading defects then this method derives a value that is two orders of magnitude greater than that found through electrical analysis of the junction. It should be noted, however, that the images taken were of the MBL layer which is presumed highly defective and not all of these defects may permeate through to the junction of the solar cell. Furthermore, pattern transfer is possible during the wet etching process where defects which are not directly in the MBL layer may be visible in the SEM image due to the wet etch transferring an image of them. For these reasons this method of TDD estimation was considered less reliable although it does suggest the density is higher in the MBL than in the solar cell itself as expected.

An additional method of direct observation is through the use of TEM imaging. A region of the defective material can be imaged and the number of defects present counted. This allows an estimation to be made for the number of the defects present throughout the material to be extracted. As our TEM analysis was completed on only one sample and over a small region it was decided not to use TEM images to estimate the TDD in our material. Observing the number of defects over a large area and a large number of samples would allow the estimation of the TDD in MBLs for solar cells.

4.5. Summary

InGaAs solar cells, to form the bottom cell in a III-V mechanically stacked solar cell, have been designed and characterised. Compared to the state of the art single-junction InGaAs cells as presented in [2] and [6], the lower photocurrent density can be attributed to absorption in the relatively thick InP window layer and the design of the anti-reflection coating for the 880 – 1700 nm wavelength range. The lower open-circuit voltage, as compared to Matsubaru *et al.*, I attribute to their use of a n-on-p configuration which leads to longer diffusion lengths in the 3.4 μm thick base region. Nevertheless, given the narrower spectrum for which the InGaAs cell in this chapter was designed, a 1-Sun conversion efficiency of 9.3% compares well to their result. Furthermore a maximum EQE of 93.8% was measured at 1030 nm as desired for light transmitted through GaAs.

InAlAs cells were designed and characterised to determine the PV characteristics of this material relevant to multi-junction cell fabrication. The extracted minority carrier diffusion lengths of 710 and 2080 nm for the emitter (p-type $3x10^{18}$ cm^{-3}) and base (n-type $4x10^{17}$ cm^{-3}) layers are adequate for use in monolithic cell formation and compare to 14 μm and 5 μm for equivalently doped GaAs layers. Furthermore, fabricated cells had a PV efficiency of 6.6% using 800 nm thick absorber layers under 48% metal shading showing the promising potential of the material. The measured open-circuit voltage of 925 mV is close to the state of the art for an InAlAs cell under 1-Sun conditions. Single-junction cell performance can be improved by using a thicker base layer to absorb more photons, reduce grid-metal shading and using a double layer anti-reflection coating to reduce reflection across a broader wavelength range. Additionally, a more comprehensive understanding of the carrier transport properties of InAlAs as a function of doping level and polarity is needed to design an optimised junction to increase the power produced.

An $In_xGa_{1-x}As$-InP metamorphic buffer layer has been used to grow InAlAs and InGaAs solar cells, at the lattice constant of InP, on GaAs substrates. The decrease in performance as compared to control cells on InP substrates has been attributed to defects in the MBL as observed in TEM images. The defects were observed to extend through the grading layer and into the photoactive region of the cells with an electrical analysis used to extract a density value of $5x10^8$ cm^{-2}, although alternative methods are recommended to confirm this value. The defects resulted in reduced minority carrier diffusion lengths in the cells where the values for cells on GaAs substrates was an order of magnitude lower than those on InP substrates. Further work is required to improve the MBL quality to reduce the density of defects that extend into the device.

4.6. References

[1] P. Bhattacharya, *Properties of lattice-matched and strained Indium Gallium Arsenide*. INSPEC, 1993.

[2] A. Wieczorek, V. Djara, F. H. Peters, J. O'Callaghan, K. Thomas, and B. Corbett, "Inductively coupled plasma deep etching of InP/InGaAsP in Cl[sub 2]/CH[sub 4]/H[sub 2] based chemistries with the electrode at 20 [degree]C," *J. Vac. Sci. Technol. B Microelectron. Nanometer Struct.*, vol. 30, no. 5, p. 051208, 2012.

[3] H. Matsubara, T. Tanabe, A. Moto, Y. Mine, and S. Takagishi, "Over 27% efficiency GaAs/InGaAs mechanically stacked solar cell," *Sol. Energy Mater. Sol. Cells*, vol. 50, no. 1–4, pp. 177–184, Jan. 1998.

[4] T. Yamada, A. Moto, Y. Iguchi, M. Takahashi, S. Tanaka, T. Tanabe, and S. Takagishi, "5× 5 cm2 GaAs and GaInAs Solar Cells with High Conversion Efficiency," *Jpn. J. Appl. Phys.*, vol. 44, pp. L985–L987, Jul. 2005.

[5] M. S. Leite, R. L. Woo, W. D. Hong, D. C. Law, and H. A. Atwater, "Wide-band-gap InAlAs solar cell for an alternative multijunction approach," *Appl. Phys. Lett.*, vol. 98, p. 093502, 2011.

[6] R. R. King, D. Bhusari, A. Boca, D. Larrabee, X.-Q. Liu, W. Hong, C. M. Fetzer, D. C. Law, and N. H. Karam, "Band gap-voltage offset and energy production in next-generation multijunction solar cells," *Prog. Photovolt. Res. Appl.*, vol. 19, no. 7, pp. 797–812, 2010.

[7] W. Nakwaski, "Effective masses of electrons and heavy holes in GaAs, InAs, A1As and their ternary compounds," *Phys. B Condens. Matter*, vol. 210, no. 1, pp. 1–25, Apr. 1995.

[8] C. L. Andre, D. M. Wilt, A. J. Pitera, M. L. Lee, E. A. Fitzgerald, and S. A. Ringel, "Impact of dislocation densities on n+/p and p+/n junction GaAs diodes and solar cells on SiGe virtual substrates.," *J. Appl. Phys.*, vol. 98, no. 1, p. 014502, 2005.

[9] S. M. Sze, *Physics of Semiconductor Devices*. John Wiley and Sons, 1981.

[10] N. Bouarissa and M. Boucenna, "Band parameters for AlAs, InAs and their ternary mixed crystals," *Phys. Scr.*, vol. 79, no. 1, p. 015701, Jan. 2009.

[11] M. R. Brozel and G. E. Stillman, *Properties of Gallium Arsenide*. INSPEC, 1996.

[12] B. H. Müller, R. Lantier, L. Sorba, S. Heun, S. Rubini, M. Lazzarino, A. Franciosi, E. Napolitani, F. Romanato, A. V. Drigo, L. Lazzarini, and G. Salviati, "Zn0.85Cd0.15Se active layers on graded-composition InxGa1−xAs buffer layers," *J. Appl. Phys.*, vol. 85, no. 12, pp. 8160–8169, Jun. 1999.

[13] A. Gocalinska, M. Manganaro, and E. Pelucchi, "Suppression of threading defects formation during Sb-assisted metamorphic buffer growth in InAs/InGaAs/InP structure," *Appl. Phys. Lett.*, vol. 100, no. 15, pp. 152112–152112–5, Apr. 2012.

[14] A. Gocalinska, M. Manganaro, E. Pelucchi, and D. D. Vvedensky, "Surface organization of homoepitaxial InP films grown by metalorganic vapor-phase epitaxy," *Phys. Rev. B*, vol. 86, no. 16, p. 165307, Oct. 2012.

[15] J. C. Zolper and A. M. Barnett, "The effect of dislocations on the open-circuit voltage of gallium arsenide solar cells," *IEEE Trans. Electron Devices*, vol. 37, no. 2, pp. 478 –484, Feb. 1990.

[16] R. R. King, J. H. Ermer, D. Joslin, M. Haddad, J. Eldredge, N. H. Karam, B. Keyes, and R. K. Ahrenkiel, "Double heterostructures for characterisation of bulk lifetime and interface recombination

velocity in III-V multi-junction solar cells," in *Presented at the 2nd World Conference on Photovoltaic Solar Energy Conversion*, Vienna, Austria, 1998.

[17] R. A. Sinton, A. Cuevas, and M. Stuckings, "Quasi-steady-state photoconductance, a new method for solar cell material and device characterization," in , *Conference Record of the Twenty Fifth IEEE Photovoltaic Specialists Conference, 1996*, 1996, pp. 457–460.

[18] B. Chhabra, S. Jacobs, and C. B. Honsberg, "Suns-Voc and minority carrier lifetime measurements of III-V tandem solar cells," in the *Conference Record of the 2006 IEEE 4th World Conference on Photovoltaic Energy Conversion*, Waikoloa, Hawaii, 2006.

Chapter 5

BCB-bonded GaAs-InGaAs mechanically stacked solar cell

5.1. Introduction

The design concept for a GaInP/GaAs-InGaAs mechanically stacked solar cell (MSSC) has been outlined in Chapter 3 and the characteristics of InGaAs cells fabricated on InP substrates were presented in Chapter 4. As a first demonstration of this stacked cell system single junction GaAs and InGaAs solar cells were used to form prototype MSSCs fabricated through BCB bonding. This chapter introduces single-junction GaAs solar cells fabricated for use in this MSSC. It continues by discussing the material properties of BCB relevant to stack fabrication and provides experimental justification for the use of BCB to improve the optical transmission of the solar cell interface. Finally a process outline for BCB-bonding of cells is provided and the performance of GaAs-BCB-InGaAs MSSCs are presented.

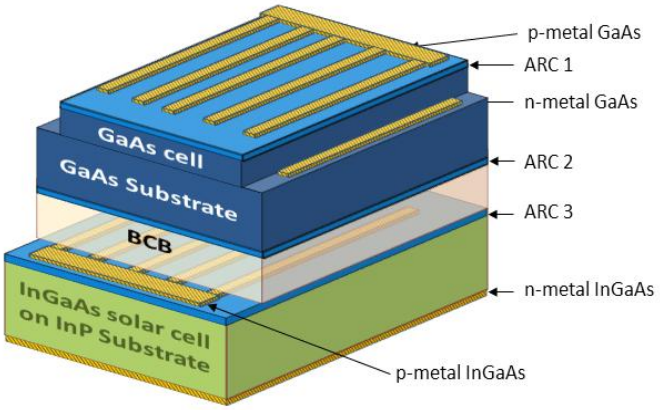


Figure 5.1: Schematic outline of the fabricated GaAs-InGaAs stacked solar cell as designed in Chapter 3.

5.2. Single-Junction GaAs Solar Cells

Mechanically stacked solar cells have traditionally been considered an expensive route to multi-junction solar cell production given the numerous semiconductor substrates used and additional fabrication costs. Recent research into these devices, however, has tended to focus on cost saving techniques for MSSC production. With advances in epitaxial-lift-off thin-film III-V cells and substrate re-use [1]; these top cells can be bonded to narrow bandgap bottom cells which provide mechanical support while also increasing the efficiency of the multi-junction device. Thin-film top cells based on GaAs have been used to form dual-junction GaAs-Ge cells with an efficiency of 25.1% [2] and triple-junction GaInP/GaAs-Si stacked cells with an efficiency of 27.3% [3] both measured under 1-Sun conditions. This stacked cell fabrication route provides the greatest possibilities for efficiency gains and cost-savings as the dual challenges of III-V substrate cost and light absorption in substrates are tackled. This thesis uses a single-junction GaAs top cell, which was fabricated for use in a prototype MSSC.

5.2.1. GaAs cell design

A single-junction GaAs solar cell was designed and grown in an Aixtron Aix200/4 horizontal MOVPE reactor. A p-on-n structure was used to reduce free-carrier absorption losses in the substrate which are higher in p-type substrates [4]. The cell structure, grown on a double-side polished GaAs p-type wafer (Zn-doped, N_a~$1x10^{18}$ cm^{-3}), is outlined in Table 5.1 and consists of a 3 μm base layer to strongly absorb wavelengths near the band edge of GaAs, a relatively thick 400 nm p+GaAs emitter layer to reduce resistance to lateral current flow increasing the Fill Factor of devices, AlGaAs carrier blocking layers at the front (85% Al) and back (30% Al) of the p+GaAs/n+GaAs emitter and base layers to reduce surface recombination and a highly doped p-GaAs front contact layer.

Table 5.1: Nominal layer structures of single-junction GaAs and InGaAs cell grown by MOVPE. Details of the as grown structure are given in Appendix D.

Layer	**Material**	**Doping** (cm^{-3})	**Thickness** (μm)
Cap	p^{++} GaAs	$8x10^{18}$	0.2
Window	p^{+} $Al_{0.85}Ga_{0.15}As$	$1x10^{17}$	0.04
Emitter	p^{+} GaAs	$2x10^{18}$	0.4
Base	n^{+} GaAs	$2x10^{17}$	3
BSF	n^{+} $Al_{0.3}Ga_{0.7}As$	$1x10^{18}$	0.04
Buffer	n^{+} GaAs	$2x10^{18}$	0.1
Substrate	n-GaAs	$1\text{-}4x10^{18}$	140

5.2.2. Cell Processing

A GaAs solar cell fabrication process was developed. Both n- and p-type contacts were fabricated on the front surface of the cell (Figures 5.2 and 5.3 (b)) to allow the use of electrically insulating epoxy to bond the cells. n-contacts were formed by wet etching through the photoactive region of the device and depositing n-metal on the exposed n-type substrate. A front surface grid pattern (p-contact) was deposited by e-beam evaporation providing total metal shading by both contact types of 11%. Wet etching was used to remove the cap layer in open regions and isolate individual cells (0.22 cm^2). ZnS and SiO_2 (48 and 74 nm respectively) were deposited on the front surface by e-beam evaporation and PECVD respectively to form a dual layer ARC. To improve the long wavelength (850 – 1700 nm) transmission of the GaAs cell; the substrate was thinned to 140 μm using a Br:MeOH solution and a 120 nm layer of ZnS (n~2.3) deposited on the back surface to act as an anti-reflection coating between the cell and adhesive as designed in Chapter 3. GaAs solar cells with p-metal grid contacts on the front but blanket n-metal coverage on the back surface of the cells were also fabricated as control devices (Figure 5.3 (a)).

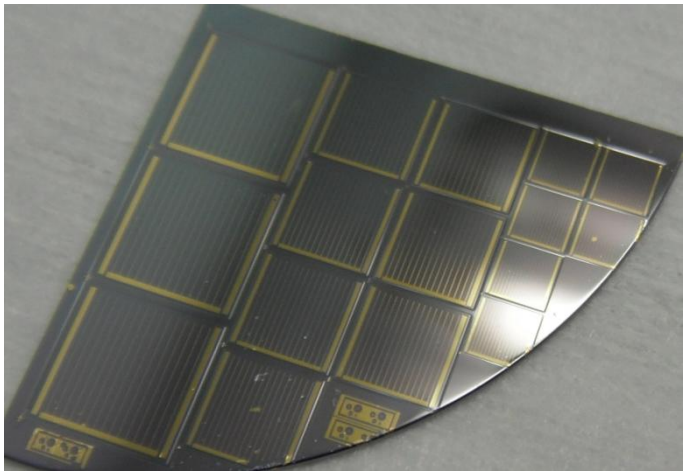


Figure 5.2: Optical image of a processed 1/4 wafer of single-junction GaAs solar cell material with both p- (grid line and bus bars) and n-type contacts (bus bars only) visible on the front surface. An anti-reflection coating was not deposited on this chip.

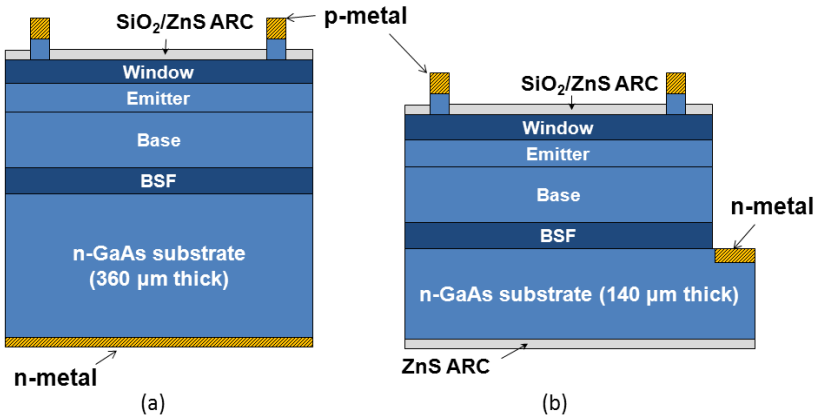


Figure 5.3: Outline of the processed (a) control and (b) front surface contacted GaAs solar cells.

5.3. BCB Bonding

A flip-chip tool, FINEPLACER (Figure 5.4) from Finetech, was used to perform the adhesive bonding between the cells as it allows pressure to be applied, sample heating with some alignment. The tool had a placement accuracy of <5 µm.

A limitation of this flip-chip system is its design for aligning features on the chip surfaces which are to be brought into contact during bonding. For the MSSC, alignment was desired between the grid metal patterns on the front of both cells, which are not the two surfaces being brought into

contact during bonding. Therefore the alignment capabilities of the flip-chip tool were used to align the edges of the cells only.

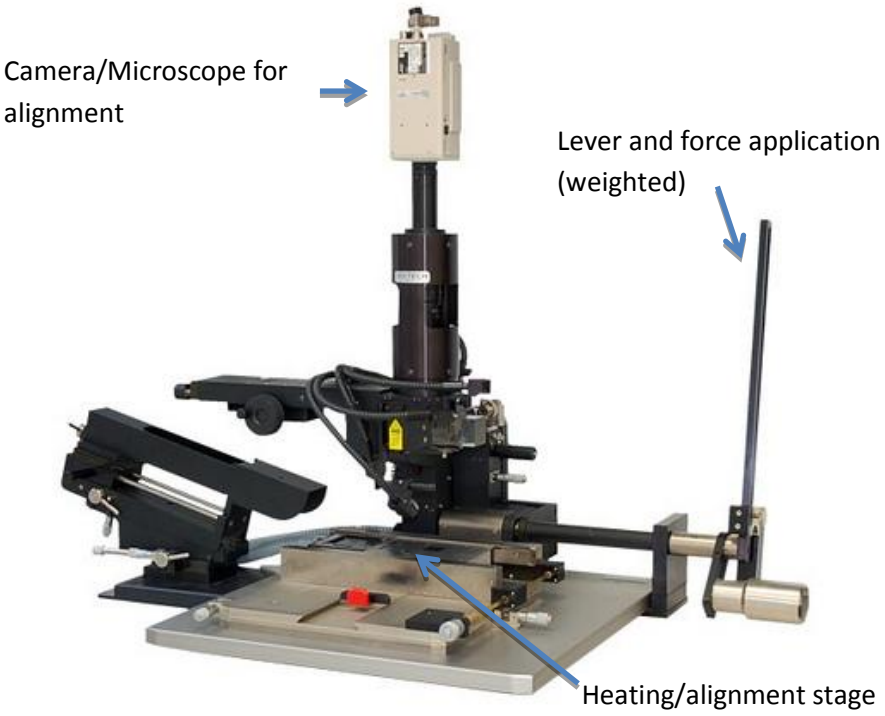


Figure 5.4: Flip Chip Bonder FINEPLACER® pico MA (© Finetech 2013: http://www.flickr.com/photos/30984232@N02/2903755265).

BCB was chosen as the most suitable adhesive for stacking the solar cells (Chapter 3). Two grades of BCB from the Cyclotene 3000 series dry etch resins from Dow Corning were trialled, namely, 3022-46 and 3022-57. The difference between the resins is the volumetric ratio of solvent (Mesitylene), although the exact volumetric ratio is not given by the supplier, Dow Corning [5]. The different solvent volume ratios allow control of the viscosity of the samples and subsequently the film thickness versus spin speed when applied by spin-coating where 3022-57 is the higher viscosity solution. Ideally film thicknesses of 3-5 μm would be spun on the bonding surface of each cell in order to fabricate a 6 – 10 μm BCB bonding layer between the cells. 3022-46 and 3022-57 were trialled initially as they provide film thicknesses in this range using stadard spin coating speeds, as shown in Figure 5.5.

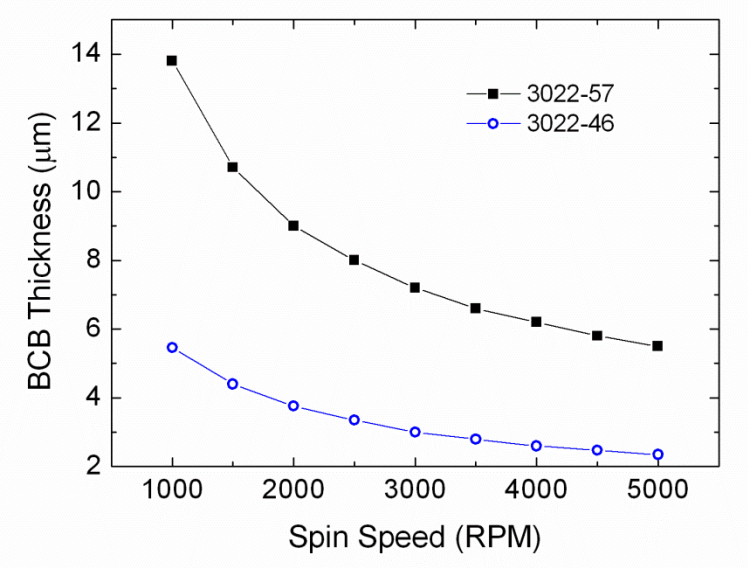


Figure 5.5: BCB layer thickness versus spin speed for both BCB resins considered in this study where 3022-57 is the higher viscosity solution.

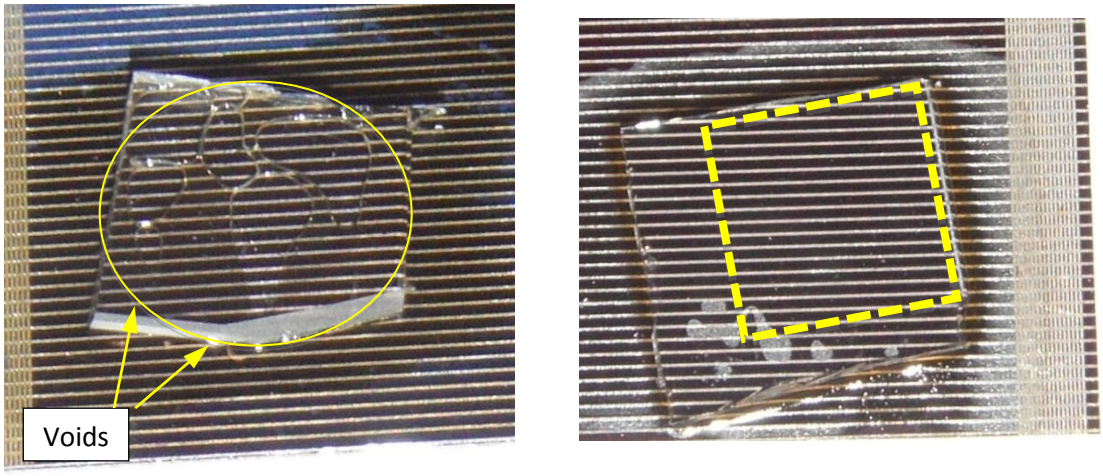
5.3.1. Phase 1: Bond Development

In order to develop a final bonding process using BCB; trials were initially carried out using Si solar cells. 5 mm x 5 mm quartz and GaAs pieces were bonded to Si cells under various conditions to compare the quality of the bond associated with each BCB resin and to establish the optimum curing conditions.

a) Void free adhesive bonding process development by Quartz-Si bonding

Quartz bonding to Si solar cells (cell details given in Appendix E) allowed visual inspection of the bond to investigate if voids formed at interface. Figure 5.8 (a) is an optical image of a typical bond formed using 3022-46 where the higher volume of solvent requiring outgassing before and during bonding leads to void formation at the bonding interface. A high portion of voids was typically formed during pre-curing in the flip-chip bonder before samples were placed in an oven for final curing. Figure 5.8 (b) is a typical image for a bond between quartz and a Si solar cell using 3022-57 under the best established conditions of a 30 second temperature ramp-up (to 150 ^{o}C) of the BCB in the flip-chip bonder before contacting the cells for 5 minutes at 150 ^{o}C. The lower volume of solvent in 3022-57 is outgassed during the temperature-ramp but the BCB maintains a low enough viscosity to allow bonding of the cells. The voids evident from the images in Figure 5.8 (b) are due to the area mismatch between the quartz piece and the flip-chip

bonder pressure pad. In other words, the pressure applied by the flip-chip bonder (highlighted by the blue square) did not extend to the corner where voids formed.



(a) (b)

Figure 5.6: Optical image of quartz pieces bonded to Si solar cells using (a) 3022-46 and (b) 3022-57 grade BCB resin. In (a) the voids formed during processing are highlighted in the yellow bubble and in (b) the region where pressure was applied by the flip-chip bonder is highlighted by a dashed yellow square in (b).

Once a suitable process was found to ensure no bubble formation in a quartz-Si solar cell bond; Si chips were bonded to fabricated InGaAs solar cells to ensure the same process was suitable for bonding of two semiconductor materials. The lack of voids was confirmed by investigation of cross-sectional optical images taken on diced cells with a typical image given in Figure 5.7.

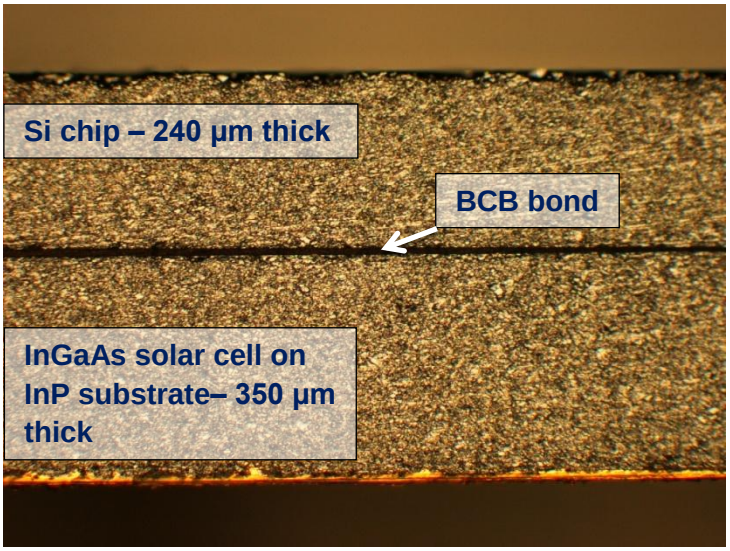


Figure 5.7: Optical image of a Si chip bonded to an InGaAs solar cell (post scribing to form cross-section for imaging) used for development of the flip-chip process.

b) GaAs-Si bonding for optical measurement

Following optimisation of the bonding parameters (pressure, temperature, etc) GaAs chips (5 mm x 5 mm, double-side polished, 360 µm thick and n = 1-4x10^{18} cm^{-2}) were next bonded to Si solar cells to investigate the improvement achieved in the optical performance of the cell interface using adhesive versus an air gap. EQE measurements of Si solar cells stacked under GaAs chips with an air gap and BCB-bonded interface were compared. To reduce reflection from the front surface of the GaAs chips a SiO_2/ZnS double-layer ARC was deposited. The back surface of the GaAs chips were processed using one of the following methods:

1) A double-layer SiO_2/ZnS (160/110 nm) ARC was deposited which was designed to reduce reflection in the 850 - 1700 nm range: Figure 5.8 (a).
2) A single-layer ZnS ARC was deposited designed to reduce reflection between GaAs and BCB in the 850 – 1700 nm range: Figure 5.8 (b).

The EQE for both stacks is shown in Figure 5.9, demonstrating that the response of the Si bottom cell is improved by using an n = 1.54 interface filled versus the air gap with an optimised ARC structure. The response of the cell stacked using BCB reaches a maximum of 52.5% at 940 nm versus 50% for an air gap at the same wavelength (a simulated difference of 3% was expected between the two optical designs). Also shown is the response of the Si cell under a GaAs chip

with 130 nm ZnS on the back surface (i.e. that used for BCB-bonding) before bonding showing the improvement post bonding.

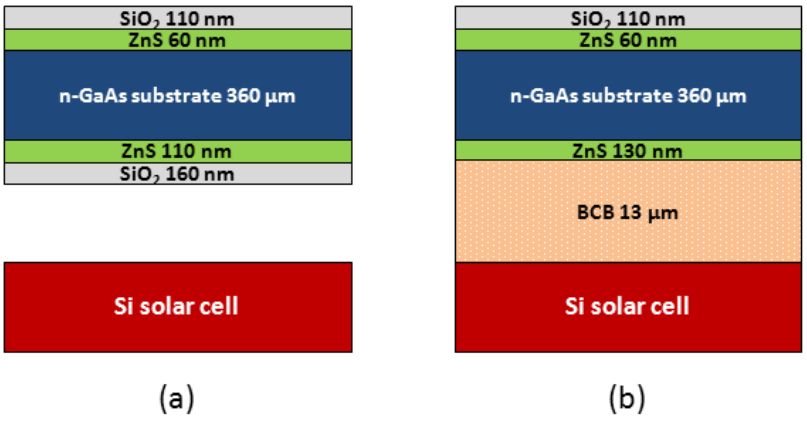


Figure 5.8: Outline of the two stack set-ups used to evaluate the effectiveness of BCB in reducing interface reflection (a) a DLARC deposited on the back surface of an n-GaAs chip and (b) a single-layer ZnS ARC and BCB bond between an n-GaAs chip and the Si solar cell.

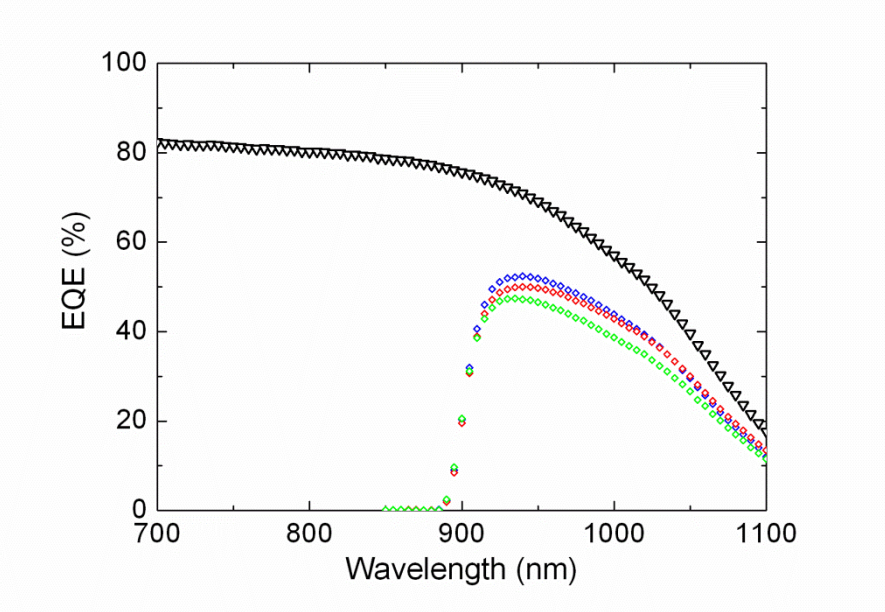


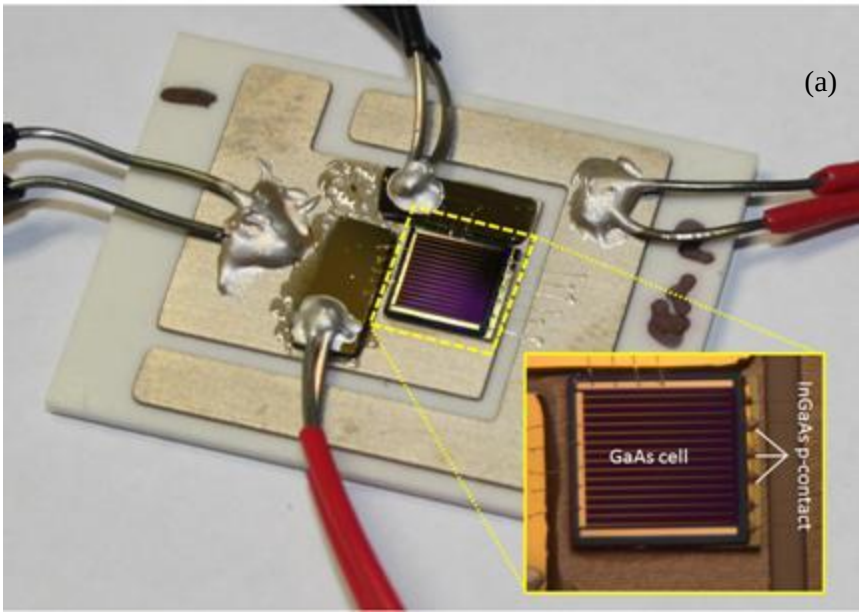
Figure 5.9: Measured EQE response of a Si solar cell before stacking with GaAs (black triangles) and post stacking with an air gap (red diamonds) and a BCB bond (blue diamonds). Also shown is the improvement pre-bonding with BCB for a single-layer ZnS ARC (green diamonds).

5.3.2. Phase 2: Final bonding process for MSSCs

Fabrication of the MSSC involved a five step process using the GaAs and InGaAs cells grown by MOVPE and the BCB adhesive.

1) The InGaAs cell was epoxy bonded to a Ni coated, patterned copper AlN submount using HS20 Ag-loaded conductive epoxy from EpoTek.
2) Droplets of BCB were manually applied to the active surface of the InGaAs cell. The GaAs top cell was attached to the InGaAs bottom cell using a Finetech Flip-Chip bonder. Benzocucylobutene (Cyclotene 3022-57 resin) from the Cyclotene Advanced Electronics Resins range from Dow Corning was used. It should be noted that both cells do not employ the same metallisation pattern and some negative impact on bottom cell performance was expected due to excess shading by the top cell metallisation pattern since high precision grid metal alignment between the two cell types was not carried out in this study.
3) The MSSC was pre-cured at 150ºC under a pressure of 4 N/cm^2 for 5 minutes to pre-bond and cure BCB to ~80% polymerization [6].
4) The bonded chips were then cured in an oven at 210ºC for 2 hours.
5) The solar cell fabrication and packaging process was completed by wire-bonding from the InGaAs bus bar p-contact to the patterned Ni coated AlN submount and the remaining GaAs cell bus bars to Au-coated Si pieces mounted with electrically insulating epoxy on the submount.

A packaged GaAs-InGaAs stacked cell is shown in Figure 5.10 (a). Optical microscope images taken on diced stacks were used to measure the adhesive bond thickness ~ 13 μm with a typical image shown in Figure 5.10 (b).



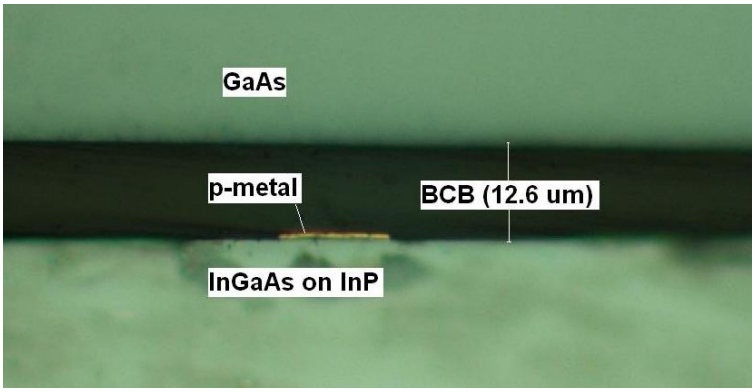


Figure 5.10: Optical images of (a) the fabricated and packaged GaAs-InGaAs stacked cell, the inset image shows the wire bonding to the cell bus bars, and (b) the BCB bond between a GaAs top and InGaAs bottom cell post dicing.

5.4. Mechanical stack measurements

The photovoltaic conversion efficiency of the solar cells were measured using a Newport Oriel 91193 series 1600 W solar simulator, where the incident spectrum was calibrated at 0.1 W/cm^2 using a reference cell, and are summarised in Table 5.2 and Figure 5.11. The EQE and front surface reflection of all cells was measured using a PVE300 Spectral Response System from Bentham Instruments. The illumination area for EQE measurements was smaller than the cell area. A grid metal shading loss occurs, due to the thin metal fingers only, of 3.3% for the GaAs cell and 9.9% for the InGaAs cell in an MSSC.

Table 5.2: Measured photovoltaic performance of the fabricated cells under 1-Sun conditions.

Cell	J_{sc}	V_{oc}	FF	η
	mA/cm^2	mV	%	%
GaAs control	26.4	1023	82.5	22.3
GaAs – top contact	25.4	1014	79.9	20.6
InGaAs	38.2	357	69	9.3
Stacked InGaAs	19.3	339	70.7	4.6
GaAs-InGaAs	-	-	-	25.2

Control GaAs cells with n-metal contact on the back surface of the device had an efficiency of 22.3% under 1-Sun conditions with an open-circuit voltage of 1023 mV and a short-circuit current density of 26.4 mA/cm^2. In stacked configuration, with n-contacts on the front surface, the GaAs top cell short-circuit current density drops to 25.4 mA/cm^2 due to increased cell shading. The increased current conduction path due to lateral conduction to the n-contact also increases the series resistance of the cell leading to a drop in Fill Factor and a cell efficiency of 20.6% when measured in a stack. A relatively high Fill Factor of 79.9% was, nevertheless, achieved by using the 140 μm thick substrate as the lateral conduction layer. The use of a SiO_2/ZnS double layer ARC reduces front surface reflection to 3.5 - 5% in the 400 – 900 nm range. Accounting for the optical losses, the GaAs cell has an IQE of > 98% in the same range outlining the high quality of the epitaxial material. The potential of thinned III-V solar cells has already been established with a GaAs cell efficiency of 23.2% [2] achieved post-substrate removal and contact formation on the rear-surface to allow illumination of a bottom cell. These techniques should be readily applied to dual-junction top cells allowing formation of a triple-junction stack.

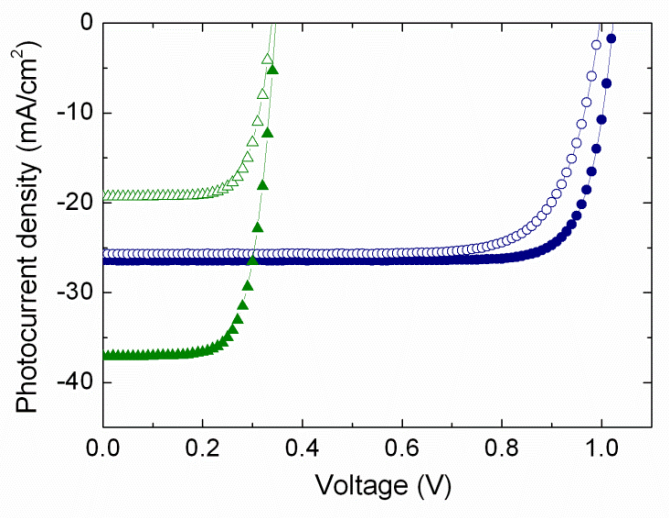


Figure 5.11: Measured photocurrent density-voltage characteristics of a control GaAs cell (closed circles), top-contacted GaAs cell (open circles), stand alone InGaAs cell (triangles) and stacked InGaAs cell (open triangles) under 1-Sun conditions.

5.4.1. External Quantum Efficiency

While the top cell contributes by far the largest portion of stack efficiency, high performance bottom cells are required to provide a significant efficiency boost. The single-junction InGaAs cells outlined in Chapter 4 had an open-circuit voltage of 357 mV when measured under 1-Sun conditions and a short-circuit current density of 38.2 mA/cm^2. The measured EQE is given in Figure 5.12 and shows how the low short-circuit current density value measured is due to the design of the cell to give a large response in the 850 – 1700 nm range. The expected absorption in the thick 100 nm InP window layer is shown with a 50% loss of photons in the 400 – 900 nm range. Furthermore, the anti-reflection coating was optimised for IR photon transmission with a minimum measured at 1000 nm. Nevertheless, a measured 1-Sun efficiency of 9.3% was achieved in these cells before integration in the stack. By focusing the design on wavelengths > 850 nm a large photocurrent should be expected from this cell post BCB-bonding to a GaAs top cell and this was found with a measured short-circuit current density of 19.3 mA/cm^2. The InGaAs cell efficiency in mechanically stacked configuration was 4.6% leading to a total 1-Sun stack efficiency of 25.2%.

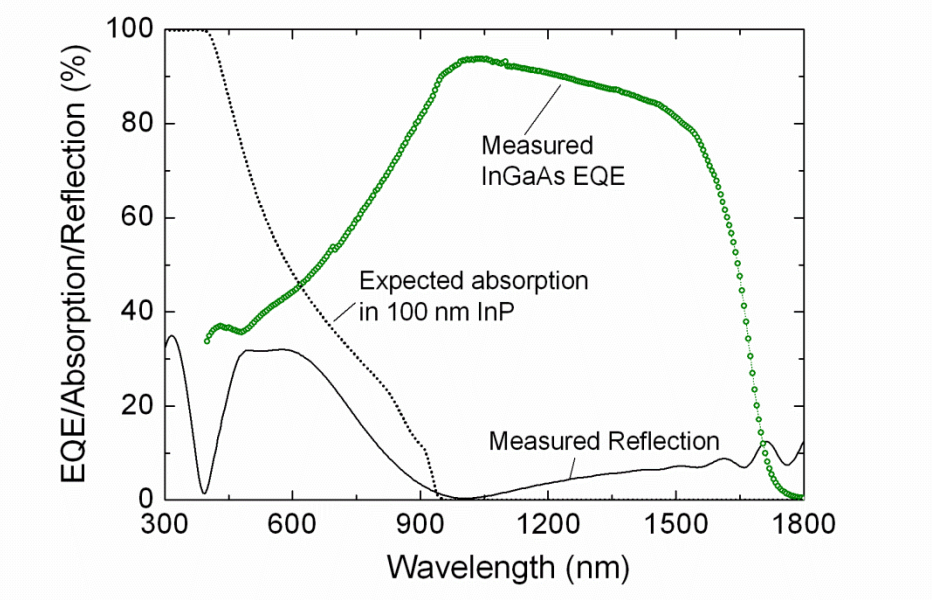


Figure 5.12: Measured EQE (green diamonds) of the stand-alone InGaAs solar cell as well as the measured reflection from the front surface and the simulated absorption of the AM1.5G spectrum in a 100 nm InP layer.

The EQE of the InGaAs cell post-bonding in a stack (Figure 5.13) achieves a maximum value of 74% at 1040 nm. The decrease in response versus the initial InGaAs cell is caused by reflection from the front surface of the GaAs cell and the BCB bonding interface which is measured as 14-21% in the relevant wavelength range, the increased shading in the cell caused by non-alignment of the metal grids (9.9%) and the absorption of long wavelength photons in the GaAs substrate.

As outlined in Figure 5.1 the p-contact of the InGaAs solar cell was contacted by fabricating a smaller GaAs top cell and bonding in such a fashion as to leave a small fraction of the top surface of the InGaAs cell exposed. This leads to an overestimation of the short-circuit current density of the bottom cell when measuring in the solar simulator. In order to predict the photocurrent from the bottom cell under direct sunlight an estimated value of 15.1 mA/cm^2 was derived using the measured EQE and the ASTM G-173-03 AM1.5d spectrum (888 W/m^2) [7].

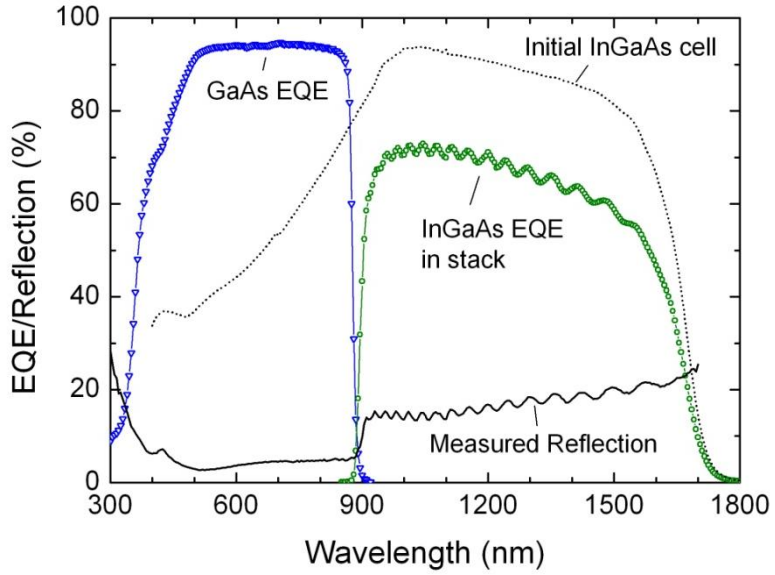


Figure 5.13: Measured EQE of the GaAs (blue triangles) and InGaAs (green circles) cells in stacked formation. Also shown is the measured reflection from the stack (solid line) and the EQE of the InGaAs cell pre-bonding (dots).

5.4.2. Optical Analysis

The EQE of the stacked InGaAs cell can be readily improved by using a thin-film III-V top cell where the substrate has been completely removed to reduce absorption losses, by design of identical metal grids which are aligned during bonding and further optimisation of the reflectance characteristics of the stacked cells. To confirm the improvement in EQE response of the bottom cell as a function of GaAs substrate thickness an additional stack was fabricated which featured all the same specifications as previously outlined except the n-GaAs substrate was not thinned i.e. the n-GaAs substrate was a 360 μm thick double-side polished wafer. As shown in Figure 5.14 the EQE response of the bottom cell improved by ~ 25% absolute efficiency in the 900 – 1150 nm range with an increase from 59.3 to 74.1% at 1040 nm.

The fabricated stack did not feature the optimum anti-reflection coating scheme designed in Chapter 3. The development of the InGaAs cell required the use of a SiN_x passivation layer to reduce non-radiative recombination losses in this cell. The refractive index of this layer, ~ 1.9 for the relevant wavelength range, is lower than the desired 2.32. Figure 5.15 shows the expected reflection at the cell interface only for the optimised (black line) and as fabricated (grey line) optical layers. The simulated reflection for the as fabricated is significantly higher than for the optimised ARCs and a result the expected short-circuit current density in the bottom cell drops by 4.3%.

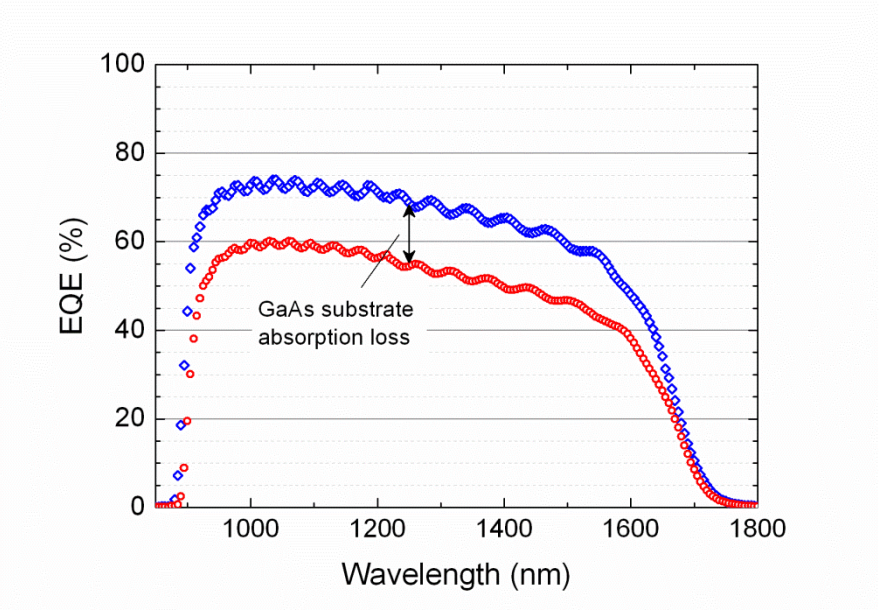


Figure 5.14: Measured EQE of an InGaAs bottom cell stacked under a GaAs top cell with a 360 µm thick substrate (red circles) and a 140 µm thick substrate (blue substrates).

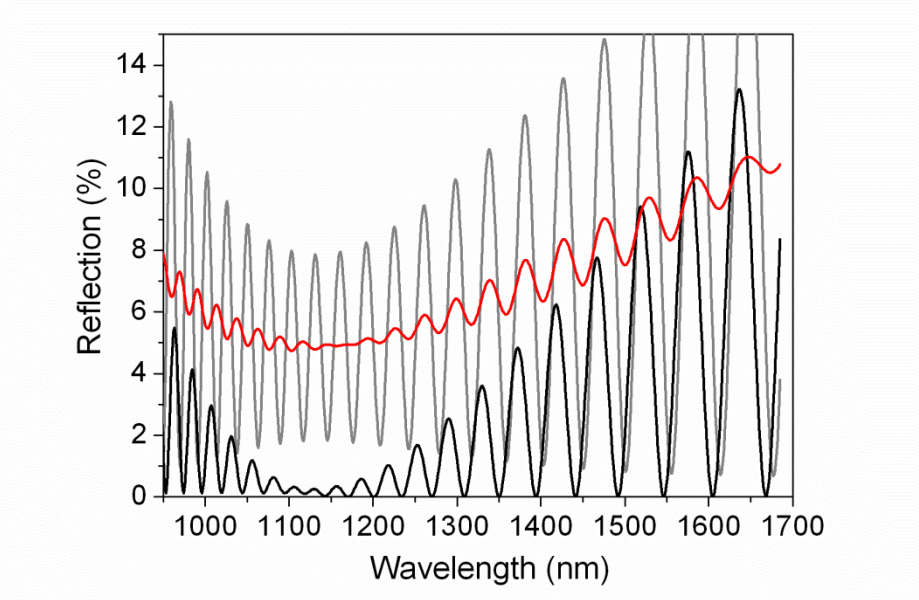


Figure 5.15: Simulated reflection at the cell interface for the optimum (black) and fabricated (grey) optical coatings. The red line is the simulated as fabricated coatings when 'wedging' is considered.

Figure 5.16 shows the measured reflection from the front surface of the stacked cell (blue line). In order to confirm the performance of the optical model the expected reflection from the stack was

also simulated with the closest fit shown. It was found the optical performance of the cell behaved as if the thickness of the top cell and adhesive interface were not uniform across the cell area. This was expected for the top cell where the wet etch thinning process is not uniform and for the interface as the flip-chip process does result in thickness variation across the epoxy bond known as 'wedging'. These variations were accounted for in the model by simulating the reflection from the interfaces for various thicknesses and averaging the results. The best fit was found for thicknesses between 12.8 – 13.2 μm across the 2 x 2 mm illumination spot with the simulated reflection from the cell interface due to 'wedging' shown as a red line in Figure 5.17 with an obvious reduction in peaks. Furthermore the measured reflection, in Figure 5.18, is 3% greater at all measured wavelengths suggesting the 3.3% metal coverage (e-beam Ti/Pt/Au) is highly reflective.

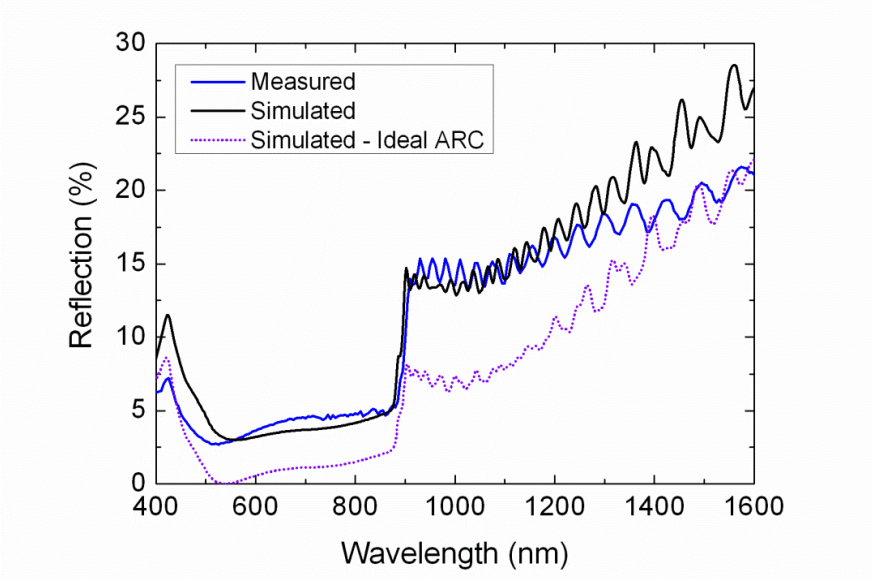


Figure 5.16: Measured reflection from the front surface of the stacked solar cell (blue line). Also shown is the simulated reflection for the fabricated optical system (black line) and the optimum optical coating regime (purple dots).

The simulated reflectance when using the optimum anti-reflection coatings at the interface and assuming metal shading is reduced to 0% is presented in Figure 5.18. Considering this to be the only optical loss in the stack and assuming a thin-film GaAs based top cell with no absorption losses, an expected short-circuit current density of 19.52 mA/cm^2 was determined for the AM1.5d spectrum (1000 W/m^2) using the IQE derived for the InGaAs cell in Chapter 4.

5.5. Future implementation

For commercial MSSC production, the scalability of the bonding process is an important factor. Wafer bonding allows the fabrication of a number of bonded cells in one process step and facilitates metal grid alignment. A brief discussion is given here on a possible future implementation of adhesive wafer bonding for MSSC production using BCB.

To reduce the optical losses in the MSSC, the metal patterns on all cells should be aligned. N-contacts can be formed on the back surface of the GaAs cell using back surface alignment in a suitable mask aligner tool. The use of a wafer bonder can facilitate the alignment of a metal grid patterned on the backside of a GaAs cell wafer with the front contact of an InGaAs cell wafer. This will reduce the optical losses in the bottom cell. Furthermore, if the GaAs cell is grown in an inverted structure, the GaAs substrate can be removed post-bonding to increase the transmission of long wavelength photons through the top cell.

The planarisation capabilities of BCB are advantageous for wafer bonding of MSSCs as the metal contacts on the back of the GaAs based top cell and InGaAs bottom cell will have metal grid contacts formed before BCB application and bonding (Figure 5.17 (a)).

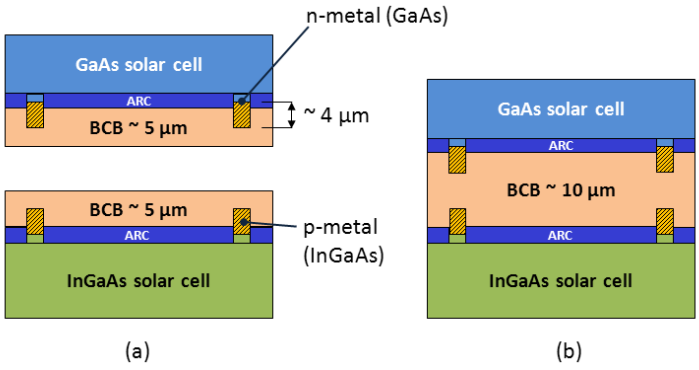


Figure 5.17: Outline of BCB wafer bonding process: (a) BCB is spin coated on the back of the top cell and front of the bottom cell at ~ 5 µm thickness providing a planar surface for bonding (b) cells are bonded by contacting the BCB layers and curing.

For large area wafer bonding, a planar surface is required in order to ensure adequate bond strength. For spin-coated BCB, as in Figure 5.18, the planaristaion ratio of BCB is > 95% for 4 µm layer thicknesses when the width of the metal features is ~10 µm. This is adequate for a MSSC as metal grid finger width is typically in the 5 – 20 µm range. Furthermore, the data given

by Dow Corning is for metal line heights of 4 μm which is within the range expected for plated metal contacts although metal plating was not undertaken in this thesis.

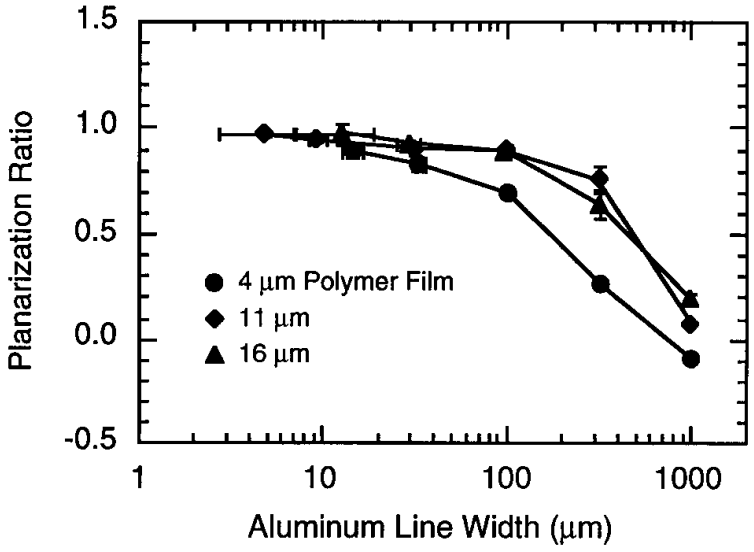


Figure 5.18: Planarization ratio as a function of metal line width for dry etch grade BCB (3022 series). The metal line height is 4 μm [5].

5.6. Summary

A GaAs solar cell design has been used to grow devices for use in an MSSC with a measured 1-Sun efficiency of 22.3%. The cells were adapted for use with an electrically insulating adhesive bond by fabricating both p- and n-contacts on the front surface. The increased metal shading and reduced fill factor led to a decreased cell efficiency of 20.6%.

A flip-chip solar cell bonding process, using BCB, was developed and used to fabricate prototype III-V mechanically stacked solar cells. A 13 μm bonding layer was fabricated between the cells by applying an initial force of 4 N/cm^2 at a temperature of 150 ^{o}C in the flip-chip tool and subsequently transferring the chips to an oven for a final cure at 210 ^{o}C for 2 hours. 'Wedging' in the bond interface was found through optical imaging of the diced cells and the optical performance of the interface as measured for the EQE of the InGaAs cell. The flip-chip process is limited in its use for forming MSSCs as significant control of the adhesive interface properties is difficult to achieve. The results show the potential for BCB to reduce the reflection at the cell interface, in conjunction with thin-film anti-reflection coatings, and I would recommend trialling adhesive wafer bonding of solar cell structures using BCB. This technology would allow the

bonding of multiple MSSCs in one process improving scalability. Void free 4" Si wafer bonded pairs have been demonstrated by Niklaus *et al.* [8].

5.7. References

[1] G. J. Bauhuis, P. Mulder, E. J. Haverkamp, J. C. C. M. Huijben, and J. J. Schermer, "26.1% thin-film GaAs solar cell using epitaxial lift-off," *Sol. Energy Mater. Sol. Cells*, vol. 93, no. 9, pp. 1488–1491, Sep. 2009.

[2] L. Zhao, G. Flamand, Y. Mols, J. V. der Heide, and J. Poortmans, "Novel Mechanically Stacked Multi-Junction Solar Cells Applying Ultra-Thin III-V Cells and Wafer Based Germanium Cell," *ECS Trans.*, vol. 27, no. 1, pp. 1123–1128, Nov. 2010.

[3] J. Yang, Z. Peng, D. Cheong, and R. Kleiman, "III-V on silicon multi-junction solar cell with 25% 1-Sun efficiency via direct metal interconnect and areal current matching," in *Proceedings of the 27th EUPVSEC*, 2012.

[4] H. Matsubara, T. Tanabe, A. Moto, Y. Mine, and S. Takagishi, "Over 27% efficiency GaAs/InGaAs mechanically stacked solar cell," *Sol. Energy Mater. Sol. Cells*, vol. 50, no. 1–4, pp. 177–184, Jan. 1998.

[5] "Processing Procedures for Cyclotene 4000 Series Photo BCB Resins," Dow Corning, Mar. 2009.

[6] A. Jourdain, P. D. Moor, K. Baert, I. D. Wolf, and H. A. C. Tilmans, "Mechanical and electrical characterization of BCB as a bond and seal material for cavities housing (RF-)MEMS devices," *J. Micromechanics Microengineering*, vol. 15, no. 7, pp. S89–S96, Jul. 2005.

[7] NREL, "ASTM (G-173-03)," *http://rredc.nrel.gov/solar/spectra/am1.5/*. .

[8] F. Niklaus, P. Enoksson, E. Kälvesten, and G. Stemme, "Low-temperature full wafer adhesive bonding," *J. Micromechanics Microengineering*, vol. 11, no. 2, pp. 100–107, Mar. 2001.

Chapter 6

Conclusions and Future Work

This thesis has investigated the design and application of solar cells with lattice constants equal or close to that of InP in order to improve the efficiency of multi-junction photovoltaic devices by reducing the constraint of current matching.

The current-matching requirement of monolithic multi-junction solar cells, which are connected in series by tunnel junctions, restricts their ultimate efficiency. Cell architectures that increase the portion of the solar spectrum converted to photocurrent provide one route to overcoming this restriction.

The PV efficiency of MSSCs, formed with solar cells grown lattice-matched to host substrates, was investigated using electrical and optical modelling. A III-V mechanically stacked solar cell with a separately connected InGaAs bottom cell under a GaAs based top cell was chosen as the most suitable to pursue high efficiencies under concentration. In order to provide an optimum response from the bottom cell, adhesive bonding was proposed to reduce the refractive index step between the cells. BCB was found the most suitable compared to the other adhesives considered owing to its relatively high thermal conductivity and refractive index. A single-junction InGaAs cell was designed, grown and fabricated with a 1-Sun PV efficiency of 9.3%. The cell design was optimised for response in the 880 – 1700 nm range for sunlight transmitted through GaAs with a peak EQE response of 93.8% at 1030 nm. A single-junction GaAs cell design with a measured 1-Sun PV efficiency of 22.3% was presented. As an electrically insulating adhesive (BCB) is proposed to form MSSCs, a processing procedure was developed to fabricate GaAs cells with both p and n-contacts on the front surface to allow electrical contacting. The increased metal shading and reduced fill factor of the ‘top-contacted’ cell reduced the 1-Sun efficiency to 20.5%. GaAs and InGaAs cells were successfully bonded, using a 13 μm layer of BCB, in a flip-chip process with a final combined 1-Sun cell efficiency of 25.2%. GaAs substrate absorption, excessive metal shading and the use of a non-ideal ARC on the front surface of the InGaAs cell reduced the EQE of the InGaAs device with a maximum value of 74% achieved at 1040 nm.

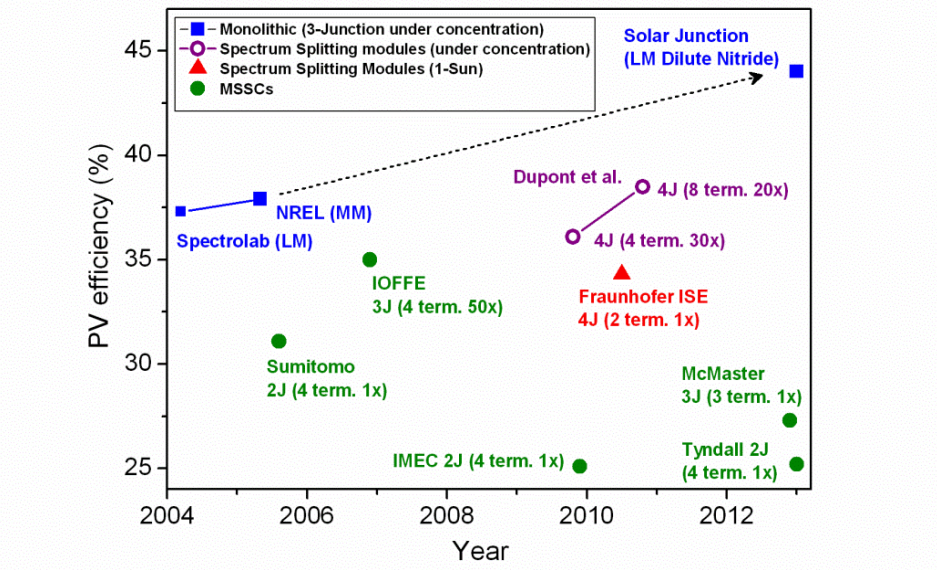


Figure 6.1: Selected results for the efficiency of multi-junction solar cells over the past decade including results from this thesis.

As summarised in Figure 6.1, while a cell efficiency of 25.2% is below the state of the art in multi-junction solar cells it is comparable to other MSSC results and presents considerable room for improvement by considering the following:

- The maximum open-circuit voltage of the single-junction InGaAs cell, 339 mV, is less than that achieved by others for InGaAs devices stacked under GaAs based top cells. Furthermore the 1-Sun value of 352 mV is below that designed in Chapter 3 of ~380 mV. An issue which became apparent during the fabrication of InGaAs cells is the importance of the etch used to isolate the cells and the subsequent passivation of the sidewalls where SiN_x was used in this case. Further process optimisation is required before the maximum open-circuit voltage for the InGaAs solar cell structure will be achieved.
- The optical losses in the MSSC are higher than what can be achieved and must be reduced. The measured reflection from the front surface of the MSSC is up to 20% in the 880 – 1700 nm wavelength range. This is higher than was designed for in Chapter 3. A higher refractive index ARC must be deposited on the InGaAs cell to reduce reflection at this interface, however, it must also achieve adequate passivation of the cells as discussed above. Furthermore a significant loss is also seen from parasitic absorption in the GaAs substrate. The use of a thin-film III-V solar cell, with complete substrate removal, would remove this loss but presents other processing challenges.

- While the top cell was not the focus of this thesis it contributes the largest portion of the final MSSC efficiency. In the current GaAs-InGaAs arrangement the top cell achieved an efficiency of 20.5% under 1-Sun conditions. This can be improved by designing a better metal contacting scheme which does not shade the top device but results in low series resistance. The integration of a wider bandgap GaInP cell and subsequent tunnel junction to provide a dual-junction top cell will further improve the efficiency of the MSSC.
- Ultimately this system will be judged by its performance under concentration which is only worthwhile with the design of a low resistance contacting scheme. Thickening of metal contacts must also be performed on all cells, which may present challenges for the BCB bonding process as thicker fingers must be accommodated at the cell/bond interface.

In a second aspect of the thesis, InAlAs cells were designed and characterised to determine the PV characteristics of this material relevant to multi-junction cell fabrication. The extracted minority carrier diffusion lengths of 710 and 2080 nm for the emitter (p-type $3x10^{18}$ cm^{-3}) and base (n-type $4x10^{17}$ cm^{-3}) layers are adequate for use in monolithic cell formation and compare to 14 μm and 5 μm for equivalently doped GaAs layers. Furthermore, fabricated cells had a PV efficiency of 6.6% using 800 nm thick absorber layers under 48% metal shading showing the promising potential of the material. The measured open-circuit voltage of 925 mV is close to the state of the art for an InAlAs cell under 1-Sun conditions.

The lattice constant of a GaAs host substrate was graded to that of InP using an $In_xGa_{1-x}As$ grade onto which InGaAs and InAlAs solar cell structures were grown by MOVPE. A significant performance drop was found in these cells as compared to those grown lattice matched on InP and a defect density of $5x10^8$ cm^{-2} was estimated to extend from the graded structure to the cells as extracted by electrical and optical characterisation. Significant further work is required to develop both the InAlAs solar cell and virtual substrate namely.

- Single-junction cell performance can be improved by using a thicker base layer to absorb more photons, reduce grid-metal shading and using a double layer anti-reflection coating to reduce reflection across a broader wavelength range. Additionally, a more comprehensive understanding of the carrier transport properties of InAlAs as a function of doping level and polarity is needed to design an optimised junction to increase the power produced.

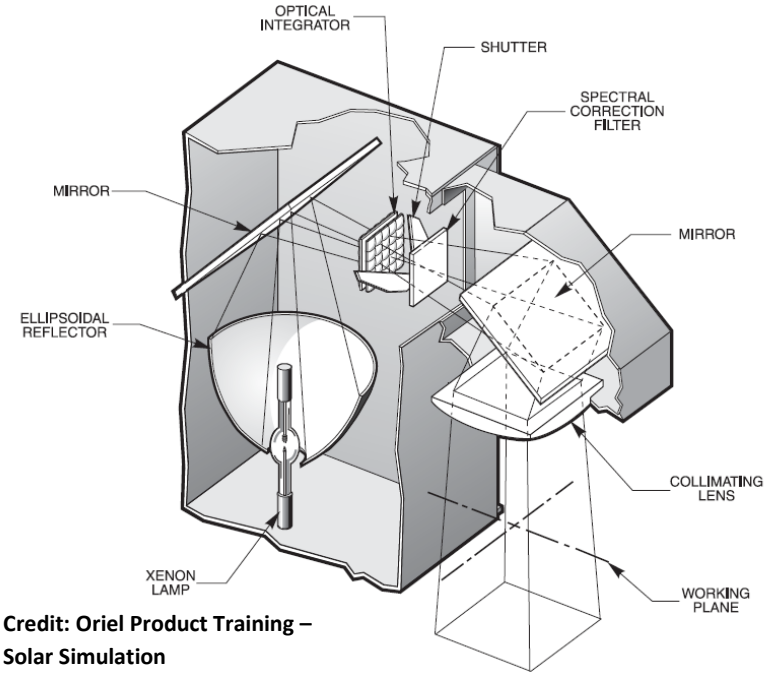
- A suitable lower cost and low defect density substrate with a lattice constant of 5.87 Å must be developed. The design presented in this thesis used a relatively thin 1 μm grade which was not adequate to contain the induced strain. Possible routes to improving the graded substrate include using thicker grading layers to better contain the strain or trialling a GaInP grade. Ultimately, the objective of this work should be the integration of the cell design on low cost Si substrates.

While the future work suggestions given imply significant research is required before either technology outlined in this thesis can be fully compared to the state of the art multi-junction solar cells, the study of high efficiency photovoltaics through mechanical stacking of solar cells based on the InP lattice constant suggests a commercially compelling case can be made for pursuing these cells. The work presented here demonstrates proof of concept that forming multi-junction solar cells at alternative lattice constants to GaAs can lead to higher efficiency photovoltaics than are currently available.

Appendix A: Photovoltaic and Electrical characterisation

Solar Simulation

The photovoltaic conversion efficiency of the solar cells is measured using a Newport Oriel 91193 series 1000 W solar simulator with a 6" x 6" output beam (± 3^{o} collimation). The system uses an ozone free Xenon short arc lamp with a beam uniformity of ± 5%. An AM1.5G spectra filter is installed in the system to produce the desired spectral characteristics. The illumination housing provided contains the lamp, lamp ignitor, optical integrator, shutter and collimating optics while a separate dark housing was built to contain the measurement set-up. A constant source power supply is used to control the current level in the lamp.



Credit: Oriel Product Training – Solar Simulation

Fig. A: Layout of the lamp housing of the Newport Oriel 91193 Solar Simulator.

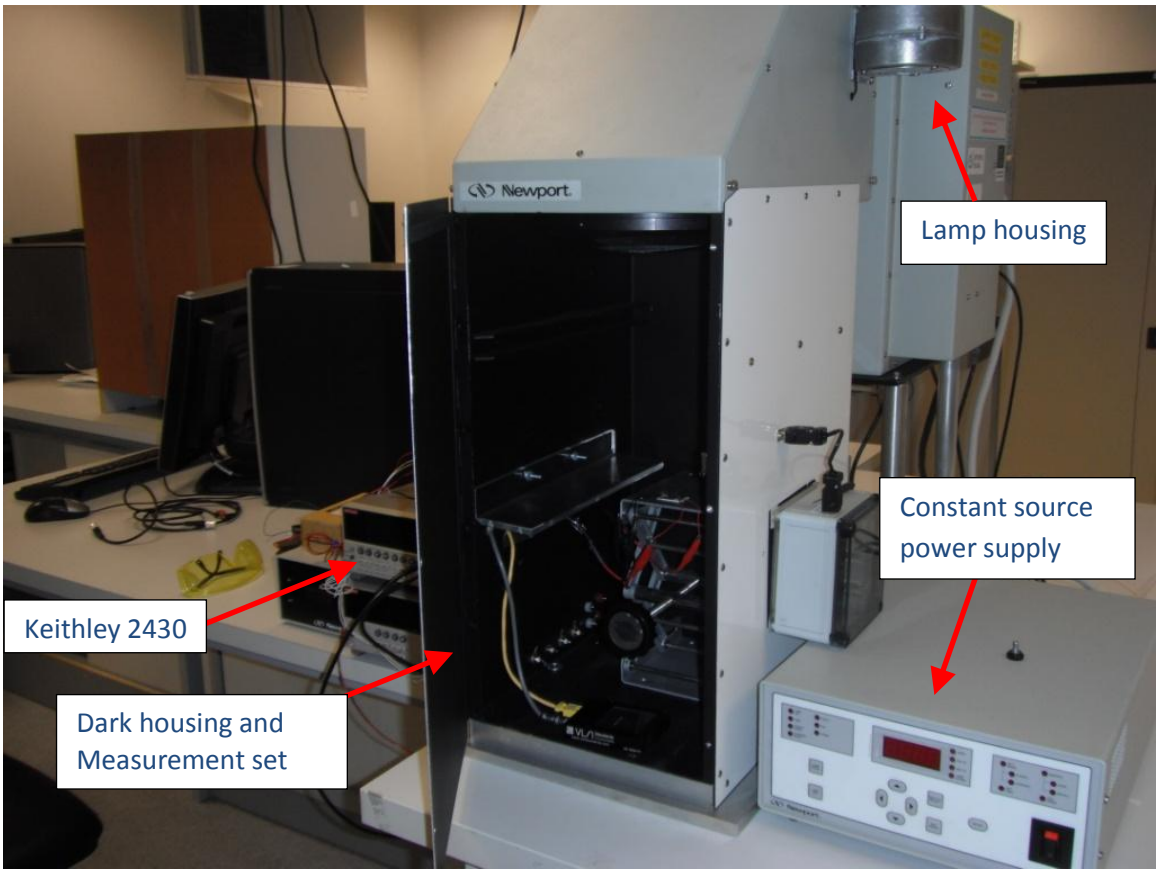


Fig. B: Picture of the solar simulator.

The incident spectrum is calibrated at 0.1 W/cm^2 using an Oriel reference cell. The reference cell system consists of a readout device and a 2 x 2 cm calibrated monocrystaline silicon solar cell. The system is accredited by NIST to the ISO-17025 standard. The readout device reads solar simulator irradiance in units of suns (up to a maximum of 3.5 suns) where one sun is equal to 1000 ± 1 W/m^2 at 25 °C and AM1.5 Global Reference.



Credit: www.newport.com

Fig. C: Readout meter and reference cell assembly.

Electrical measurement is completed using the 4-point probe method. A Labview VI sweeps the bias of a Keithley 2430 which is used to measure current.



Fig. D: Picture of the inside of the dark housing showing a solar cell under test (lamp shutter closed). The reference cell is also shown although it is placed on the adjustable stage when reading light intensity.

Spectral Response

The Bentham PVE300 was used for the measurement of Spectral Response and Internal/External Quantum Efficiency.

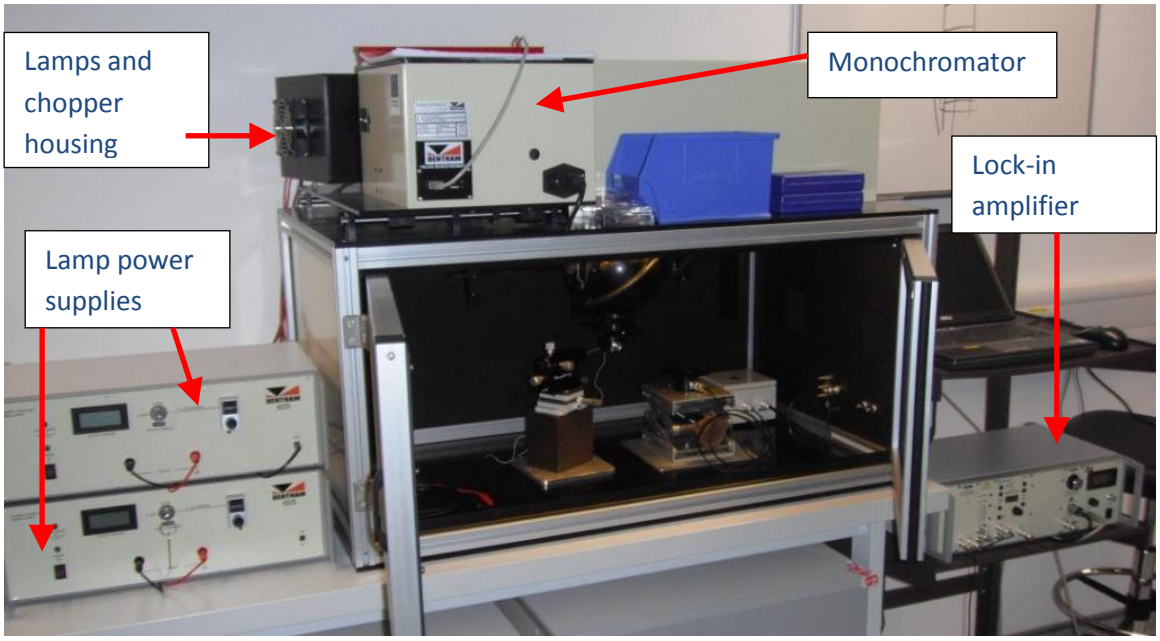


Fig. E: Picture of the Bentham PVE300 with relevant parts labelled.

Overview of Operation

A monochromatic probe is assembled from a TMc300, 300mm focal length monochromator, with three diffraction gratings and a dual Xenon/ quartz halogen light source, providing illumination from 250 to 2500 nm. The dual light source is fitted with an optical chopper (10 Hz-2 kHz). The sample under test is mounted horizontally on a mount. The monochromatic probe is made to be incident upon the sample under test; at each wavelength the photocurrent generated by the device is measured. The device photocurrent is contacted using standard probes and measured using a lock-in amplifier and chopper system to remove background current. A dark housing is provided for the system as shown in Figure G. Having measured the beam power with a detector of known responsivity, spectral response and EQE can be directly obtained.

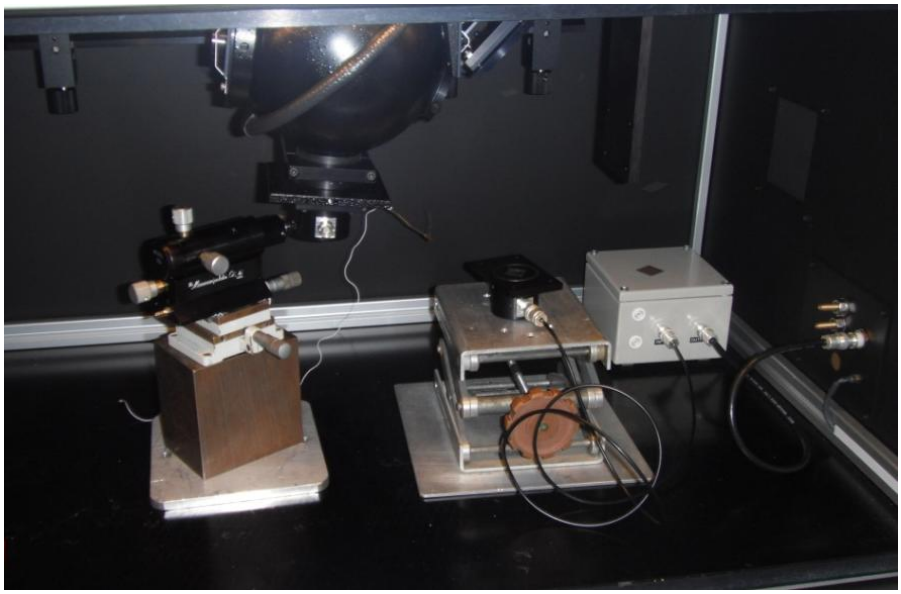


Fig. F: Picture of the measurement set-up within the spectral response kit. A calibrated Si photodetector is shown under the illuminating beam (not on). Only one probe is shown for clarity.

Appendix B: Detailed balance limit of efficiency calculation

Simulation procedure as outlined by Letay and Bett in Reference [2], Chapter 2.

The efficiency of a solar cell with a current-voltage dependence J(V) is given by:

$$\eta = \frac{P_{cell}/A}{P_{in}/A} = \frac{V_{mpp} j_{mpp}}{P_{in}/A}$$

1. Calculate the generation current, j_g
2. Determine the recombination current, j_r, considering radiative recombination only
3. Compute maximum power of the cell by establishing a current-voltage relationship and considering current matching

For each junction in a stack, the generated current density, j_g, is found using:

$$j_g = k_{EQE} \frac{q}{hc} \int_{\lambda_i}^{\lambda_g} \lambda I(\lambda) d\lambda$$

i.e. the number of incident photons is multiplied by the number of carrier pairs generated per photon, k_{EQE} *(unity assumed),* for the complete solar spectrum where, *q*, is the charge per electron, *c*, is the speed of light, *h*, Planck's constant and, *I(l),* the power density of the spectrum per wavelength. λ_i is the bandgap of the preceding junction (zero for highest bandgap junction) and, λ_g, the bandgap of the junction in wavelengths ($\lambda = hc/E_g$). For current matched cells, j_g, is found for each junction and the cell current taken as the minimum.

The only recombination mechanism considered is radiative recombination that occurs in each cell due to the radiation equilibrium of the cell with its environment.

$$j_r = \frac{2\pi q}{h^3 c^2} (n_o^2 + n_u^2) \int_{Eg}^{\infty} E^2 \frac{1}{exp\left(\frac{E - qv}{kT}\right) - 1} dE$$

An analytical version of which is:

$$j_w = \frac{2\pi q}{h^3 c^2} (n_o^2 + n_u^2) kT \left[E_g^2 + 2kTE_g + 2(kT)^2\right]$$

V, is the applied voltage, *no (nu),* is the refraction index of the medium over (under) the junction. The factor $(n_o^2 + n_u^2)$ represents the influence of total internal reflection of the escaping rays (for a more detailed discussion of this influence see Letay and Bett).

The current voltage dependence if found in the usual manner and the derivation of the power equation set = 0 to find the maximum power point. The maximum power from each cell is added to give P_{cell}.

$$j(V) = j_g - j_o\left(e^{\frac{qV}{kT}} - 1\right) where\ j_o = j_w e^{Eg/kT}$$

$$P = jV, P_{mpp} \rightarrow 0 = \frac{dPj}{dj}, P_{cell} = \sum P_{mpp}$$

Appendix C: PC1D

PC1D is a solar cell modelling programme developed by the University of New South Wales available as a free download [Chapter 2: 34]. The programme solves the one-dimensional carrier transport equations to simulate the performance of solar cells. A simple graphical user interface is supplied which allows the easy set-up of the model to be solved and interfacing with the results. Figure A is a screenshot of the input page and shows the required parameters that are entered in the programme. The thickness, doping and carrier transport properties of the various semiconductor layers in a solar cell can be altered. The effect of additional external parameters on solar cell power output are considered such as reflection, cell resistances and illumination spectrum.

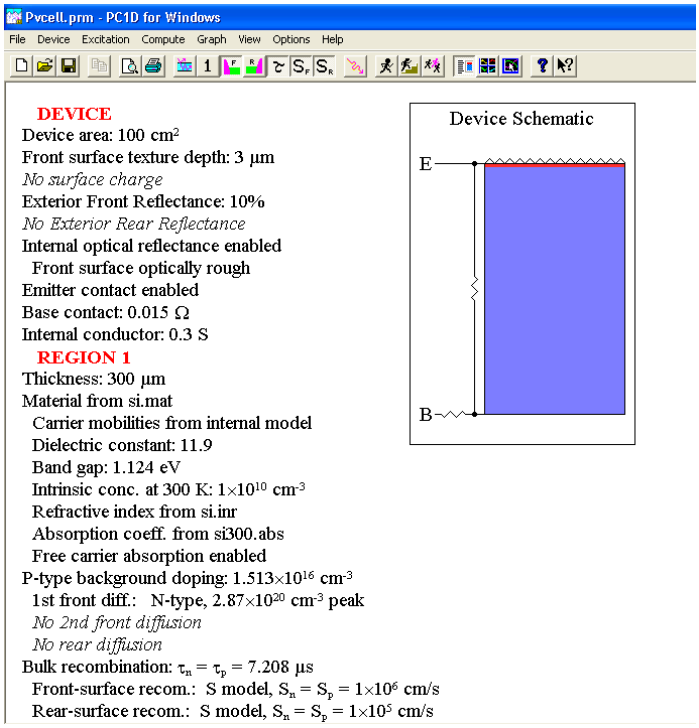


Fig. G: Screenshot of the parameter input screen of PC1D.

The simulation results are provided on an additional page of the programme and provide access to temporal results such as current, voltage and power (Figure B). Spatial analysis of the various regions in the solar cell is also provided allowing a better understanding of the device physics of the modelled cell. Band diagrams and carrier density as a function of depth are provided as well as other outputs.

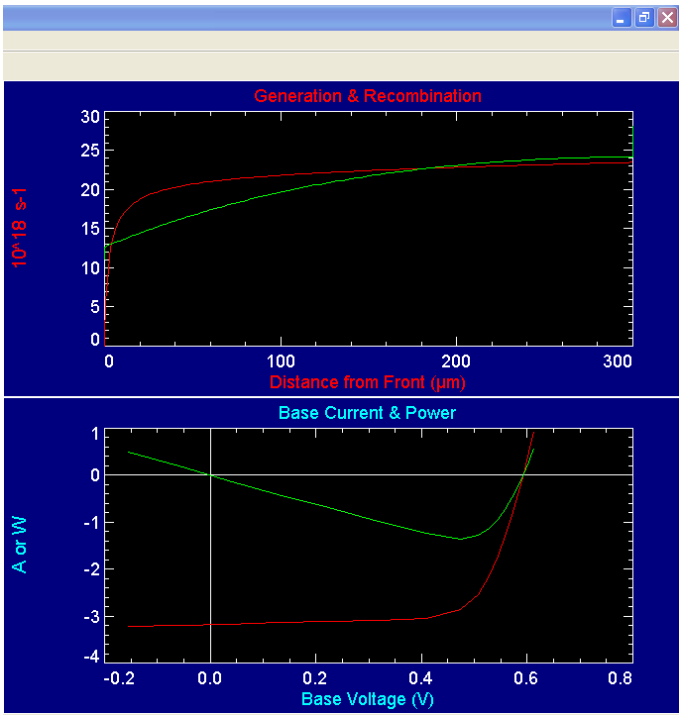


Fig. H: Screenshot of the output screen of PC1D.

Appendix D: Nominal and measured solar cell structures grown by MOVPE

Tab. A: InGaAs solar cell

Layer	Material	Nominal Doping cm^{-3}	Measured CV cm^{-3}	Nominal Thickness nm	Measured SEM nm
Cap	p-$In_{0.53}Ga_{0.47}As$	3-4x10^{19}	~4x10^{19}	20	250
Cap	p-$In_{0.53}Ga_{0.47}As$	1x10^{19}	>2x10^{19}	230	
Window	p-InP	2x10^{18}	2-3x10^{18}	100	110
Emitter	p-$In_{0.53}Ga_{0.47}As$	2x10^{18}	1.5x10^{18}	100	3250
Base	n-$In_{0.53}Ga_{0.47}As$	3x10^{17}		3000	
BSF/Buffer	n-InP	1x10^{19}		500	

Tab. B: InAlAs solar cell

Layer	Material	Nominal Doping cm^{-3}	Measured CV cm^{-3}	Nominal Thickness nm	Measured TEM nm
Cap	p-$In_{0.53}Ga_{0.47}As$	1x10^{19}	1x10^{19}	200	200
Window	p- $In_{0.35}Al_{0.65}As$	1x10^{18}	-	20	25
Emitter	p-$In_{0.52}Al_{0.48}As$	3x10^{18}	~3x10^{18}	300	800
Base	n-$In_{0.52}Al_{0.48}As$	4x10^{17}	3.7x10^{17}(Hall)	500	
LCL	n-InP	5x10^{18}		2000	2000
Buffer	n-InP	2x10^{18}		100	

Tab. C: GaAs solar cell

Layer	Material	Nominal Doping cm^{-3}	Measured CV cm^{-3}	Nominal Thickness nm	Measured SEM nm
Cap	p-GaAs	8x10^{18}		200	216
Window	p-$Al_{0.85}Ga_{0.15}As$	1x10^{17}		40	45
Emitter	p-GaAs	2x10^{18}		400	463
Base	n-GaAs	2x10^{17}		3000	3250
BSF	n- $Al_{0.30}Ga_{0.70}As$	1x10^{18}		40	38

Buffer	n-GaAs	$2x10^{18}$	100

Appendix E: Si Solar Cell

Single-junction Si solar cells were purchased from the National Renewable Energy Centre, UK (Figure I).

Design:

Laser Grooved Buried Contact Cz silicon concentrator solar sells

- Random pyramidal texturing on the front of the cell, carried out by anisotropic texturing
- Silicon nitride (90 nm) ARC: LPCVD
- 16mm long and 22mm wide (two busbars each 1.5mm wide giving an active width of 19 mm)

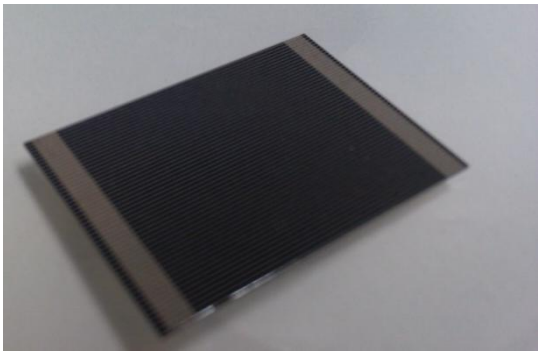


Fig. I: Optical image of NAREC Si solar cell.

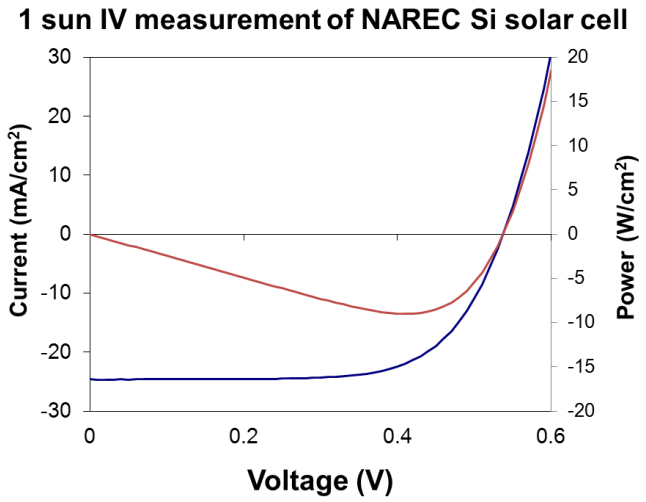


Fig. J: Measured 1-Sun IV characteristics of single-junction NAREC Si solar cell.

Appendix F: Solar cell processing procedures, detailed processing conditions and mask layouts

Tab. D: Processing procedure for InGaAs solar cell with blanket n-metallisation on the back surface.

	Process	Mask	Desired	Measured
1	Back surface clean	-		-
2	lift-off lithography	SingleJunction _Grid metal		-
3	p-metal evaporation		30:50:150 nm	260 nm
4	metal lift-off			0.5 hrs
4	n-metal evaporation	(back surface)		
5	metal anneal			390 C
6	InGaAs cap etch (stop InP)		250	35 s
7	Mesa etch - InGaAs	SingleJunction _Trench		3950 (658 nm/min)
8	SiN deposition (140 nm)		140	140 (13 mins)
9	SiN contact opening	SingleJunction _Contact opening		4 min
10	Scribe			

Tab. E: Processing procedure for InGaAs solar cell with both p- and n-contacts on the front surface.

	Process	Mask	Desired	Measured
1	lift-off lithography	MSSC_Grid2 front contact		-
2	p-metal evaporation		30/50/150 nm	260 nm
3	metal lift-off			0.5 hrs
4	Lithog. for n-contact etch	MSSC_mesa		
5	InGaAs etching for n-contact		1000 nm	1270 nm (635 nm/min)
6	Lithog. for n-contact	MSSC_back metal		
7	n-metal evaporation			
8	metal lift-off			0.5 hr
9	metal anneal			390 C
10	InGaAs cap etch (stop InP)		250	35 s
11	Mesa etch - InGaAs	MSSC_trench		4600 (707 nm/min)
12	SiN deposition (140 nm)		140	165 (16 mins)
13	SiN contact opening - BOE	MSSC_Grid2 bus open		3 min
14	Scribe			

Tab. F: Processing procedure for InAlAs solar cell with blanket n-metallisation on the back surface.

	Process	Mask	Desired	Measured
1	Back surface clean			-
2	lift-off lithography	Photodiode_grid metal		-
3	p-metal evaporation		30: 50: 200	
4	metal lift-off			1 hr
4	n-metal evaporation	(back surface)		
5	metal anneal			395 C
6	InGaAs cap etch (stop InAlAs)		200 nm	200 nm (50 s)
7	Lithog. for mesa etch	Photodiode_trench		
8	InAlAs etching to InP		1000 nm	990 (540 s)
9	SiN deposition (70 nm)		70	77 (7 mins)
10	SiN contact opening	Photodiode_contact opening	77	77 (2 mins)
11	Scribe			

Tab. G: Processing procedure for InAlAs solar cell with both p- and n-contacts on the front surface.

	Process	Mask	Desired	Measured
1	lift-off lithography	MBL_Grid		-
2	p-metal evaporation		30: 50: 200	
3	metal lift-off			1 hr
4	Lithog. for n-contact etch	MBL_mesa		
5	InAlAs etching to InP		1000 nm	1020 nm (540 s)
6	Lithog. for n-contact	MBL_n-metal		
7	n-metal evaporation			
8	metal lift-off			0.5 hr
9	metal anneal			395 C
10	InGaAs cap etch (stop InAlAs)		200 nm	200 nm (50 s)
11	SiN deposition (70 nm)		70	77 (7 mins)
12	SiN contact opening	MBL_contact open	77	77 (2 mins)
13	Scribe			

Tab. H: Processing procedure for GaAs solar cell with blanket n-metallisation on the back surface.

	Process	Mask	Desired	Measured
1	lift-off lithography	SingleJunction_Grid metal		
2	p-metal evaporation		30/50/200	250
3	metal lift-off			
4	n-metal evaporation	(back surface)		
5	metal anneal			
6	GaAs cap etch		200 nm	200 nm (3 min-expected 60 s)
7	Lithog. for mesa etch	SingleJunction _Trench		
8	Mesa etch - GaAs		5 µm	5 µm (5 min)
9	DLARC deposition	ZnS/SiO_2	48/74	46/79
10	DLARC contact opening	SingleJunction _Contact opening		
11	Scribe			

Tab. I: Processing procedure for GaAs solar cell with both p- and n-contacts on the front surface.

	Process	Mask	Desired	Measured
1	lift-off lithography	MSSC_Grid2 front metal		-
2	p-metal evaporation		30/50/200	250
3	metal lift-off			
4	Lithog. for n-contact etch	MSSC_mesa		
5	n-contact etch - GaAs		5 µm	~ 5 µm (80 s)
6	Lithog. for n-contact	MSSC_back metal		
7	n-metal evaporation			
8	metal lift-off			1 hr
9	metal anneal			
10	GaAs cap etch		200 nm	200 nm (3 min-expected 60 s)
11	Lithog. for mesa etch	MSSC_trench		
12	Mesa etch - GaAs		5 µm	5 µm (5 min)
13	DLARC deposition (70 nm)	ZnS/SiO_2	48/74	46/79
14	DLARC contact opening	MSSC_Grid2 bus open		
15	Substrate thinning		360 µm thin to 150 µm	thinned to 140 µm (9 mins)
16	ZnS deposition on back surface		130 nm	
17	Scribe			

Detailed processing conditions:

Thinning station

Back surface clean

□ 180s etch in Br:MeOH bubbler thinning station

Substrate thinning

□ etch in Br:MeOH bubbler thinning station (~20 μm/min)

Lithography

Lift-off lithography

□ Ni blow-clean
□ Spin on HMDS: 4000 rpm for 60 seconds
□ Spin on LOR10A: 4000 rpm for 60 seconds
□ Hotplate: 150˚C for 3 minutes
□ Spin on HMDS: 4000 rpm for 60 seconds
□ Spin on S1813: 4000 rpm for 60 seconds
□ Hotplate: 115˚C for 2 minutes
□ Expose (MA1006): 10 seconds, Hard contact
□ Develop: MF319 for 75 seconds
□ DI rinse
□ Oven: 90˚C for 30 minutes
□ Amm: DI (1:10) dip for 20 seconds

Lithog. for n-contact etch

□ Ni blow-clean
□ Spin on HMDS: 4000 rpm for 60 seconds
□ Spin on S1813: 4000 rpm for 60 seconds
□ Hotplate: 115˚C for 2 minutes
□ EBR [Acetone wipe]
□ Expose (MA1006): 7 seconds, Hard contact
□ Develop: MF319 for 45 seconds
□ DI rinse
□ Hotplate: 120˚C for 5 minutes

Lithog. for mesa etch

□ Ni blow-clean
□ Spin on HMDS: 4000 rpm for 60 seconds
□ Spin on S1813: 4000 rpm for 60 seconds
□ Hotplate: 115˚C for 2 minutes
□ EBR [Acetone wipe]
□ Expose (MA1006): 7 seconds, Hard contact
□ Develop: MF319 for 45 seconds
□ DI rinse
□ Hotplate: 120˚C for 5 minutes

Metals

P-metal evaporation

□ Evaporation of Ti:Pt :Au

N-metal evaporation
□ Evaporation of Au : Ge : Au : Ni : Au [14 :14 :14 :11 : 250 nm]

Metal lift-off
□ Lift off in 1165 solvent at 100°C
□ DI rinse + N2 blow dry

metal anneal
□ Anneal at 420 °C for 3 minutes at neck of furnace (1.5 sccm - 5% H_2 / 95% N_2)
□ Anneal at 420 °C for 5 minutes at middle of furnace (1.5 sccm - 5% H_2 / 95% N_2)
□ Anneal at 420 °C for 3 minutes at neck of furnace (1.5 sccm - 5% H_2 / 95% N_2)

III-V etching

InGaAs cap etch (stop InP)
□ H_3PO_4:H_2O_2:H_2O = 1:1:8

InGaAs cap etch (stop InAlAs)
□ $C_6H_8O_7$:H_2O_2 (2:1) (don't stir solution)

GaAs cap etch
□ $C_6H_8O_7$:H_2O_2 (5:1) (don't stir solution)

Mesa etch - InGaAs
Deposit 1200 nm standard SiN PECVD
□Standard recipe deposition -120 mins
Photo-lithography (Mask: SingleJunction_Trench)
□ Spin on AZ5214: 4000 rpm for 60 seconds
□ Hotplate: 115˚C for 2 minutes
□ Expose (MA1006): 7 seconds, Hard contact
□ Develop: MF319 for 27 seconds
□ DI rinse
□ HP: 5 min 120 C
SiN patterning - PicoAsher
□ CF4 plasma in PicoAsher_(14 min)
Remove PR
□ Solvent 1165, 110 C – 15 mins
□ DI rinse
ICP – III-V etching
Recipe: 'InP 4um Cl2:CH4:H2 Yang Hua' (10:8:4 sccm)
□ Cl_2/CH_4/H_2 plasma in Oxford ICP system for 6 min
Strip SiN
□ BOE 2 min (etched 60 nm)
□ CF4 plasma in PicoAsher_8 min (~ 90 nm/min)

InGaAs etching for n-contact
Deposit 700 nm standard SiN PECVD
□Standard recipe deposition -63 mins (measured 693 nm)
Photo-lithography (Mesa definition)
□ Spin on AZ5214: 4000 rpm for 60 seconds
□ Hotplate: 115˚C for 2 minutes
□ Expose (MA1006): 7 seconds, Hard contact
□ Develop: MF319 for 27 seconds

□ DI rinse
□ HP: 5 min 120 C

SiN patterning - PicoAsher

□ CF4 plasma in PicoAsher_(7 min)

Remove PR

□ Solvent 1165, 110 C – 15 mins
□ DI rinse

ICP – III-V etching

Recipe: 'InP 4um Cl2:CH4:H2 Andrea' (10:18:12 sccm)
□ $Cl_2/CH_4/H_2$ plasma in Oxford ICP system for 2 min

Strip SiN

□ BOE 2 min (etched 60 nm)
□ CF4 plasma in PicoAsher_5 min (~ 90 nm/min)

InAlAs etching to InP

□ $H_3PO_4 : H_2O_2 : H_2O$ = 1:1:38 static wet etching
□ PR removal: 1165 @100 C 15 min

Mesa etch - GaAs

□ if n-metal on back surface protect with PR (S1813) as etch attacks Au
□ H_2O_2:HBr:DI (1:10:100)
□ PR removal: 1165 @100 C 15 min

n-contact etch - GaAs

□ protect polished back surface from etch with PR (S1813)
□ $H3PO_4$:H_2O_2:DI (4:5:8)
□ PR removal: 1165 @100 C 15 min

Dielectrics

SiN Deposition (PECVD)

□ Load sample at 30°C
□ Standard recipe deposition 'MFSiN'

SiN contact opening

Lithography

□ Spin on AZ5214: 4000 rpm for 60 seconds
□ Hotplate: 115˚C for 2 minutes
□ Expose (MA1006): 7 seconds, Hard contact
□ Develop: MF319 for 45 seconds
□ DI rinse
□ Oven baking: 90˚C for 30 minutes

Contact opening

Use CF4 recipe in asher
Etch rate given as 45-50 nm/min
□ 15 min conditioning run to clean chamber
□ 4 min etch
□ Remove PR: Solvent 1165 for 15 minutes

SiN contact opening - BOE

Lithography

□ Spin on AZ5214: 4000 rpm for 60 seconds

□ Hotplate: 115˚C for 2 minutes
□ Expose (MA1006): 7 seconds, Hard contact
□ Develop: MF319 for 45 seconds
□ DI rinse
□ Oven baking: 90˚C for 30 minutes

Contact opening

□ BOE etching - 3 min
□ Remove PR: Solvent 1165 for 15 minutes

DLARC deposition

□ Load sample in (e-beam) Lab600
□ Deposit ZnS

□ Load sample in (e-beam) Lab600
□ Deposit SiO_2, recipe: HFSiO

DLARC contact opening

Lithography

□ Ni blow-clean
□ Spin on HMDS: 4000 rpm for 60 seconds
□ Spin on S1813: 4000 rpm for 60 seconds
□ Hotplate: 115˚C for 2 minutes
□ EBR [Acetone wipe]
□ Expose (MA1006): 10 seconds, Hard contact
□ Develop: MF319 for 60 seconds
□ DI rinse
□ Hotplate: 120˚C for 5 minutes

Etching

□BOE for SiO_2 etch
□HCl:DI (1:5) for ZnS
□ Remove PR: Solvent 1165 for 15 minutes

Mask-sets layout

SingleJunction

Mask Features:

Busbar: 4.4 mm x 0.2 mm

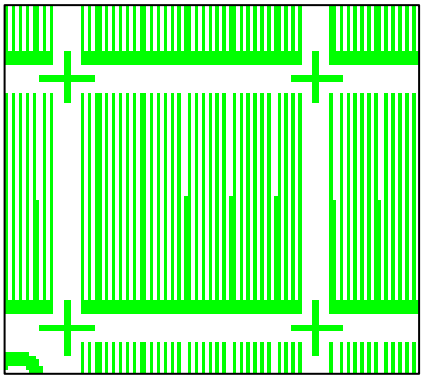
Finger: 30x 15.5 µm tapered to 4 µm

Trench isolation: 4.6 mm x 4.6 mm

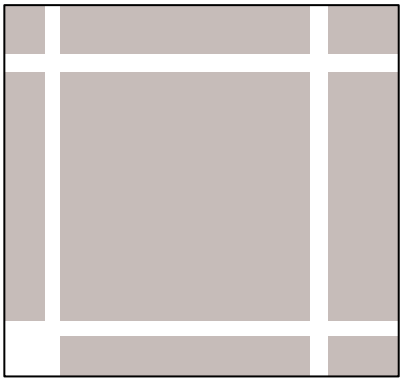
Contact opening: 4 mm x 0.18 mm

Grid coverage: 9.9%

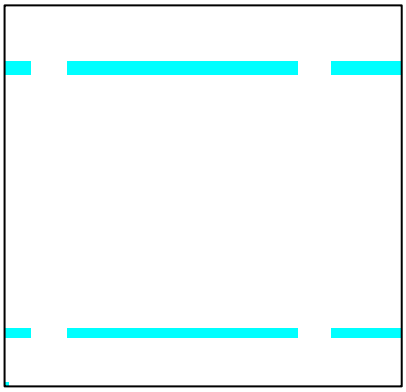
Grid metal



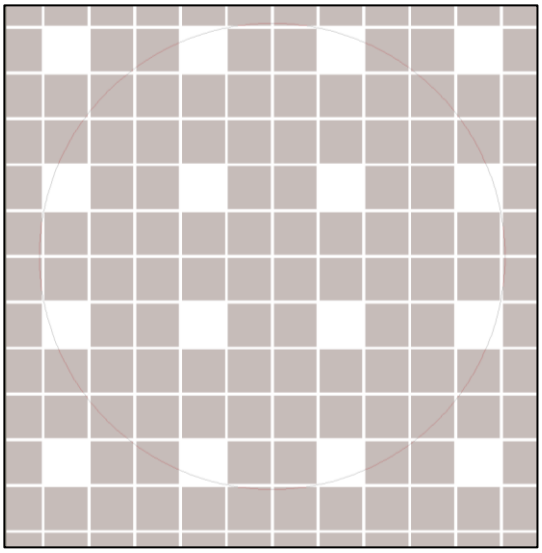
Trench



Contact opening



Overall layout (Trench shown)

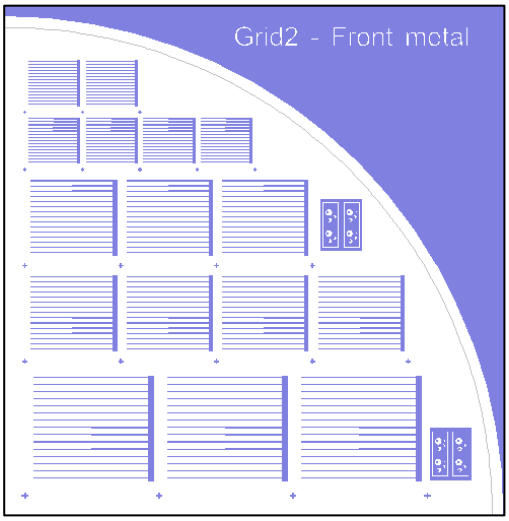


MSSC

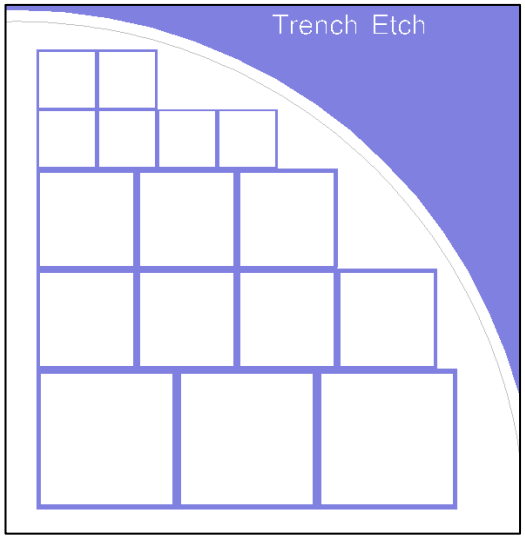
Mask Features:

Cell	A	B	C
Busbar	5.5 x 0.25 mm	3930 x 0.18 mm	2360 x 0.11 mm
Fingers (15 each)	20 tapered to 5 (6 mm long)	14.3 tapered to 3.6 (4.3 mm long)	8.6 tapered to 2.1 (2.6 mm long)
Trench	6.6 x 6.6 mm	4.7 x 4.7 mm	2.8 x 2.8 mm
n-mesa	6.4 x .35 mm	4.6 x .25 mm	2.75 x .15 mm
back metal	6.3 x .25 mm	4.5 x .18 mm	2.7 x .11 mm
Busbar	5.5 x 0.25 mm	3930 x 0.18 mm	2360 x 0.11 mm

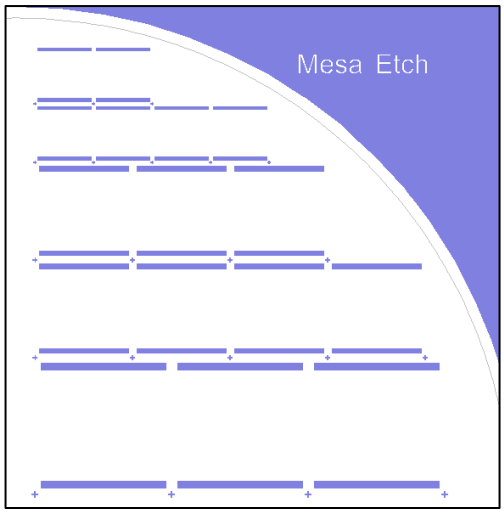
Grid2 front metal



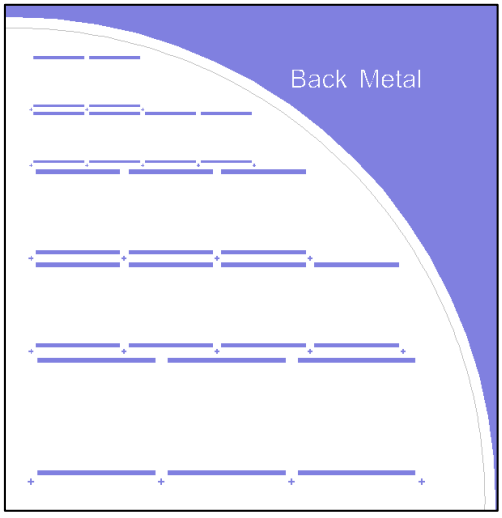
Trench



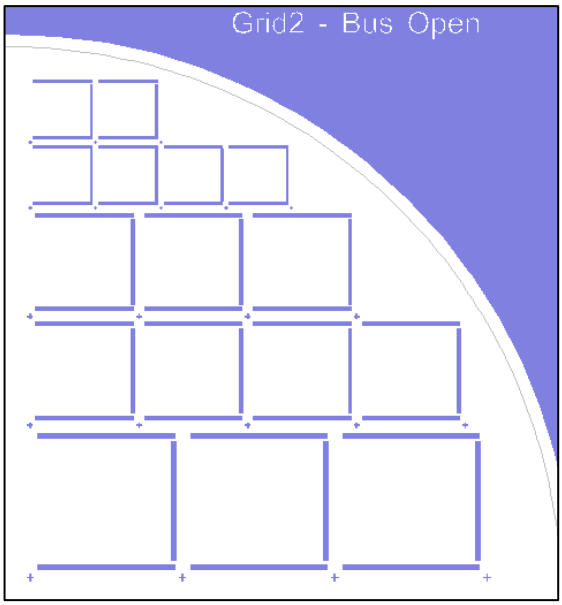
mesa



back metal



Grid2 bus open



MBL

Mask Features:

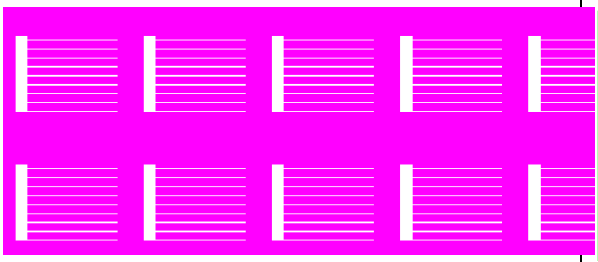
Cell area: 900 um x 700 um = 630000 um^2

Busbar: 100 um x 600 um = 60000 um^2

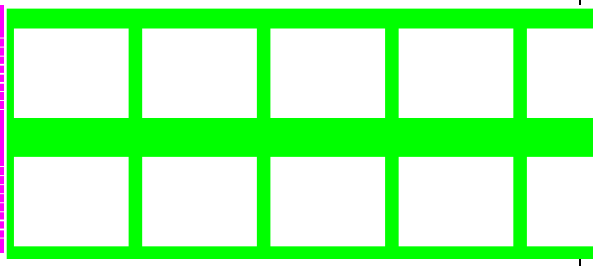
Fingers: 9no. 15 um x 700 um = 94500 um^2

Metal coverage = (60000+94500)/630000 = 24%

Grid



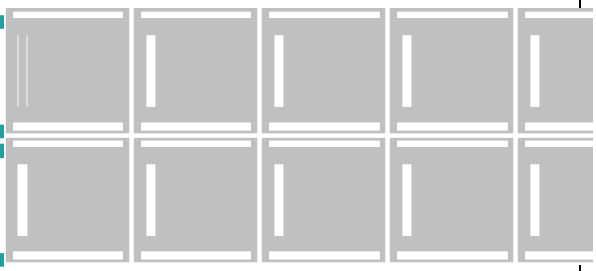
mesa



n-metal



contact open



Photodiode

Mask Features:

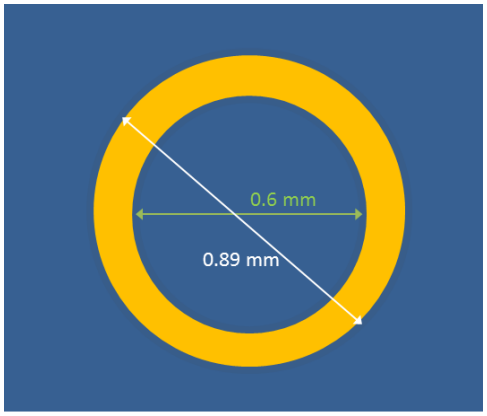
Metal: inner diameter Ø 0.6 mm, outer diameter Ø 0.89 mm

Trench isolation: Ø 0.95 mm

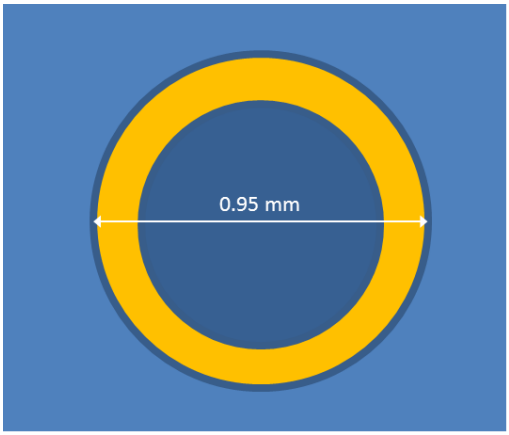
Contact opening: inner diameter Ø 0.65 mm, outer diameter Ø 0.85 mm

Grid coverage: 48%

Grid metal



Trench



Contact opening

